



The
University
Of
Sheffield.

Discovering the Potential of Additively Manufactured Steels

Jiawei Xi

A Thesis Submitted for the degree of Doctor of Philosophy

Department of Materials Science and Engineering

University of Sheffield

September 2021

Abstract

Additive manufacturing (AM) is a novel fabrication technology that has shown potential in producing high strength and structurally complex metallic parts. A wide range of legacy alloys were atomised and applied to powder bed laser additive manufacturing and the results showed that unweldable materials can be fabricated.

Recently, studies in austenitic 316L stainless steel highlighted the simultaneous enhancement in strength and ductility, which attributes to the unique microstructure of additively manufactured alloys. To understand whether laser additive manufacturing has the capability to further enhance advanced steels, a twinning induced plasticity (TWIP) steel composition is designed for AM processing and its mechanical performance was characterised in both conventionally processed and additively manufactured status. A trade-off is present in the mechanical properties of the additively manufactured TWIP steel, resulting in an inferior crashworthiness rating.

In addition to the pursuit of superior mechanical properties, the study of metastable steels has yielded surprising results. The athermal martensitic transformation in 17-4 PH stainless steel and 18Ni-300 maraging steel was reported to be suppressed by the solidification structure. The microstructure of additively manufactured M300 built with unique processing parameters was characterised and the transformation was studied with *ex-situ* X-ray diffraction. A dual stage metastability was discovered which resulted in extra amount of retained austenite.

Finally, cantilever structures were fabricated with Fe-Mn TWIP steel, 316L stainless steel and M300 maraging steel. While angular distortion was observed in the non-transforming steels, M300 shows no distortion due to its low transformation temperature.

Acknowledgement

Firstly, I would like to express my deepest appreciation to my supervisor Professor Iain Todd, for the mentoring and critical suggestions. Little did I know what kind of journey we would have together when I started my BEng final year project with you.

Secondly, I must thank my group members for the unbelievable support in the additive part of the study. Specifically, Alistair Lyle and George Maddison for the training on the Aconity platforms and the never-ending help whenever needed. Dr Felicity Freeman for the fruitful discussions around ferrous materials and guidance on the correct interpretation of additively manufactured steels. Dr Cong Liu for everyday assistance and reassuring me that we can get through this together.

Also, I would like to thank my colleagues in the materials science department who helped me in so many other aspects of the PhD journey: Neil Hind, for the heat treatment and rolling mill experiments; Dr Le Ma, for being a guardian angel in the Sorby centre and helping me with characterisation works. Professor Junheng Gao, for advice in alloy design and microscopy interpretations of high manganese steels; Dr Peng Gong, for insights in the microstructure of martensitic steels; Dr Yidong Xu. for advice in general metallurgical practices.

Finally, I would like to express my appreciation to my family and friends. My parents, for funding my study and the constant encouragement. My wife Mingfei, for accompanying me in this foreign land and always bringing up the positive side of things.

Content

Abstract	2
Acknowledgement	3
Content.....	4
List of Figures	7
List of Tables	13
Definition of Acronyms	14
1. Introduction.....	15
2. Literature Review.....	18
2.1. Metal additive manufacturing: Fundamentals	18
2.2. Defects in L-PBF	21
2.2.1. Porosity and inclusions	22
2.2.2. Cracking.....	27
2.2.3. Residual Stress.....	28
2.2.4. Conclusion	29
2.3. Basic understanding of steels.....	30
2.4. Current progress in additive manufacturing of steels	31
2.4.1. 316L stainless steel	32
2.4.2. M300 maraging steel.....	36
2.5. Advanced high manganese steel	41
2.6. Low transformation temperature electrodes(LTTE).....	48
2.7. Summary.....	50
3. Methods.....	51
3.1. Additive manufacturing with metal powder	51
3.1.1. Powder preparation	51
3.1.2. Build file design.....	51
3.1.3. Machine setup.....	52
3.1.4. Post build inspection	55
3.2. Application of high manganese TWIP steel in AM.....	55
3.2.1. Alloy selection	55
3.2.2. Arc melting and heat treatment.....	57
3.2.3. Weldability examination.....	58
3.2.4. Additive manufacturing of high manganese TWIP steel.....	58

3.2.5. Characterisation of high manganese TWIP steel	59
3.3. Additive manufacturing of M300 maraging steel	59
3.3.1. Part fabrication.....	59
3.3.2. Investigation of phase transformation.....	60
3.3.3. Austenite reversion heat treatment.....	60
3.3.4. Austenite phase fraction measurement	60
3.3.5. Microstructure characterisation of M300 maraging steel	61
3.4. Cantilever cut-off.....	61
3.5. Covid influenced work.....	61
4. Application of a High Manganese Steel for L-PBF.....	63
4.1. Background.....	63
4.2. Scope of this study	64
4.3. Alloy design and weldability test.....	64
4.4. Mechanical properties of conventionally manufactured TWIP steel.....	66
4.5. Deformation mechanism of conventionally manufactured TWIP steel.....	68
4.6. L-PBF of atomised TWIP steel powder.....	69
4.7. Microstructure of as-built TWIP steel	70
4.8. Mechanical performance of L-PBF built TWIP steel.....	74
4.9. Deformation mechanism of additively manufactured TWIP steel	75
4.10. Discussion	76
4.11. Conclusion	81
5. Metastability of Austenite in Additively manufactured M300 Maraging Steel	83
5.1. Background.....	83
5.2. Scope of the study	83
5.3. Microstructure of as-built M300 maraging steel	84
5.4. Microstructure of additively manufactured M300 maraging steel aged at 600°C	86
5.5. Feritscope measurement of phase constitution	88
5.6. Discussion	90
5.6.1. Phase constitution of additive manufactured M300 maraging steel	90
5.6.2. Application of retained austenite as a damage sensor	95
5.7. Conclusion	97
6. Self Stress-Relief Capability in Additively Manufactured Steels.....	99
6.1. Background.....	99
6.2. Scope of the study	99
6.3. Cantilever distortion in L-PBF built 316LSS and M300	101

6.4. Dilatometry of as-built M300 maraging steel.....	103
6.5. Validation of the self stress-relief effect.....	103
6.6. Discussion.....	106
6.7. Conclusion.....	108
7. Conclusion.....	110
7.1. Summary of the study.....	110
7.2. Future work.....	113
7.2.1. Further improvement to the currently proposed high manganese TWIP steel	113
7.2.2. Further understanding into the crescent shaped austenite bands.....	114
7.2.3. <i>In-situ</i> observation of γ - α' - γ during the fabrication of M300 maraging steel	115
7.2.4. Realistic experiment on utilising M300 maraging steel as a structural sensor	116
Reference.....	118
Appendix.....	127

List of Figures

Figure 2.1: a typical setup of a powder bed fusion system with indication of melt region and operating environment [10]. b: Experimental set up of a laser powder deposition System [3].	18
Figure 2.2: Schematic graph of an Arcam EBM device, a set of magnetic lenses guides the electron beam through to the build chamber. b: Typical build scenario with EBM. The overlap of melt pools are illustrated with dashed lines [2].	19
Figure 2.3: Visualisation of scanning strategies. Poor overlap or miss-alignment of islands in the strategy shown in (c) and (d) can lead to severe cracking [6].	20
Figure 2.4: (a) Optical micrograph showing a lack of fusion defect found in 304 stainless steel [7]. b: Scanning electron image showing an un-melted powder embedded in a nickel-based superalloy matrix, courtesy to Liu Cong for the image.	22
Figure 2.5: In-situ observation of the development of LOF defect due to insufficient melting. The wide range of particle size distribution also contributed to this effect as LOF defects are formed between the previous layer and large particles [8].	23
Figure 2.6: Optical micrograph showing two types of melt pools in additive manufacturing. Note the keyhole defects in the stem region [9].	24
Figure 2.7: In-situ observation of the formation of vapour depression and further development of melt pool shape due to the movement of the vapour depression zone in the laser melting of a solid block of Ti-6Al-4V [10].	24
Figure 2.8: In-situ observation of keyhole melt pool in L-PBF built Ti-6Al-4V. The evaluation of the melt pool was separated into three stages. The first stage mainly involves the establishment of the keyhole melt pool [11].	25
Figure 2.9: Plot showing how power and scan speed of the laser affects the shape of the keyhole. Note the conduction mode melt pool below the blue line [10].	26
Figure 2.10: a) SiO inclusion observed in as-built 316LSS. b) TiO inclusion in aged M300 maraging steel [16][17].	27
Figure 2.11: Modified Suutala diagram of pulsed laser welding. Note the shift in trend line between the laser welding result and TIG welding condition [22].	28
Figure 2.12: Modes of residual stress in relation to the rapid heating and cooling during the L-PBF process [26].	29
Figure 2.13: Elimination of residual stresses achieved by using a heated substrate, no distortion is seen in b) [27].	29
Figure 2.14: Typical Fe-C, Fe-Cr and Fe-Mn phase diagrams [28][29][30].	30
Figure 2.15: Bain strain approach of understanding the existence of a body centred tetragonal unit cell inside FCC lattice [31].	31
Figure 2.16: Two pie charts showing the grades of steels studied with powder bed fusion and laser metal deposition, despite the similarity in composition. Reproduced from [4].	32
Figure 2.17: (a): Mechanical properties of additively manufactured 316L compared to conventionally processed counterparts. (b): Precession electron diffraction images showing large grains and sub-micro dislocation network in as-built 316L SS. (c): STEM EDS segregation map showing Mo and Cr segregation at low angle grain boundaries [16].	33
Figure 2.18: EBSD IPF showing the distribution of $\Sigma 3$ (red) and $\Sigma 9$ (blue) boundaries in (a)(b) as built and (c)(d) annealed status of 316L SS [34]. The build direction is annotated as BD. 35	35
Figure 2.19: (a) Crystal orientation and supposed melt-pool morphology of additively manufactured 316LSS under texture control. (b)EBSD IPF map of texture controlled	

316LSS. Large blocks of grains are successfully grown in the same orientation. (c) Optical and directional reflectance microscopy micrograph of etched surface showing a QR code [37].	36
Figure 2.20: (a) 2% nitric acid etched optical micrograph of as-built M300 maraging steel. (b) SEM micrograph showing the melt pool boundaries. (c) Close up SEM micrograph showing dislocation cells [43].	38
Figure 2.21: STEM EDS segregation maps of additively manufactured MS1 maraging steel. By comparing with the bright field STEM image at the top left corner, strong Mo cell-boundary segregation can be observed in bottom left map of Molybdenum. High density of Ti-Al nanoparticles is also observed in corresponding segregation maps [44].	39
Figure 2.22: Engineering stress-strain curves of as-built and heat treated M300 samples. A trade-off between peak strength and elongation to failure can be clearly seen between as-built and aged samples. Inclined samples (coloured in green) exhibit overall inferior mechanical performance [46].	40
Figure 2.23: Secondary electron micrographs showing the partially dissolved dislocation network in M300 after substantial ageing heat treatment [49].	41
Figure 2.24: A series of studies showing how changing the chemistry can alter the deformation mechanism [57].	43
Figure 2.25: Engineering stress strain curve of TWIP steels with different grain sizes. Smaller grains lead to higher yield strength and slight reduction in plastic strain [54].	45
Figure 2.26: Grain refinement results of (a)Fe-22Mn-0.6C (b)Fe-22Mn-0.6C-3Cu and (c) Fe-22Mn-0.6C-4Cu. It is clearly displayed that increasing addition of Cu leads to finer grain size. STEM EDS map in (d) shows the distribution of Cu-nanoparticles in the TWIP steel with 4 wt.% of Cu addition. Diffraction pattern on the right indicates a single phase microstructure in the [110] FCC zone axis. (e) and (f) shows grain size and element segregation of Fe-22Mn-0.6C and Fe-22Mn-0.6C-3Cu, respectively. No grain boundary segregation can be seen, and a high population of Cu-nanoparticles are clearly visible in the 3Cu composition [55].	46
Figure 2.27: (a) Engineering stress-strain curves of Fe-22Mn-0.6C-xCu TWIP steels. The highest strength is achieved in the 4Cu composition after 5min annealing at 760°C. (b) and (d) are atomic probe tomography reconstruction of the distribution of Cu-nanoparticles at 15% and 45% strain, respectively. Detailed shearing of nanoparticles is shown in (c) and (e). As the darkfield images on the left show an increase in twin density at higher strain, nanoparticles are sheared by the formation of twins and further refine the microstructure. This process is confirmed by the STEM EDS elemental segregation maps of Cu on the right [55].	47
Figure 2.28: EBSD phase maps of Fe-16Mn-0.3C TRIP steel at different levels of strain. Significant transformation starts to occur after 20% plastic strain. The middle section of the sample shows a smaller magnitude of transformation due to being enriched in manganese [63].	48
Figure 2.29: a: Comparison of welding electrodes with different Ms and its influence on the residual stress [66]. b: Schematic diagram showing the improvement made by reducing Ms [67].	49
Figure 3.1: Geometries utilised in this study. Cuboids were mostly used for design of experiment purpose and can be further cut-off for microscopy investigations. Tensile bars	

were extracted from bar structures. The presence of as-built residual stress was revealed by the cantilever structure.....	51
Figure 3.2: Processing chamber of the Aconity Mini. The supplier sits in front of the baseplate column. Each layer the wiper blade brings new powder from raised supplier platform to the lowered baseplate platform. Excess powders are swept to the overflow.....	52
Figure 3.3: Inductive heating element installed in Aconity Lab. The baseplate can be kept at a constant temperature during the build and slowly cooled back down to room temperature after the build.	53
Figure 3.4: Thermocouple readings from top surface of the heated substrate and designated temperature in the heating element showing a steady increase in heat loss at higher operating temperature.	54
Figure 3.5: Melt-pool top view temperature contour plots of M300 steel processed at room temperature and heated bed environment. The laser scan power, scan speed and hatch space of each condition is presented alongside with the plot.	55
Figure 3.6: : Thermomechanical processing pathway of conventionally manufactured Fe-Mn TWIP steel. Cast steel sheet was homogenised at 1100°C for 2 hours and quenched in water. Cold rolling was then conducted to achieve 60% thickness reduction and the rolled sheet was recrystallised at 900°C for 3 minutes followed by water quenching.	58
Figure 4.1: (a) Schaeffler diagram prediction based on the composition proposed for this study, the present composition is predicted to yield austenite and martensite in the weld region. (b) Original Suutala diagram showing that the present TWIP steel is susceptible.....	65
Figure 4.2: Optical micrograph of the crack formed in weld test of proposed TWIP steel.....	66
Figure 4.3: Engineering stress-strain curve of cold-rolled & annealed TWIP steel.	67
Figure 4.4: Kocks-Mecking analysis of conventionally manufactured TWIP steel.	67
Figure 4.5: (a) EBSD IPF-Z of fractured TWIP steel. High density of deformation bands can be seen in the microstructure. (b)EBSD phase map of fracture sample, red deformation bands circled in white in the top left corner of (b) are indexed as ϵ -martensite.	68
Figure 4.6: XRD spectrum of as-rolled TWIP steel sheet. Both transformation products (ϵ and α') can be seen.	69
Figure 4.7: Density measured from cubes built in the DoE. All samples registered above 99% density indicate that the proposed TWIP steel exhibits good printability.	70
Figure 4.8: (a) Back scattered electron micrograph of as-built TWIP steels taken in the build direction. (b) Dislocation cell structure in the as-built TWIP steel. Nanometre sized gas pores can be seen in (b).	70
Figure 4.9: EBSD IPF-Z of as-built TWIP steel. Large aspect ratio grains contain neighbouring elongated cells with low misorientation angles. A site in the bottom right corner of the IPF containing $\Sigma 3$ boundaries highlighted in red is shown in the top right corner.	71
Figure 4.10: XRD spectrum taken from as-built TWIP steel. Note the higher intensity in (220) FCC peak.....	72
Figure 4.11: Bright field TEM micrograph showing the distribution of nano-twins in the as-built TWIP steel. The location of a grid-like finer twin intersection is highlighted in red.....	73
Figure 4.12: Bright field STEM image and EDS maps of the as-built TWIP steel. Strong segregation of Mn can be observed in (b).....	74
Figure 4.13: (a)Engineering and true stress strain curves of conventionally and additively manufactured TWIP steel, the trade-off between ultimate tensile strength and ductility can be seen in the AM built TWIP steel. (b) True stress-strain curve combined with strain hardening	

rate analysis showing the lower peak strain hardening rate of additively manufactured TWIP steel, as well as the steep decline in strain hardening rate.	74
Figure 4.14: (a) EBSD IPF with $\Sigma 3$ grain boundaries highlighted in red showing the distribution of deformation twins in the TWIP steel sample strained to 25%. (b) Phase map of L-PBF built TWIP steel showing the presence of ϵ -martensite formed in twin bands.....	75
Figure 4.15: XRD spectrum comparison between strained L-PBF built tensile bar and severely deformed TWIP steel. Absence of transformation product can be seen in the L-PBF built steel. Peaks in the as-rolls sample are labelled in Fig 4.6.	76
Figure 4.16: Bright field TEM micrograph showing high density of deformation twinning and dislocation forests. SAD insert shows diffraction spots of the FCC matrix and twin. Image taken in [110] zone axis.	76
Figure 4.17: Backscattered electron micrographs showing cavities and remaining dislocation cells in L-PBF built TWIP steel strained to 25%.....	77
Figure 4.18: Engineering stress strain curves showing the size effect in L-PBF built TWIP steel.	79
Figure 4.19: Transmission electron micrographs and corresponding drawings of the morphology of martensite inside (a) fine and (c) ultrafine austenite grains. With approximately 1 μm grain size, multiple laths with similar orientation are formed. When the grain size is further refined below 1 μm , a single lath of martensite is formed [82].	80
Figure 4.20: (a) Engineering stress strain curves of additively manufactured 316LSS. (b) Kocks-Mecking analysis of data presented in (a) showing a different strain hardening behaviour. Peak strain hardening rates were obtained after yielding and a steady decrease can be observed [16].	81
Figure 4.21: Performance comparison between the known studies of L-PBF built steels and the present study. The steels designed in the present study shows improved ultimate tensile strength when compared to legacy austenitic stainless steels and superior ductility in comparison to previously reported additively manufactured high manganese steels [16][33][84][46].	82
Figure 5.1: (a) Secondary electron micrograph showing the distribution of keyhole type defects in as-built M300. (b) Backscattered electron micrograph of as-built M300 showing solidification cell structures. Cell boundaries are highlighted due to the presence of retained austenite.	84
Figure 5.2: (a) EBSD IPF and (b) phase map of as-built M300. Insert in (b) shows a magnified region where distribution of retained austenite can be seen. The colouring of phases is shown in the legend. ImageJ calculation shows around 6.9% of austenite is present in b).	85
Figure 5.3: Off-axis imaged dislocation cell in additively manufactured M300.	85
Figure 5.4: (a) BF-STEM micrograph showing the outline of a dislocation cell. Insert SAD shows the [110] BCC zone axis with weak response of precipitates and largely confident fully martensitic matrix. (b) and (c) STEM EDS maps showing the segregation profile of Ni and Ti, respectively.....	86
Figure 5.5: EBSD phase map of M300 heat treated at 600°C for 24hrs. Insert shows partial dissolution of cell boundaries. Map acquired at a step size of 0.1 μm . ImageJ calculation shows 13% of austenite is present.	86
Figure 5.6: (a) Backscattered micrograph of the site of EDS point analysis. (b) Nickel content in grey (austenite) and black (martensite) islands, a clear enrichment of nickel in austenite	

can be seen. (c) Typical EDS spectrum of the point index, high carbon content is caused by the deposition during EBSD mapping.	87
Figure 5.7: (a) Backscattered electron micrograph of aged sample. High contrast particles are precipitates. (b) SEM EDS map of Ni.	87
Figure 5.8: Recovery in austenite during the ageing heat treatment of M300 Rapid recovery of austenite can be seen in the first 40 minutes of ageing. The recovery process terminates after 50 minutes of ageing as the maximum austenite stability is reached. Further holding led to homogenisation and dissolution of cell boundaries which caused the fluctuation in readings.	88
Figure 5.9: (a)Engineering stress/strain curve of room temperature and HB built M300 steel. Lower yield and tensile strengths are registered by the HB built specimens. (b) Transformation of austenite during tensile testing.....	90
Figure 5.10: Combined XRD spectrums of ex-situ study of the effect of surface abrasion. ...	90
Figure 5.11: Drawings demonstrating the influence of hatch spacing. The volume of weld track overlap and consequent heat affected zone is much bigger in the scan strategy with 30µm hatch spacing.	91
Figure 5.12:a) EBSD phase map and IPF map of LMD-built M300 maraging steel, FCC austenite is coloured in red and BCC martensite is coloured in green. b) Elemental segregation maps showing clear segregation of Ti, Mo and Ni at cell boundaries. The location of the segregation site matches to the location where austenite phase is indexed in a) [90]. ..	92
Figure 5.13: EDS maps of additively manufactured Fe-Mn-Al-C steel showing clear presence of band-like structures. EDS Line analysis shows coupled depletion of Mn and enrichment of Al in BCC phase areas, with corresponding EBSD phase map showing the location of measurement area [81]......	93
Figure 5.14: Schematic drawing of the effect of keyhole type melt pool. Not only does the melt pool penetrate further into the previous layer, the effect of 30µm hatch spacing is further magnified.	94
Figure 5.15: Two methods of obtaining additional austenite in additively manufactured M300. In-situ heat treatment route involves heat treating the sample through subsequent layers, whereas the aging route revert austenite after the AM process.....	95
Figure 5.16: Remaining volume fraction of austenite in a deformed/rolled metastable austenitic steel obtained with magnetic induction, X-ray diffraction and neutron diffraction. a)shows the results of samples deformed to different engineering strain at 4°C. The results obtained in samples rolled to different levels of thickness reduction is illustrated in b) [94].	96
Figure 5.17: Analysis on the factors that influence the final volume fraction of martensite... 97	97
Figure 6.1: Alloy selection in the study based on where a steel can undergo athermal or deformation driven transformation.	100
Figure 6.2: Cantilever structures built in (a) 316L stainless steel (b) Fe-Mn TWIP steel and (c) M300 maraging steel. Upward bending can be seen in cantilevers built with austenitic steels, whereas the M300 cantilever shows slight downwards bending.	101
Figure 6.3: By measuring the gap of distortion, it can be seen that Fe-Mn TWIP steel displays the highest magnitude of distortion after cut-off. This is closely followed by 316L SS which shows a similar level of angular distortion. Meanwhile, the M300 shows no distortion.	102
Figure 6.4: EDM sectioned M300 tensile bars. Significant distortion can be seen in (a) which is the top surface of the build part. Meanwhile, the tensile bar (b) sectioned below the build surface shows no distortion.....	102

Figure 6.5: Displacement diagram showing the transitioning point during the heating and cooling of additively manufactured M300. The exact temperature of austenite reversion and martensite transformation are labelled.....	103
Figure 6.6: Melt pool length simulated with the Matlab script. Overall similar melt pool lengths are observed in all three steels.....	105
Figure 6.7: Relationship between thermal strain term and the cut-off distortion observed in cantilevers. While the austenitic steels exhibit large displacement due to the thermal strain, M300 shows no distortion due to its self stress-relief capability.....	106
Figure 6.8: (a) Spatially graded 17-4PH showing rough surface in the high thermal strain region (austenite + martensite) and smooth surface in low thermal strain region (fully austenitic) (b)Relationship between the weight percent of martensite and the process driven thermal strain term [50].	108
Figure 7.1: Effect of hot isostatic pressing on the defect volume of an additively manufactured part [13].....	114
Figure 7.2: Microstructure of as-cast, additively manufactured and AM+HIP CoCrMo alloy [101].....	114
Figure 7.3: EBSD band contrast figure showing the location of the austenite crescent. FIB lift out position is highlighted in yellow.....	115
Figure 7.4: (a) variation of phase fraction shown in stacked intensities spectrum taken from the fabrication process of Ti-6Al-4V. (b) Individual spectrums taken before and after a laser hatch being laid. (c) Schematic diagram showing the relative positions of the melt pool, heat affected zone and the Synchrotron X-ray beam [102].	116
Figure 7.5: The M300 cladding deposited in Aconity Mini and the proposed shape of tensile specimen for sensor testing.	117
Appendix Figure 1: Drawing of the smaller tensile bar used in chapter 4 and 5.....	127
Appendix Figure 2: Dimensions of the larger tensile bar tested in chapter 4 and 5	127
Appendix Figure 3: IPF of (a) austenite and (b) combined phases in aged M300 sample. Area circled in red shows near-single variant transformation.	128
Appendix Figure 4: Schematics of the Feritscope testing procedure of M300 tensile specimen.	128
Appendix Figure 5: Chemical test certificate of the manganese content in conventionally processed tensile specimen.	129
Appendix Figure 6: Chemical test certificate of the full chemical composition of new and unused powder and AM built part.	130
Appendix Figure 7: 8-bit processed EBSD phase maps of a) as-built and b) 24hrs aged M300 maraging steel for ImageJ area fraction analysis.	131
Appendix Figure 8: Sensitivity test of the MATLAB script utilised in this study. A step size of 0.000005 is chosen.	131
Appendix Figure 9: Rietveld refinement calculation results and the peaks used in the calculation.	132
Appendix Figure 10: EBSD boundary characteristic map of additively manufactured 316L SS. $\Sigma 3$ boundaries are coloured in red.	133

List of Tables

Table 2-1: Processing parameters used in previous studies of additively manufactured 316L SS.	34
Table 2-2: Composition and mechanical properties of M300 and emerging maraging steels.	37
Table 2-3: Compositions and deformation mechanisms of high manganese steels.	42
Table 3-1: Chemical composition of steels used in this study.	51
Table 3-2: Chemical composition of the proposed TWIP steel at different processing status.	56
Table 3-3: Calculated martensite start temperatures of the steels studied in this project.	57
Table 3-4: Processing parameters of this study.	59
Table 4-1: Chemical composition of previously reported TWIP steels and their deformation mechanism.	64
Table 5-1: Feritscope readings taken from M300 tensile specimens at as-built, strained, polished and fractured status. A clear trend of increasing volume fraction in martensite can be seen when the sample is subject to surface alteration or strain.	89

Definition of Acronyms

Acronym	Full name
AM	Additive Manufacturing
316L SS	316L Stainless Steel
TRIP	Transformation Induced Plasticity
TWIP	Twinning Induced Plasticity
FCC	Face Centre Cubic
L-PBF	Laser-Powder Bed Fusion
LMD	Laser Metal Deposition
EBM	Electron Beam Melting
DoE	Design of Experiment
LoF	Lack of Fusion
HIP	Hot Isostatic Pressing
XRD	X-Ray Diffraction
BCC	Body Centre Cubic
BCT	Body Centre Tetragonal
HCP	Hexagonally Closed Packed
UTS	Ultimate Tensile Strength
SFE	Stacking Fault Energy
EBSD	Electron Backscattered Diffraction
LTTE	Low Transformation Temperature Electrode
EDS	Energy Dispersive X-Ray Spectroscopy
EDM	Electrical Discharging Machining
TEM	Transmission Electron Microscopy
STEM	Scanning Transmission Electron Microscopy
SPD	Severe Plastic Deformation
IPF	Inverse Pole Figure
HB	Heated Bed

1. Introduction

Steels are one of the most important engineering materials in the world. The latest method of fabricating these ferrous materials is additive manufacturing (AM), a layer by layer process that turns powder or wire feedstock into computer designed shapes. The possibility of creating complex shapes in an increased production efficiency is still driving a global research effort and fruitful results were obtained both in manufacturing and materials science perspectives.

Despite the significant advancements of AM production platforms, very few new steels were introduced to the AM market. Most decoration and general-purpose parts are being built with stainless steel powders due to their low retail prices and good all-around performances. The low carbon content in most stainless steels is also favourable to the AM processing conditions and the oxidation resistance is typically good due to the high chromium and nickel additions. A comprehensive study of additively manufactured 316L stainless steel (316L SS) was reported two years prior to this study. It marks a milestone in the study of AM as the focus shifts from satisfying with fully dense parts to more detailed studies in the microstructure and deformation mechanism of additively manufactured alloys. The study demonstrates that the mechanical properties of legacy steels were significantly improved through the AM process. However, the overall strength and ductility values of these alloys is outdated compared to newly developed advanced high strength steels.

In the last decade, successful development of transformation (TRIP) and twinning induced plasticity steels (TWIP) have led to better understanding of lower-cost manganese stabilised high manganese steels. Combined with decades of research in the effect of nano-twin formation on mechanical properties of face centred cubic (FCC) alloys, new levels of strength & ductility combinations are achieved, some researchers even stated that they have circumvented the trade-off between strength and ductility. The high strength commonly observed in TRIP-assisted medium manganese steels originates from a multi-phase, severely deformed and then recovered microstructure, where precise control of heat treatment has a profound impact on the mechanical properties of the final steel part. TWIP steels which rely on nano deformation twins require grain refinement to achieve excellent uniform elongation. In addition to the complexity in thermal mechanical processing, the high manganese content and the low vapour pressure of manganese has limited the usage of these steels in conventional processing. In comparison, powder-based AM production has great advantages in the simplicity of fabrication process and a combination of good strength and ductility in the “as-built” status. The strength of 316L printed in laser powder bed platform even surpasses ultra-fine-grained counter parts which

have limited ductility. Therefore, AM has the potential to circumvent the trade-off between strength and ductility of TRIP/TWIP steels without the need of complex thermomechanical processing. The performance of the “as-built” steels can be further adjusted with appropriate heat treatment which enables additional flexibility of these steels. However, very few groups have attempted to introduce these two classes of manganese-based steel into the study of additive manufacturing. Fewer, if any, have investigated designing a variation of such alloy specifically for additive manufacturing. In the author’s opinion, the study of TRIP/TWIP steels with AM technology can fill a gap in the understanding of state-of-the-art steels in AM and provide insight to manufacturing body-in-white parts with AM at a better performance/cost ratio.

In this study, the current progress of research in commercially available and novel steels will be reviewed to identify necessary materials characteristics of a steel that is suitable to additive manufacturing processing environment. An alloy will then be designed following conventional welding metallurgical criteria, as well as the latest insights in the design of advanced high manganese steels. The final aim is to demonstrate the aspect of functionalise additively manufactured metastable steels and explore any further potential of AM as a disruptive technology.

Following these perspectives, a series of quests have been set up:

- Review the current progress in utilising ferrous materials with AM production method.
- Design a TRIP or TWIP steel with superior mechanical performance compared to commercially available stainless steels.
- Investigate the effect of self-stress relief capability of TWIP and TRIP during the additive manufacturing process.
- Suggest an application for metastable transforming steels produced by AM.

Chapter 2 will cover the latest progress of steels in additive manufacturing. A wide range review of commercially available steels processed with AM will be conducted. Their performances will be compared to advanced steels such as the above-mentioned high manganese TRIP/TWIP steels and CrCoFeNi series high entropy alloys. By investigating the success in these alloys, one can identify the suitable microstructure and chemical composition for an easy-to-print and strengthened-by-process steel that is largely benefited by the AM process. Experimental procedures are detailed in chapter 3.

The application of advanced high manganese steels for AM will be described in chapter 4. This includes comparing the mechanical properties of cold rolled specimens of the proposed composition with the AM-processed counterpart.

Chapter 5 illustrates a case study for additively manufactured M300 maraging steel, which represents the characteristics of both martensitic and TRIP-assisted steel. Key points such as phase stability and the effect of self stress-relief will be investigated. The utilisation of the metastable martensitic transformation observed in this class of steels will also be discussed in chapter 6, where cantilevers were built in three steels with different martensite start temperatures.

Chapter 7 will conclude the findings in this thesis and outline unfinished work due to the Covid-19 pandemic.

2. Literature Review

2.1. Metal additive manufacturing: Fundamentals

The development of metal additive manufacturing started with sintering of powder at intermediate temperatures and gradually transformed to melting of powder or wire/rod feedstock well above the solidus temperature. The heat source utilised in metal AM machines are most likely to be either laser or electron beam though the development of diode heating printers is also promising. Laser has long been used in the welding of metals. Depending on the doping mechanism of feedstock, powder-based laser additive manufacturing can be further separated into laser powder bed fusion (L-PBF) and laser metal deposition (LMD). When compared to the powder bed platforms, LMD machines tend to have a much larger processing chamber. As a result, extra degree of freedom can be achieved by either introducing a 5-axial movement baseplate or a robotic-arm style laser & dosing module. The differences of powder delivery are shown in Fig 2.1. Electron beam melting (EBM) is another popular choice in the welding and joining of large metallic parts owing to the large depth of penetration of the electron beam. A good vacuum condition is required thus the popularity in the employment of EBM in fabrication of titanium components. Due to the underlying physics however, electron beam melting (EBM) devices are mostly utilised for the fabrication of paramagnetic austenitic steels [1][2]. Fig 2.2 shows the complex electron beam focusing system in an EBM device [2].

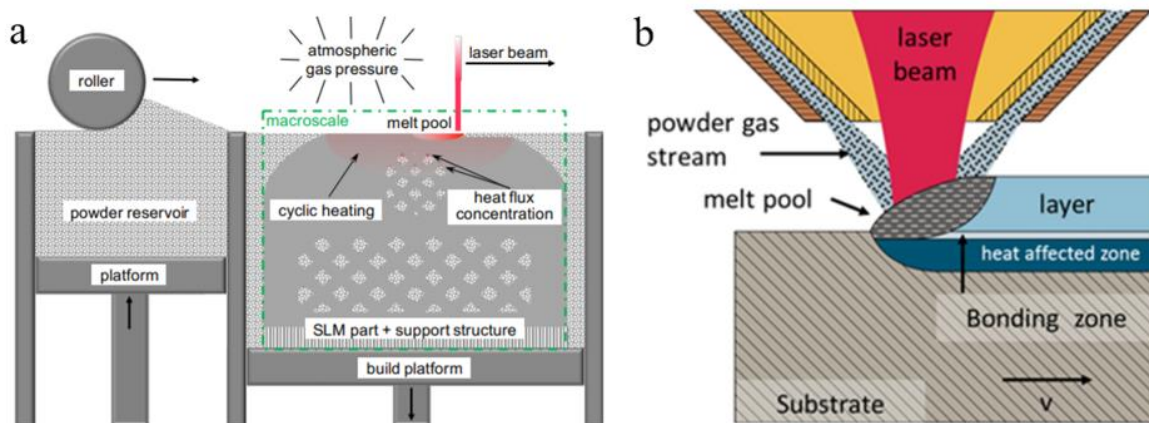


Figure 2.1: a typical setup of a powder bed fusion system with indication of melt region and operating environment [10]. b: Experimental set up of a laser powder deposition System [3].

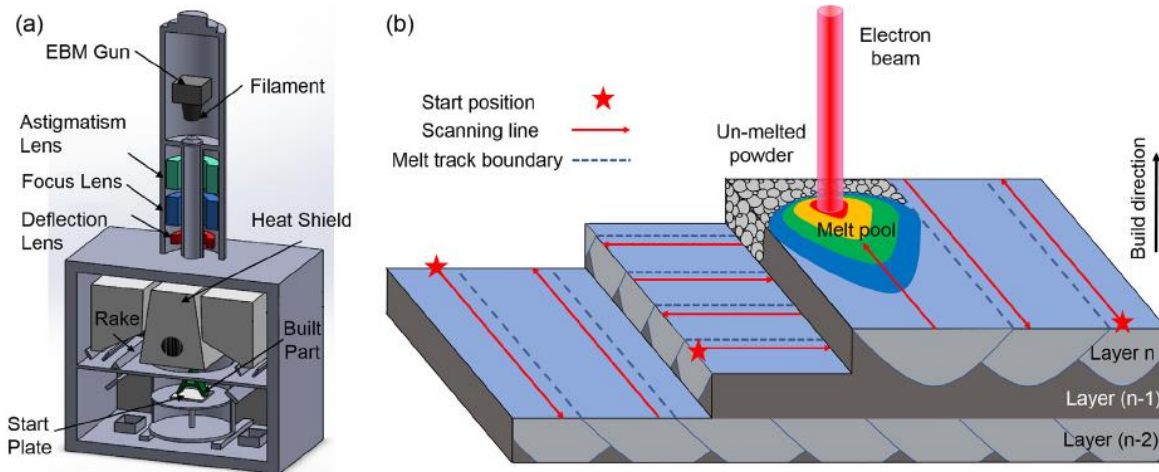


Figure 2.2: Schematic graph of an Arcam EBM device, a set of magnetic lenses guides the electron beam through to the build chamber. b: Typical build scenario with EBM. The overlap of melt pools are illustrated with dashed lines [2].

Fayazfar et.al summarised that L-PBF is the most favoured technique when it comes to research of steel [4]. This popularity attributes to the ease of operation and small printing volume which favours small scale research. The “constant” in all L-PBF machines is the baseplate which situates horizontally, and the fabrication process happens while the baseplate moves down in the Y-axis. The variables in the additive manufacturing of metals strongly affect the build quality and the final performance of the build part.

To repeat the melting of each layer continuously and successfully, the amount of powder dosed onto the substrate must be precisely controlled. This is often carried out with a wiper blade made of carbon fibre or rubber. The height of the powder bed is usually adjusted based on both the quality of the powder and the depth of melt pools. For a batch of $15\mu\text{m} - 45\mu\text{m}$ powder, the layer thickness can be set to $30 - 40\mu\text{m}$. Once the chamber condition has been reached, the laser beam will travel in the path designated in the stereolithography (STL) file. Generally, a handful of parameters can be altered in accordance with the processed alloy powder and part geometry. The spacing between the laser scan tracks is referred as hatch spacing, this value is adjusted based on the width of the melt pool so that an adequate melt pool overlap (partial remelt of the previous melt pool) is achieved consecutively. Laser power and scan speed are the most dominant parameters that can be easily adjusted. As faster layer completion time directly results in shorter total build durations, optimisation based on high laser scan speed is often desired by the industry and thus the introduction of high laser power L-PBF machines. On the contrary, lower scan speeds are almost compulsory in some of the Operando studies since the synchrotron beam cannot move at the speed of the laser [5]. For alloys with poor

printability, laser scan speed is carefully adjusted so that a steady melt pool is maintained. Alongside with layer thickness, which is not adjusted very regularly, laser power, hatch spacing and laser scan speed form the basics of processing parameters.

In addition to the scan parameters, the scan strategy is chosen and often repeated at an angle in the consecutive laser. Fig 2.3 shows the differences between four commonly used scan strategies.

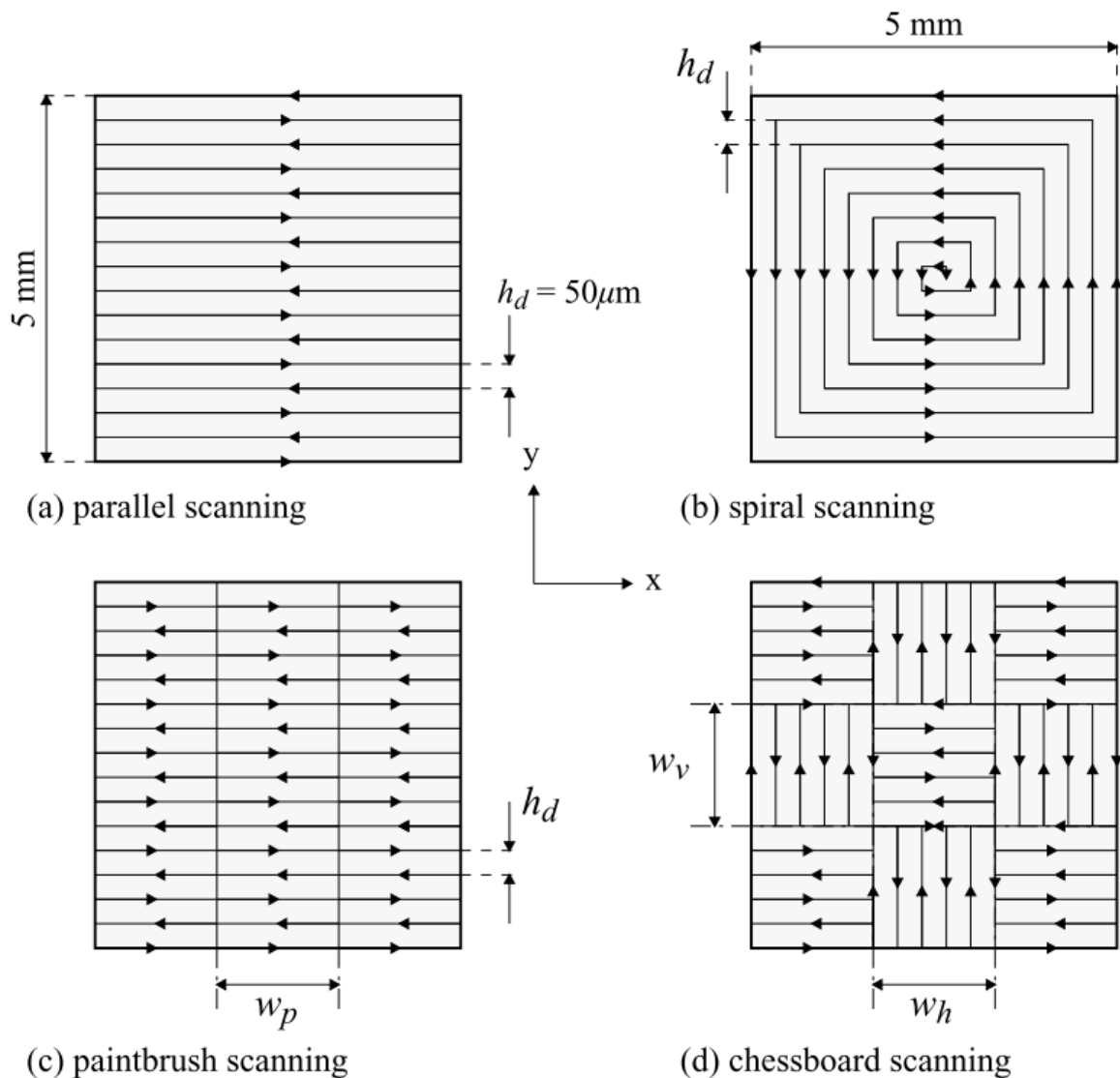


Figure 2.3: Visualisation of scanning strategies. Poor overlap or miss-alignment of islands in the strategy shown in (c) and (d) can lead to severe cracking [6].

After hundreds or thousands of repeats, a metallic part submerged in powder can finally be extracted from the machine. The product of the AM process at this point is often referred as “As-built” and the study of additively manufactured metals starts from here. In general, physical density of a part is the most practical way to evaluate the degree of success in AM.

This can be achieved by methods such as Archimedes density measurement, pycnometer and advanced image analysis on the area percentage of defects. While Archimedes' method tends to be the easiest to carry out, rough surfaces of additive manufactured parts can result in significant error in the measurement. Image analysis and pycnometer are likely to provide higher accuracy in results, but the analysis volume/area is much smaller compared with that of Archimedes method.

Mechanical performance is vital to any structural material. With metal additive manufacturing, it is found that the tensile properties are strongly dependent on the volume of defects in the as-built part. To achieve densification, the design of experiment (DoE) approach is most often used to determine the response of the material to a certain set of build parameters. When comparing different set of processing parameters, a term is used to represent the combined effect of laser powder, laser scan speed and hatch spacing: energy density (E_v).

In most cases, this term is defined as:

$$E_v = \frac{P}{L_h V_s H_L} \quad (2.1)$$

where P represents the power of the laser, L_h and H_L indicate the hatch distance and layer thickness, respectively. The scan speed of the laser is defined by V_s . Layer thickness and hatch spacing are crucial factors in build strategy design as they strongly affect the thermal history on each layer.

Suitable processing parameters can be found after running DoEs with numerous combinations of above variables. However, one must remember that E_v cannot be used to directly translate processing parameters between machines equipped with different modes of laser. Some L-PBF machines utilise pulsed laser and further adjustment to the E_v term is needed due to the ramping-up and turning-off of the heat source in between designated exposure spots. While the DoE approach is applicable to most materials with good printability, multiple runs are required for alloys with small processing windows. It is therefore important to understand the origin of defects in AM and how the chemistry of alloys can affect the defect formation. The following section will cover the typical defects found in metal additive manufacturing.

2.2. Defects in L-PBF

During the rapid heating-cooling cycle of laser additive manufacturing, a wide range of defects can emerge due to sub-optimum processing parameters or non-ideal alloy chemistry. This section will review common defects found in additively manufactured steels.

2.2.1. Porosity and inclusions

Densification is one of the most important steps of AM. The main cause of low density in metal additive manufacturing is porosity. The shape, cause and elimination of porosity will be discussed in this section.

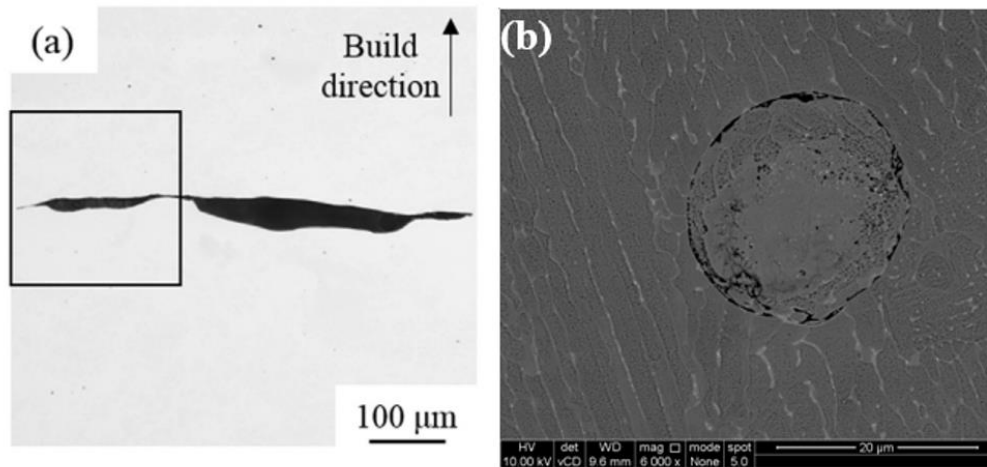


Figure 2.4: (a) Optical micrograph showing a lack of fusion defect found in 304 stainless steel [7]. b: Scanning electron image showing an un-melted powder embedded in a nickel-based superalloy matrix, courtesy to Liu Cong for the image.

When powders are insufficiently melted, lack of fusion (LOF) defects are formed. Fig 2.4 shows two types of LOF type defects, where the shape of the crack is distinctively different. To reveal the formation mechanism of LOF defects, *in-situ* and *operando* observations were made in platforms specifically designed to allow synchrotron imaging and diffraction to take place either during or in-between the melting and re-supply of layers. Fig 2.5 shows the development of consistent lack of fusion type defects. It can be seen that due to the particle size distribution, layers were fused but large gaps can be seen when consecutive layers were connected by large particles. This type of defect can be effectively eliminated with appropriate powder quality and design of experiment approach to achieve optimum melt pool depth.

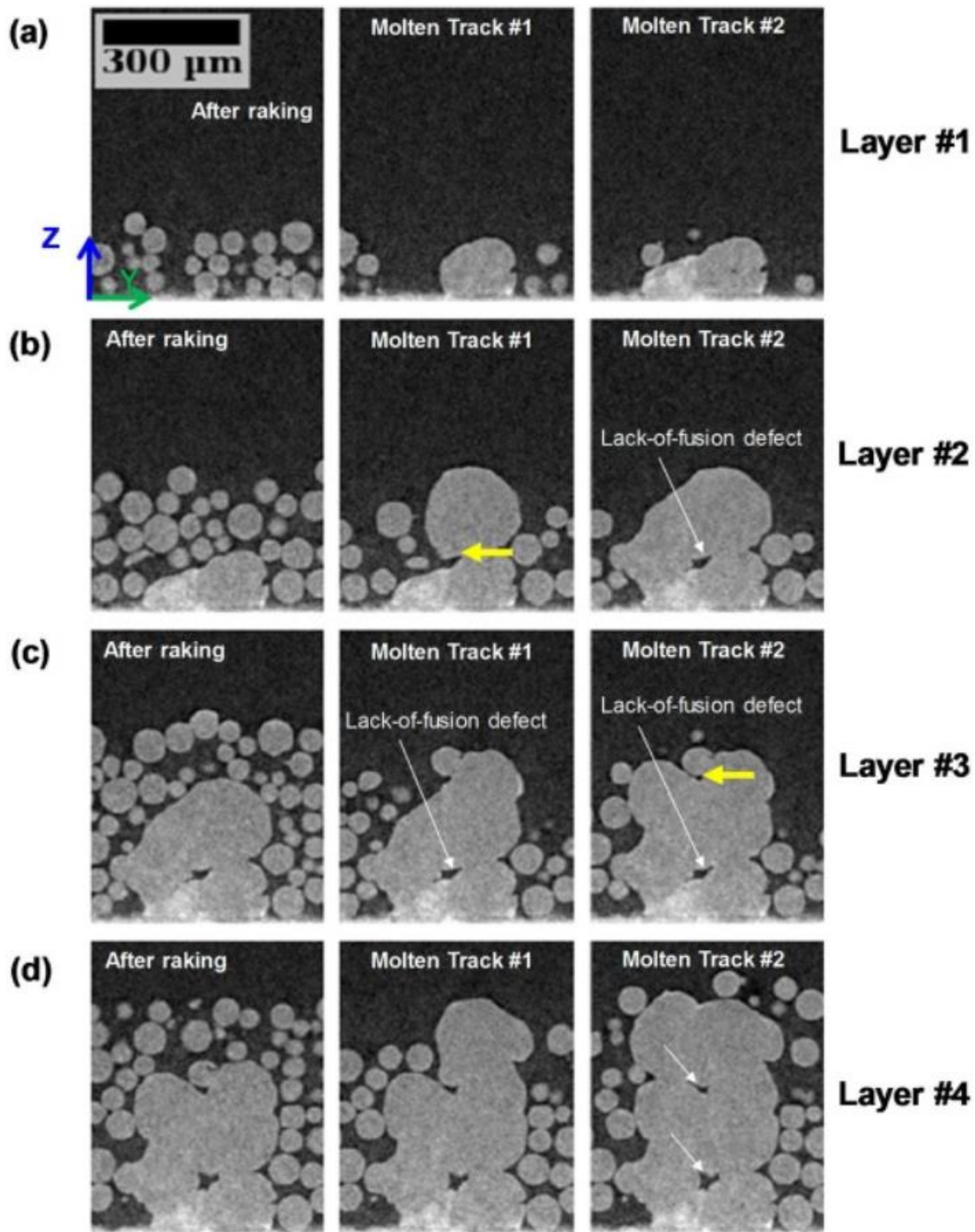


Figure 2.5: In-situ observation of the development of LOF defect due to insufficient melting. The wide range of particle size distribution also contributed to this effect as LOF defects are formed between the previous layer and large particles [8].

When too much energy is put into the AM process, the melt pool changes to a keyhole shape and without further tailoring of parameters, these keyhole melt pools can form voids and result in large areas of vacancies. This type of defect is often referred to as keyhole porosities. The differences between conduction and keyhole mode melt pools are shown in Fig 2.6.

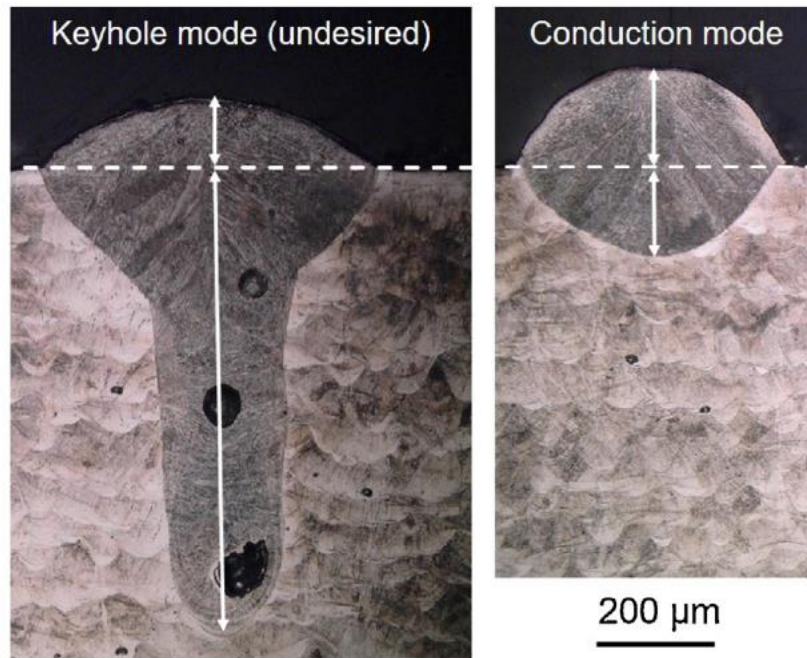


Figure 2.6: Optical micrograph showing two types of melt pools in additive manufacturing. Note the keyhole defects in the stem region [9].

The evolution of melt pool shapes is demonstrated in Fig 2.7. Once the melt pool reaches the melting temperature, the vapor depression phenomenon occurs and starts to penetrate deeper into the material. A shape change can be observed in Fig 2.7i where the melt pool changes from semi-circular to irregular and eventually a keyhole shape is achieved.

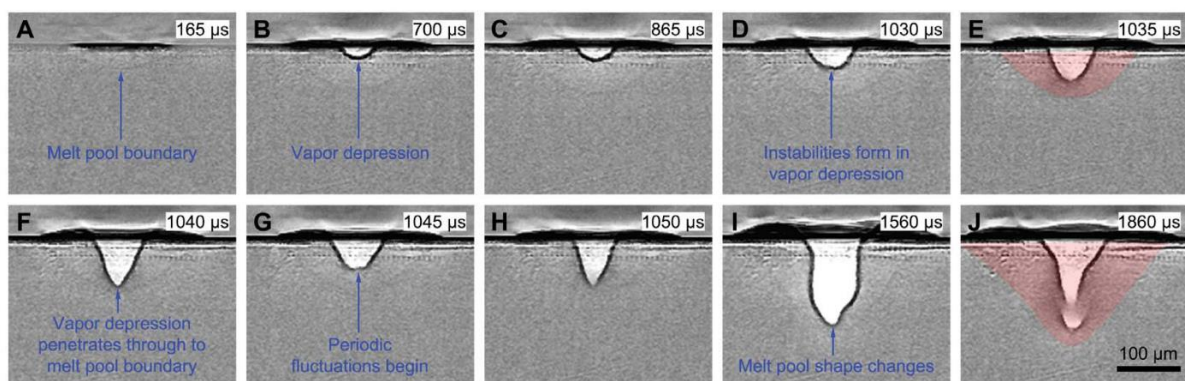


Figure 2.7: In-situ observation of the formation of vapour depression and further development of melt pool shape due to the movement of the vapour depression zone in the laser melting of a solid block of Ti-6Al-4V [10].

The real time imaging of the AM process revealed the specific formation sequences of a keyhole defect. As illustrated in Fig 2.8, the Marangoni and recoil flow altered the movement of powder, droplets and the melt pool itself, which effectively severed the flow of the melt pool and thus leaving cavities at the bottom of the melt pool.

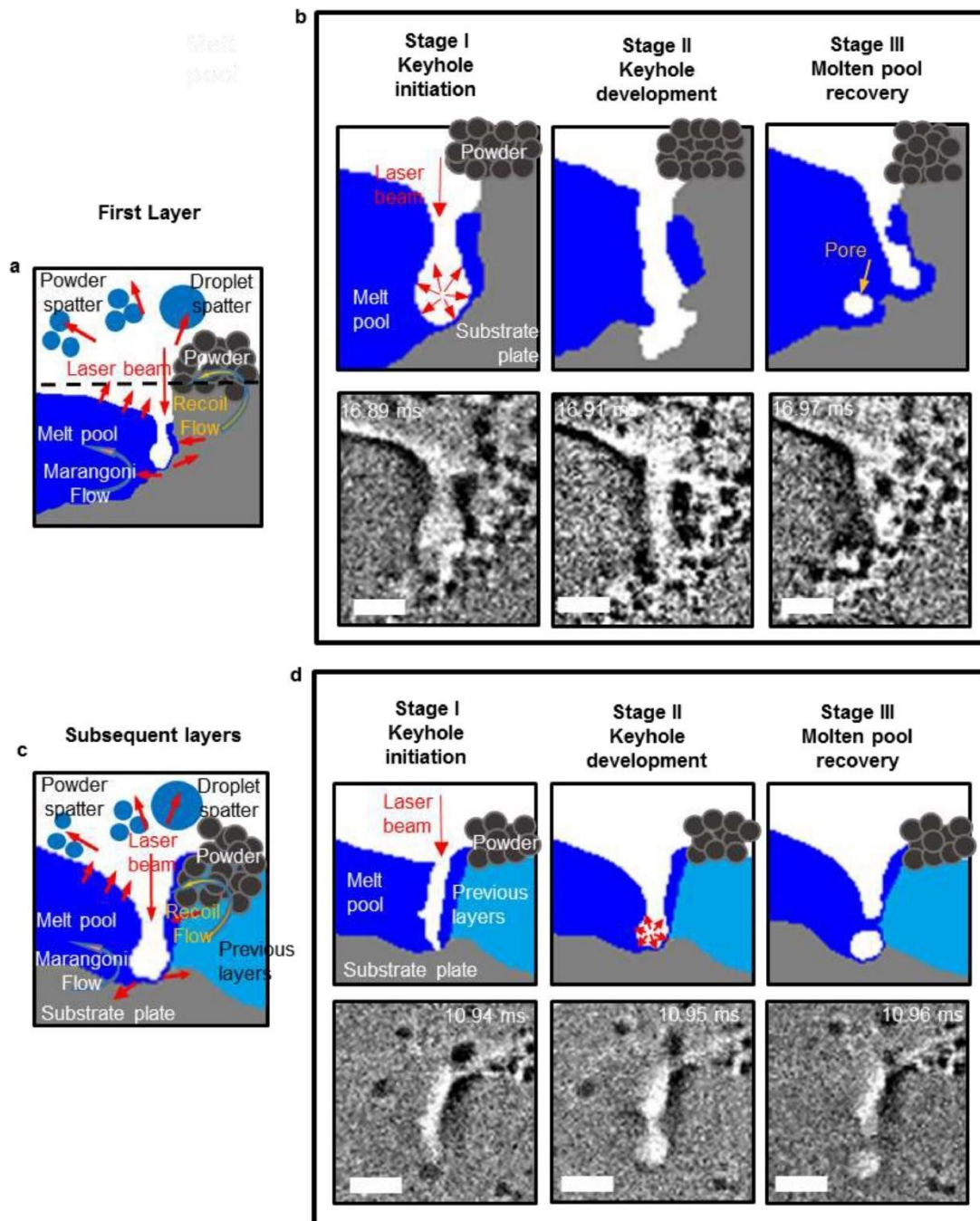


Figure 2.8: In-situ observation of keyhole melt pool in L-PBF built Ti-6Al-4V. The evaluation of the melt pool was separated into three stages. The first stage mainly involves the establishment of the keyhole melt pool [11].

Another type of pores are formed by shielding gas trapped inside viscous liquid metal. This type of defect is most often observed post build as it is mainly attributed to non-optimised processing parameters. In practice, LOF and keyhole type defects can be avoided by the design of experiment approach for parameter refinement. Post-build processing techniques such as hot isostatic pressing (HIP) can very effectively further reduce the porosity in additively manufactured parts [12]. However, it is worthwhile noting that trapped gas pores with high

pressure may grow back to its original diameter if additional heat treatment is applied after the HIP process [13]. For keyhole type defects, criteria are created to specify the formation and the aspect ratio of the keyhole, as demonstrated in Fig 2.9 [10][14].

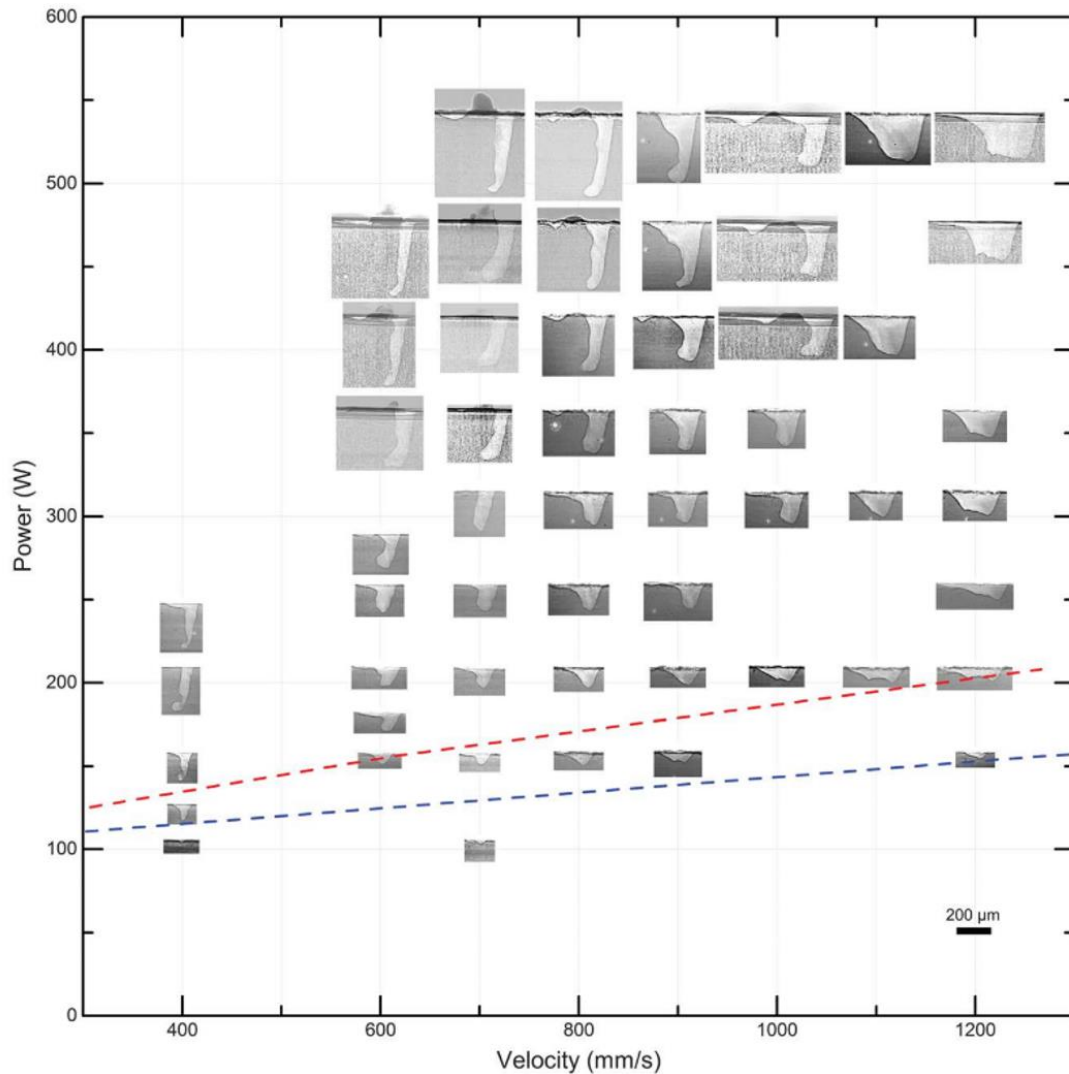


Figure 2.9: Plot showing how power and scan speed of the laser affects the shape of the keyhole. Note the conduction mode melt pool below the blue line [10].

Intermetallic and oxide inclusions can also be present in additively manufactured steels. While inclusions tend to be observed in dislocation cell walls in 316L SS, oxide inclusions in M300 can also be found in cell interior, as demonstrated in Fig 2.10. Although the processing chamber is purged before the scanning cycle begins, some degree of oxygen may be present in both feedstock supplier chamber and the alloy powder itself. L.Thijs et al. studied the effect of building M300 maraging steel in both pure N_2 and N_2+O_2 environment and the results suggested that a high population of TiN and TiO inclusions formed in the most recent scanned

layer [15]. This shows that the shielding gas also has a pronounced influence on the inclusions formed due to the AM process.

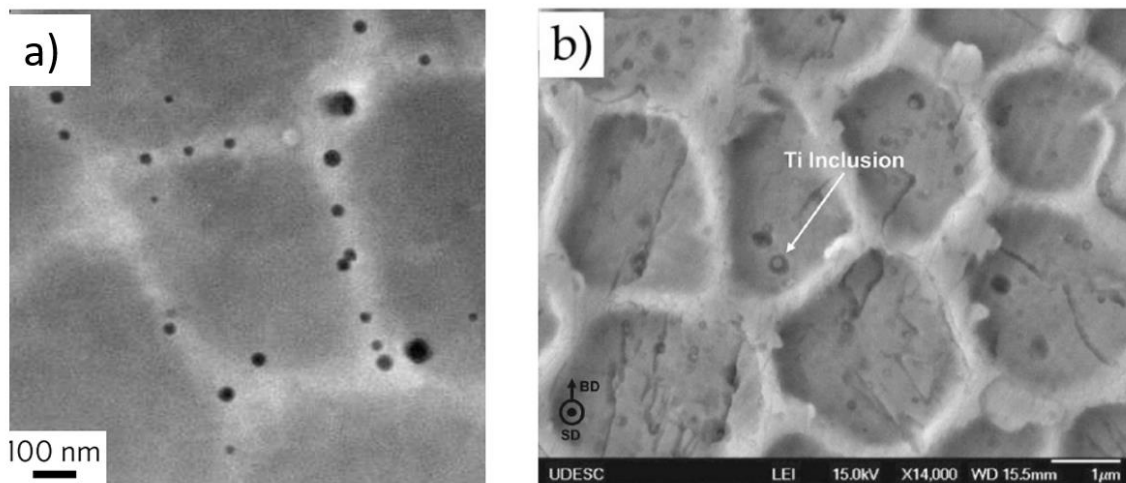


Figure 2.10: a) SiO inclusion observed in as-built 316LSS. b) TiO inclusion in aged M300 maraging steel [16][17].

2.2.2. Cracking

Cracking is one of the major challenges in introducing high performance alloys to laser additive manufacturing. Solidification cracking can occur in alloys with large freezing range when the mushy zone is subject to tensile stress [18]. For ferrous materials produced by additive manufacturing, cracking is less common in steels with good weldability [19]. However, high carbon steels such as H13 could exhibit solidification cracking [20]. To provide vital information on designing steels for AM, some of the key welding criteria and diagrams for crack susceptibility predictions will be reviewed.

Thermally induced cracking is commonly found in materials with high crack susceptibility. For ferrous materials, the susceptibility of solidification cracking can be estimated with a Suutala diagram, where the axes are formed with carbon percentage and Ni/Cr equivalent [21]. Combined with the Schaeffler diagram which helps predict the solidification pathway, one can choose the correct pre-heating conditions and arc movement speed for optimum welding results. This method worked reasonably well with conventional arc welding, where the heat source is often an electric arc moving at slow speeds. Modern welding techniques have heat sources travelling at much higher speed with much larger higher depth of penetration. This has had an impact on the use of conventional welding metallurgy diagrams. Lippold studied the solidification behaviour of austenitic stainless steel where a shift in Suutala diagram was made to fit the new solidification results [22]. As shown in Fig 2.11, the line separating crack and

non-cracking welds has shifted to the right. This shows that steels that are not predicted to crack under conventional arc welding environment can be susceptible to solidification cracking when welded with laser heat source.

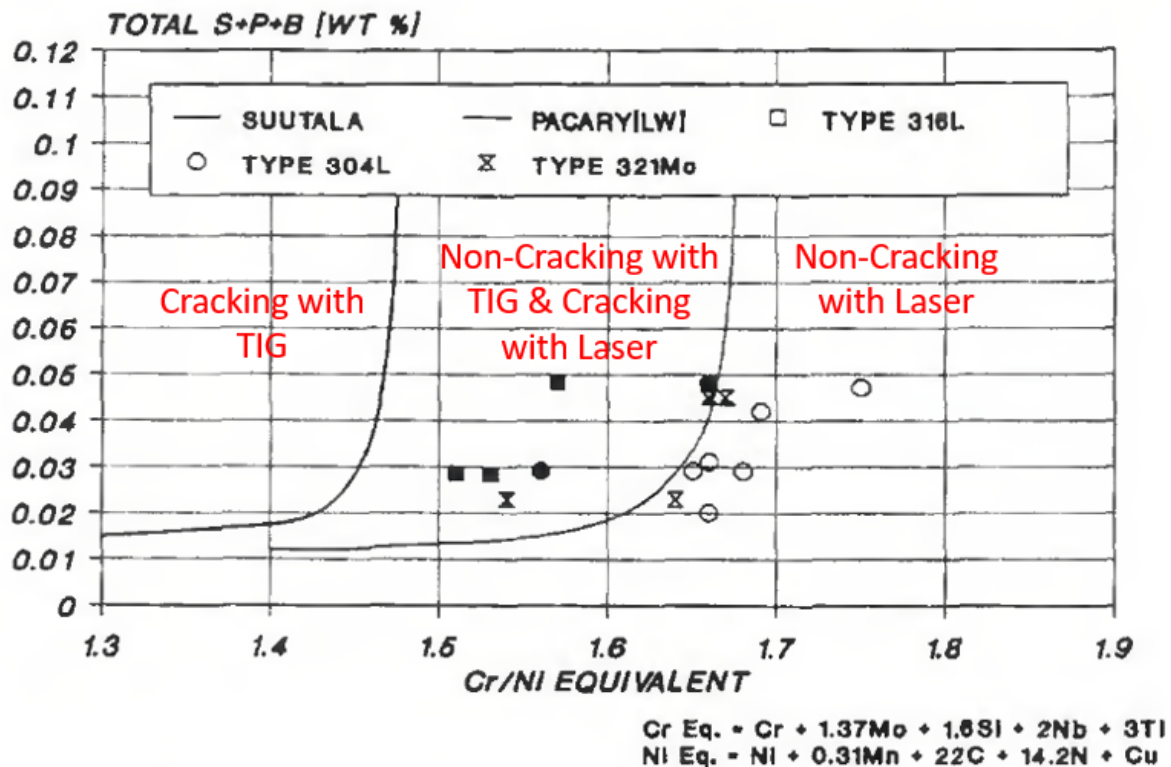


Figure 2.11: Modified Suutala diagram of pulsed laser welding. Note the shift in trend line between the laser welding result and TIG welding condition [22].

Zambon and Bonollo have shown that some of the welding empirical equations are no longer suited for solidification rate in the range of 10^4 to 10^6 K/s [23]. These studies are showing the lack of consistency when using conventional welding models for evaluation of the performance of novel alloys in AM. However, this should not stop alloy designers from using the Suutala and Schaeffler diagrams as a rough estimate for the possible printability and phase constitution of an alloy after the AM process.

2.2.3. Residual stress

Residual Stress is commonly found in AM parts in the form of distortion. Withers and Bhadeshia have shown that residual stress has an important role on the fatigue life of engineering materials [24][25]. During an AM build, thermal residual stress is formed due to the difference in thermal expansion coefficient in adjacent layers. Thermal expansion will occur on the surface regardless of the degree of melting (sintering or fully molten), which induce a residual stress on the previous layer. This type of residual stress is categorised as

heating stress. Solidification of the top layer will introduce residual stress due to shrinkage, which is named cool-down residual stress [26]. These two mechanisms are presented in Fig 2.12. Characterisation of residual stress can be achieved by destructive cutting samples and examining the curvature. Other measurement methods include *in-situ* X-ray diffraction (XRD) and digital image correlation, which reveals the evolution of residual stress during the manufacturing or deformation process.

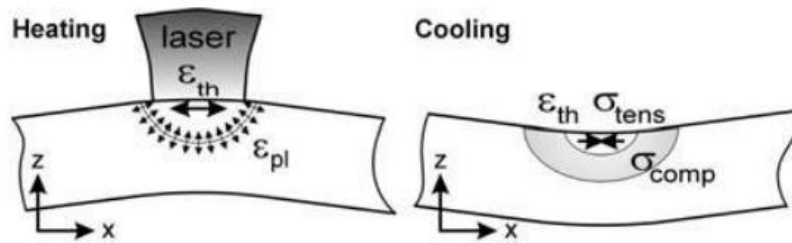


Figure 2.12: Modes of residual stress in relation to the rapid heating and cooling during the L-PBF process [26].

Shape distortion is the most common consequence of large magnitudes of residual stress in AM built parts. To visualise the magnitude of residual stresses, a cantilever structure can be prototyped and distortion upon sectioning can reveal the presence of residual stress. This structure can also be used to demonstrate the effect of heated substrate, as shown in Fig 2.13.

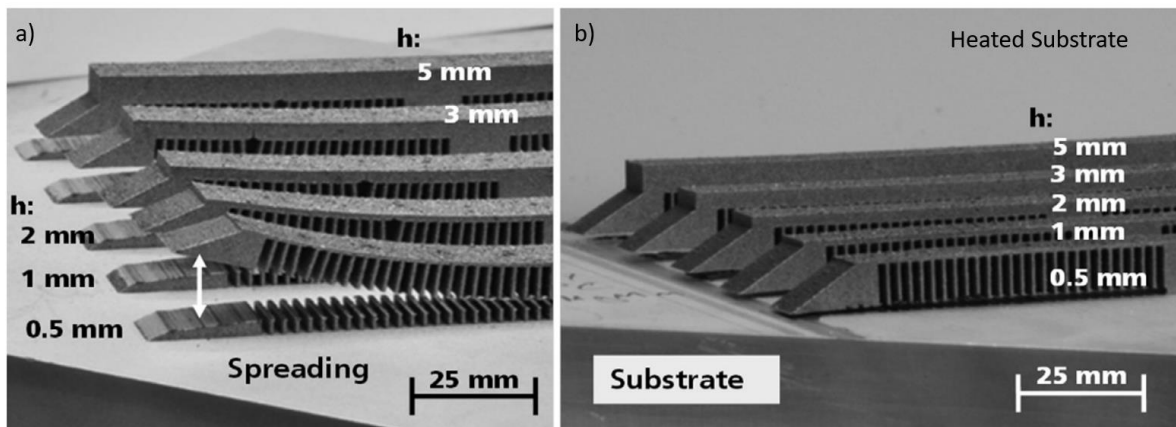


Figure 2.13: Elimination of residual stresses achieved by using a heated substrate, no distortion is seen in b) [27].

2.2.4. Conclusion

To summarise, porosity, cracking and residual stresses are key defects present in additively manufactured steels. In addition to processing parameter optimisation, post build treatments such as HIP and stress-relief annealing can eliminate the presence of these two types of defects

to a great extent. The crack susceptibility of an alloy is closely related to the chemical composition. While build modifications such as heated substrate and layer rescan have been proven effective in improving the build quality, metallurgical adjustments can directly eliminate crack formations. Therefore, one can suggest that for an alloy to perform reasonably well in AM, it must be metallurgically suitable for the AM process. To confirm this statement, the printability and mechanical properties of a wide range of steels will be investigated.

2.3. Basic understanding of steels

Steels are commonly regarded as the product of iron alloyed with neighbouring and interstitial elements. The phase diagrams shown in Fig 2.14 showcase a wide range of phases that can be present in steels.

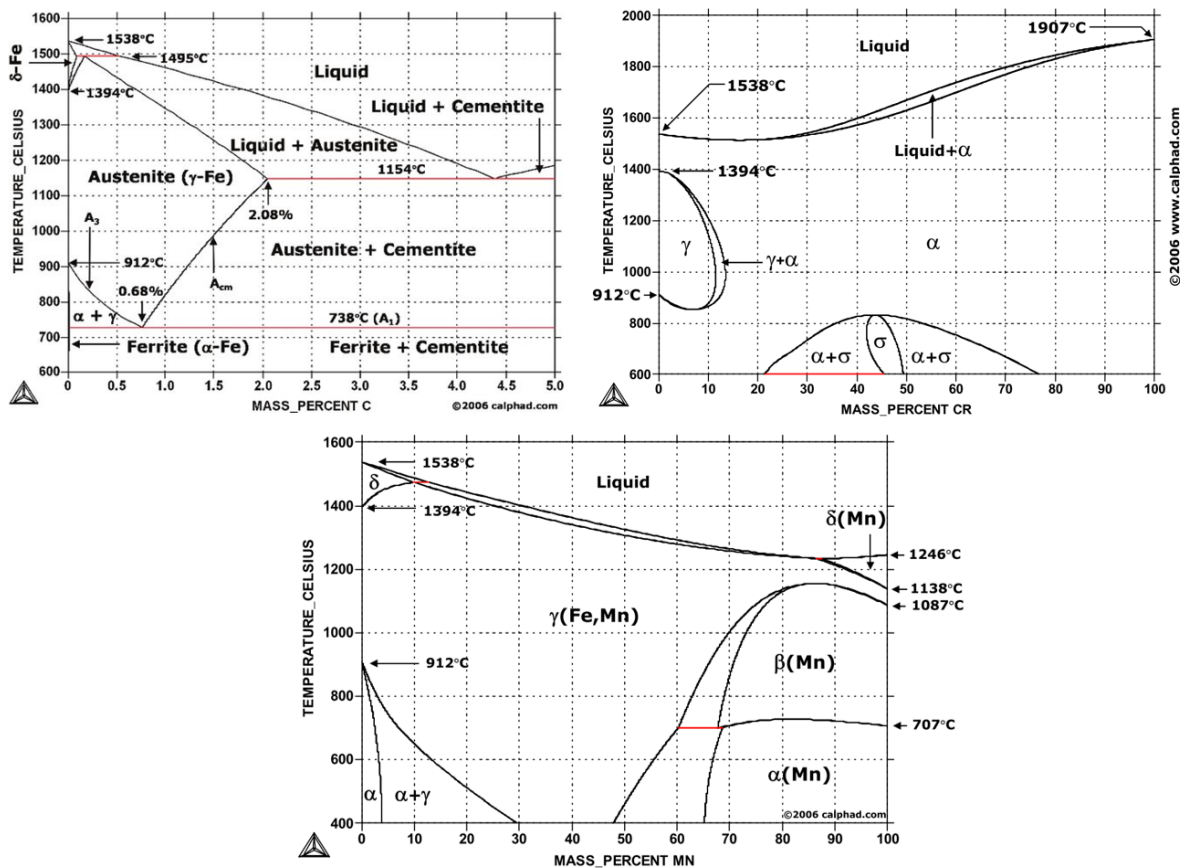


Figure 2.14: Typical Fe-C, Fe-Cr and Fe-Mn phase diagrams [28][29][30].

Face centre cubic austenite is a high temperature phase that can be retained at room temperature. Stainless steels such as 316L and 304S can exhibit a fully austenitic matrix at room temperature due to the significant addition of chromium and nickel. Further transformation can take place in metastable austenitic steels, the mechanism will be introduced later on in this chapter.

Body centre cubic or tetragonal (BCC/BCT) martensite is a transformation product of austenite under rapid cooling. A proposed model of lattice accommodation is illustrated in Fig 2.15. Since the transformation takes place in specific habit planes, the transformation product shares a specific orientation relationship with the parent austenite grain and there are in total 24 possible variants for martensitic transformation in ferrous materials. When the parent grain is sufficiently large, multi-variant martensite can be present and this is commonly regarded as packets. Another type of deformation induced martensite is hexagonally close packed (HCP). More details will be discussed in the following section.

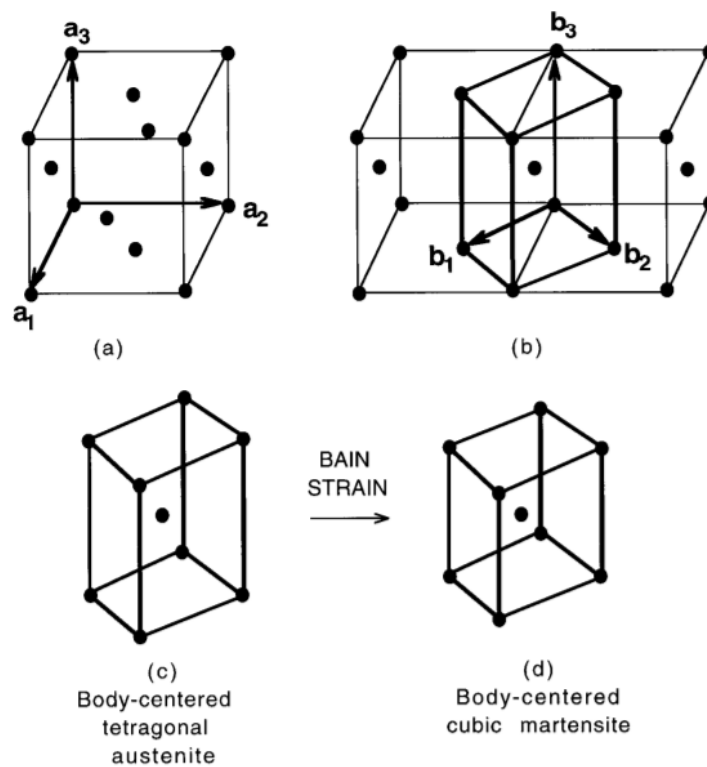


Figure 2.15: Bain strain approach of understanding the existence of a body centred tetragonal unit cell inside FCC lattice [31].

Apart from the well-known allotropic phases of iron, there are structures known as pearlite and bainite which lead to super strong and wear resistant steels. Hexagonally close packed iron can also appear in steels as a transformation product, which will be discussed further in later sections.

2.4. Current progress in additive manufacturing of steels

A wide range of commercial steels are currently being studied with AM technologies. Figure 2.16 shows two pie charts of steel researched with L-PBF and LMD. It can be seen that 316L stainless steel received high attention in both platforms. While precipitation hardened M300

maraging steel is heavily studied with L-PBF technology, low-cost Hadfield steel and carbon-rich tool steels are more popular with blown powder studies. This is due to the lack of recycling in LMD platforms as most off-substrate powder is treated as waste.

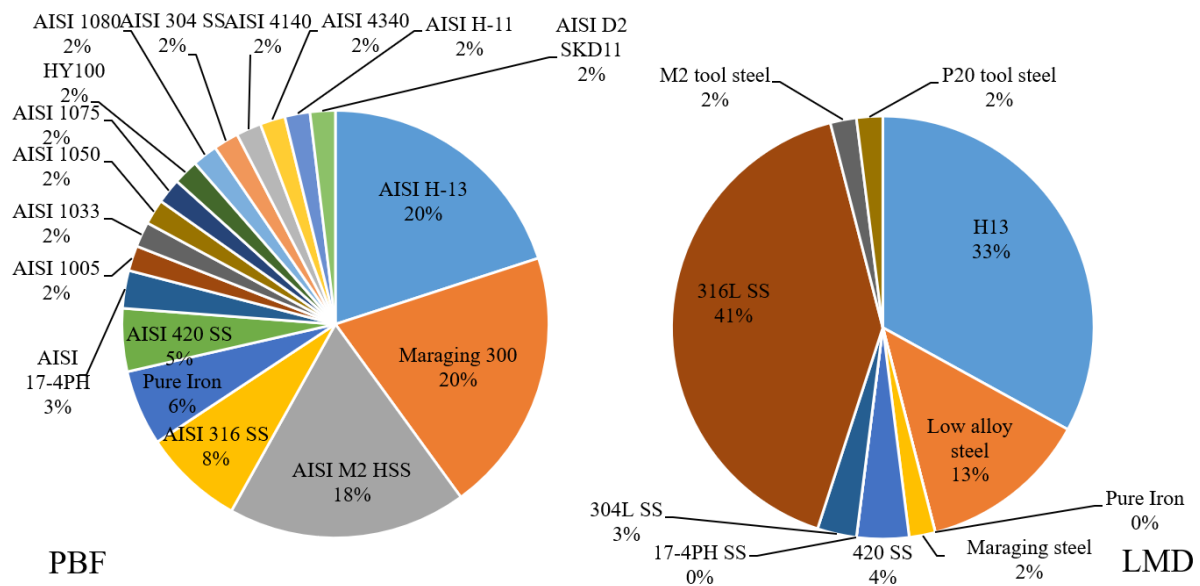


Figure 2.16: Two pie charts showing the grades of steels studied with powder bed fusion and laser metal deposition, despite the similarity in composition. Reproduced from [4] .

Due to the high popularity in research, 316L SS and M300 maraging steel will be reviewed in detail in the following section.

2.4.1. 316L stainless steel

Austenitic stainless steels are widely studied in AM due to their vast application range. From cutlery to nuclear reactors these ductile and corrosion resistant alloys are perfect candidates for complex operating environments. Wang et al. conducted systematic studies on L-PBF built 316L SS and revealed a hierarchical microstructure which results in simultaneous improvement in both strength and ductility [32][16]. The yield strength in particular increased from 160 MPa of the cast state to 590 MPa in the as-built sample. High density of deformation nano-twin was observed which contributes to the significant plastic strain. It was also discovered that some elements are segregated at cell boundaries due to high cooling and growth rate. Fig 2.17 shows a comparison between the tensile properties of additively manufactured and cast 316L SS and the microstructure which the yield strength increment arises from. Another investigation of the deformation mechanism of 316L SS showed that the low angle grain boundaries which assemble the dislocation network can provide certain level of resistance to twin-gliding

dislocation [33]. These dislocation cells remain present in the microstructure even at high plastic strain which enabled the high elongation to failure in additively manufactured 316L SS.

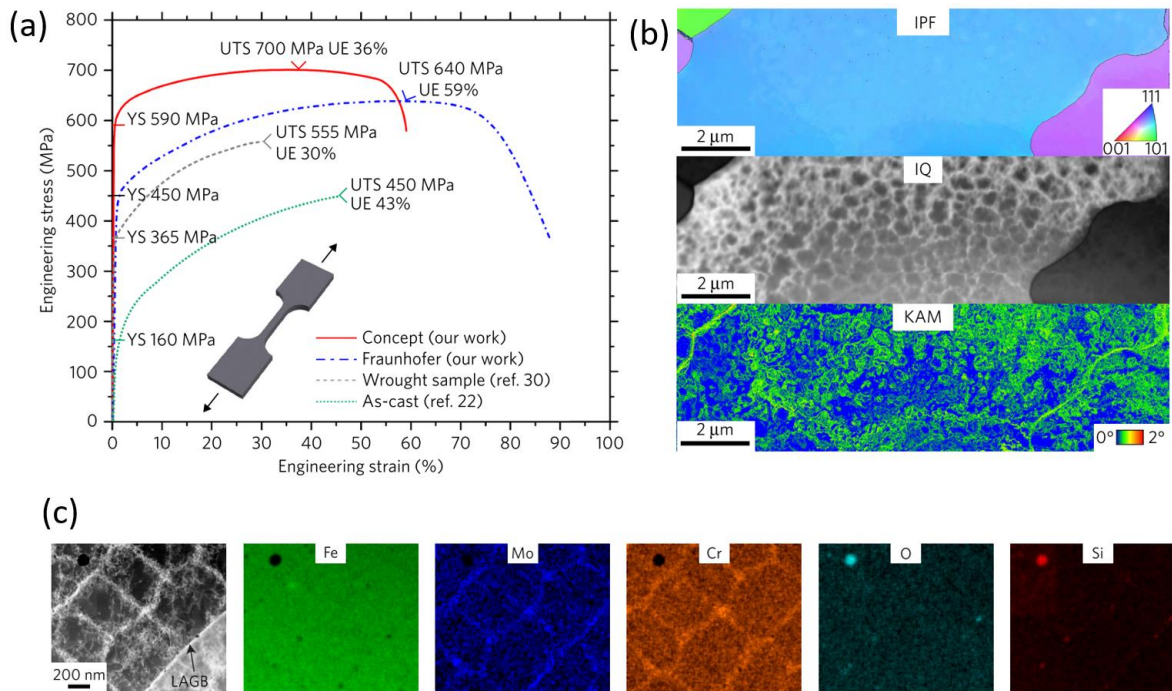


Figure 2.17: (a): Mechanical properties of additively manufactured 316L compared to conventionally processed counterparts. (b): Precession electron diffraction images showing large grains and sub-micro dislocation network in as-built 316L SS. (c): STEM EDS segregation map showing Mo and Cr segregation at low angle grain boundaries [16].

In addition to the sub-micron features, additively manufactured 316L SS possesses elongated grains and the characteristics of high angle grain boundaries are strongly dependent on the processing parameters. As shown in Fig 2.18, Laleh et al. observed high population of $\Sigma 3$ and $\Sigma 9$ grain boundaries in additively manufactured 316L [34]. To illustrate the difference in processing conditions, the parameters used in previous studies of 316L are listed below in Table 2-1.

Table 2-1: Processing parameters used in previous studies of additively manufactured 316L SS.

Author	Laser power(W)	Scan speed (mm/s)	Hatch spacing (μm)	Layer thickness(μm)	Beam radius (μm)	Energy density (J/mm ³)
Wang et al. [16]	150	700	105	30	54	68
Wang et al. [16]	296	150	100	50	207	395
Liu et al. [33]	200	850	100	20	70	118
Laleh et al. [34]	150	400	80	30	?	156

In Table 2-1, a significantly higher energy density was calculated from the “Fraunhofer” parameters [16]. This was mainly due to the effect of large laser beam radius, which is not part of the consideration of the conventional energy density equation. To mitigate the effect of additional parameters, advanced processing maps and normalised energy density calculations were created [35]. The energy density of parameters used in Laleh’s study is 230% higher than that of the “Concept” parameters reported by Wang et al., which fits the story that these coincident site lattice (CSL) boundaries are induced by higher thermal strain and cyclic loading. This provides insight into exploring processing windows for grain boundary engineering with additive manufacturing.

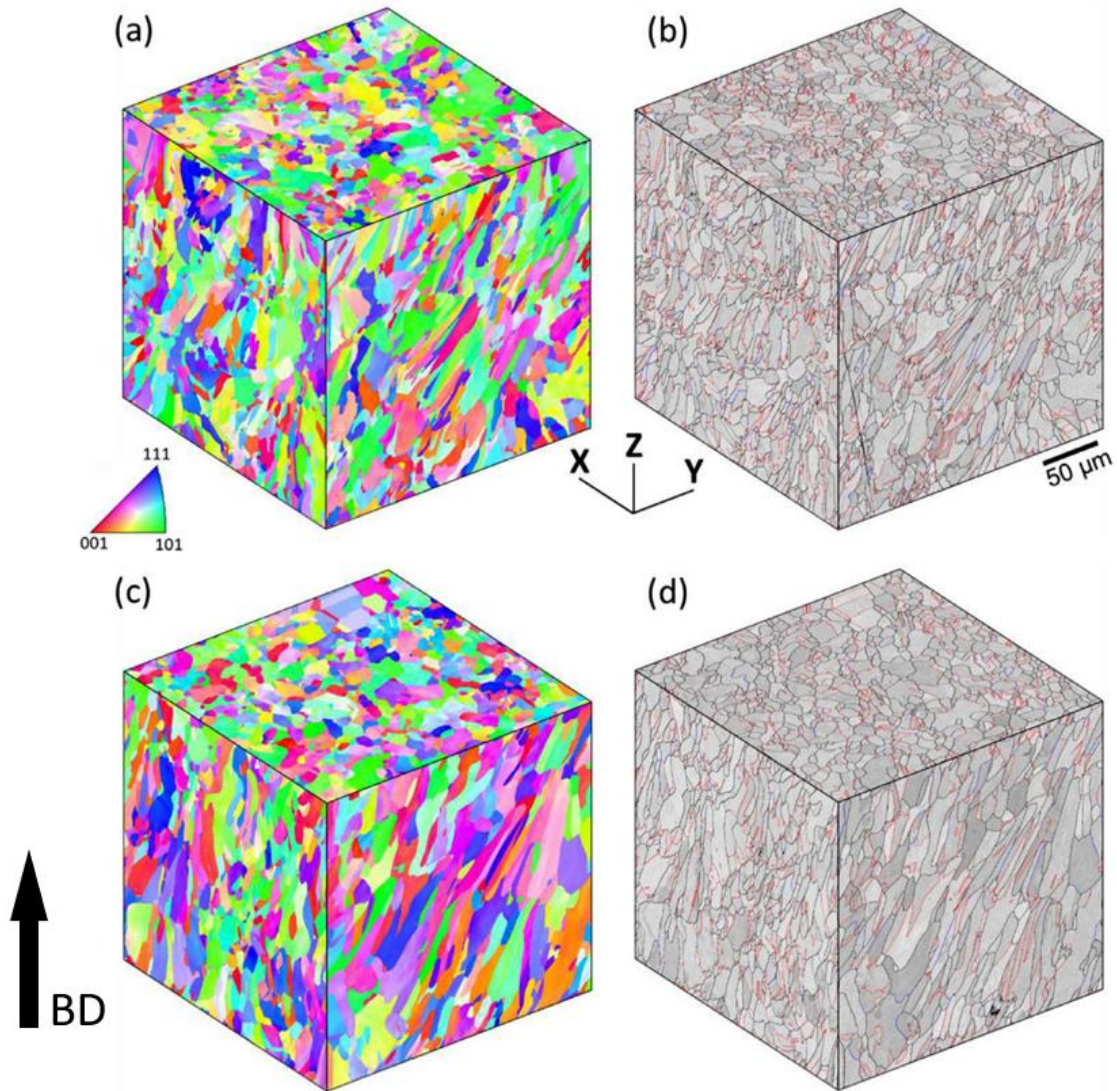


Figure 2.18: EBSD IPF showing the distribution of $\Sigma 3$ (red) and $\Sigma 9$ (blue) boundaries in (a)(b) as built and (c)(d) annealed status of 316L SS [34]. The build direction is annotated as BD.

In addition to unique interface conditions, the orientation of the grains is heavily influenced by the thermal history and processing parameters. With most AM methods, the heat flow direction is parallel to the build direction. Combined with processing parameters that does not alter grain growth periodically, large number of elongated grains with similar orientations can be obtained. [36] The directional growth observed in additively manufactured steels can be further exploited to enable texture control. Fig 2.19 shows the texture control in L-PBF built 316LSS. This unique microstructure is achieved using a layer specific scanning pattern that eliminates the influence of rotation-per-layer [37]. It is therefore important to highlight that the texture control is strongly dependent on the precise control of thermal history and solidification front. Ordinary

processing methods that involve periodic layer rotations will interfere with the continuous grain growth and result in common AM microstructures.

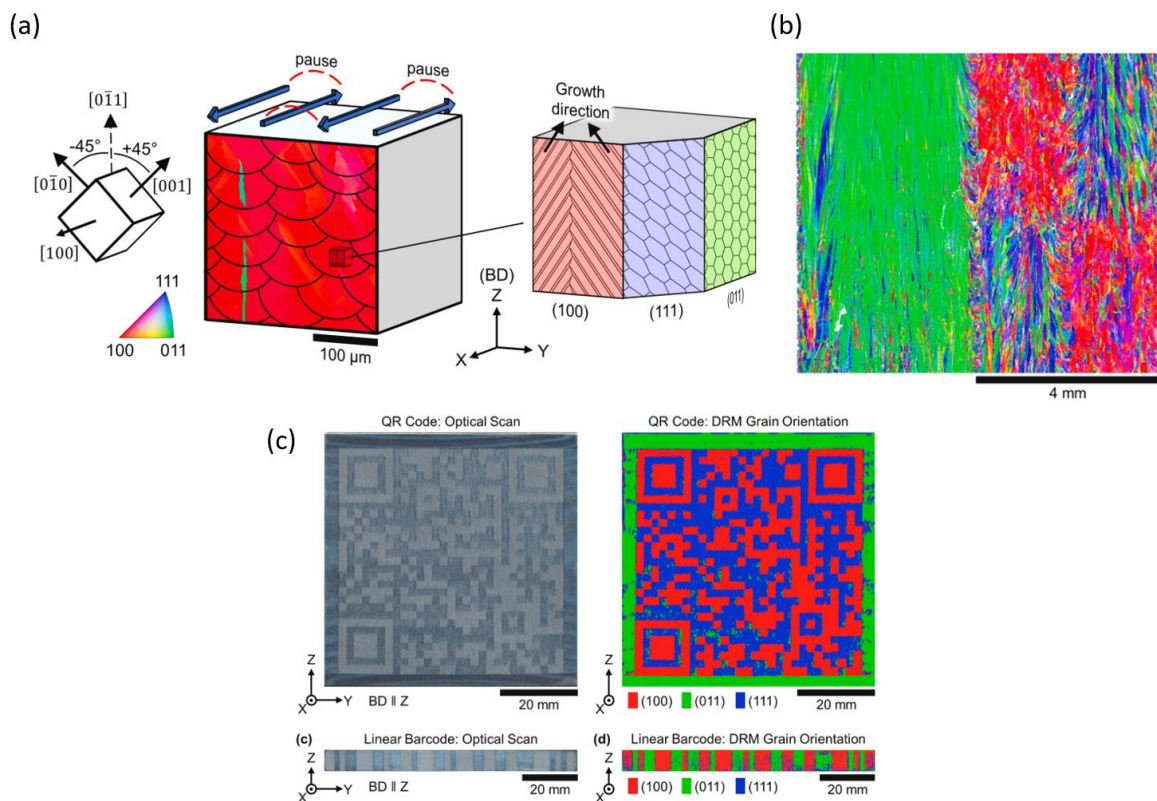


Figure 2.19: (a) Crystal orientation and supposed melt-pool morphology of additively manufactured 316LSS under texture control. (b) EBSD IPF map of texture controlled 316LSS. Large blocks of grains are successfully grown in the same orientation. (c) Optical and directional reflectance microscopy micrograph of etched surface showing a QR code [37].

Here, one can summarise that the superior yield strength observed in additively manufactured steels mainly attributes to the dislocation cell structure. The interface characteristics can also be heavily influenced by processing parameters. For transforming materials, these interfaces will also result in interesting orientation of transformation products. The following section will review the progress in transforming steels in additive manufacturing.

2.4.2. M300 maraging steel

Maraging (martensite ageing) steel is a class of martensitic steel that gains strength and ductility from precipitation of intermetallic compounds through complex thermal mechanical heat treatments. Conventional maraging steels containing 10-20 wt.% nickel tend to have an ultra-high ultimate tensile stress (UTS) of ~1900 MPa with ductility of 5-10% in aged status [38]. A very low level of carbon (usually less than 0.03 wt%) is often found in this class of

steels to avoid formation of carbides, which might lead to further embrittlement. Due to the alloy chemistry, the martensite start temperature (M_s) is around 200°C and only a small proportion of austenite is obtained in the as-built status. Current studies in maraging steels focus on obtaining superior mechanical performances with increased cost-effectiveness. By minimising the lattice mismatch between the martensite matrix and the B2-structured intermetallic ageing product, a superior combination of mechanical properties was obtained in a conventionally manufactured Co-free maraging steel [39]. Certain grades of maraging steels were widely applied in military engineering. The use of L-PBF can effectively reduce production-related waste and fabricate objects of complex shape without forming-induced cracks. The most noticeable maraging steel candidate in L-PBF is 18Ni-300 grade maraging steel, commonly regarded as M300 or MS-1. Table 2-2 outlines the compositional difference between conventional and state-of-the-art maraging steels.

Table 2-2: Composition and mechanical properties of M300 and emerging maraging steels

Steel	Composition (wt.%)	Ageing plan	Ultimate Tensile Strength (MPa)	Elongation to failure (%)
M300 [40]	Fe-18Ni-8.5Co-4.85Mo-0.75Ti	6hrs at 500°C	1806	5.5
NiAl precipitates [41]	Fe-18Ni-3Al-4Mo-0.8Nb-0.08C-0.01B	3hrs at 500°C	2197	8.2
NiAl & Lava Phase precipitates [42]	Fe-9.9Cr-8.02Co-6.99Ni-1.8Al-2.75Mo-2.43W	5hrs at 540°C	1868	8.1

Additively manufactured M300 maraging steel exhibits a dual phase microstructure, with martensite being the dominant phase. As shown in Fig 2.20, sub-micron dislocation cell structure can be clearly observed in martensite grains after etching [43].

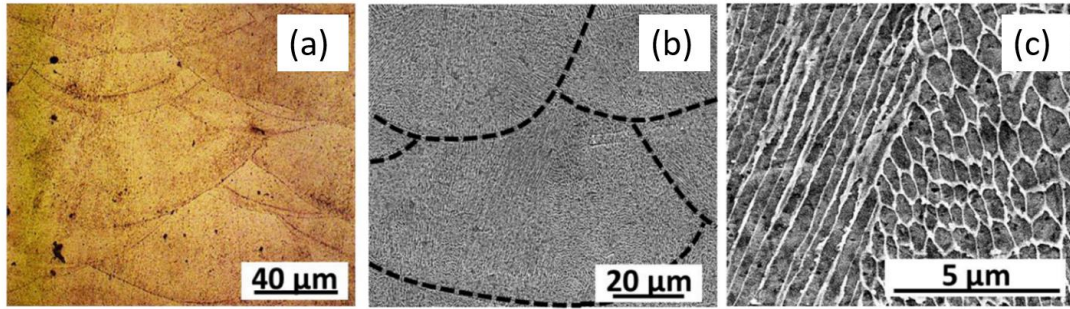


Figure 2.20: (a) 2% nitric acid etched optical micrograph of as-built M300 maraging steel. (b) SEM micrograph showing the melt pool boundaries. (c) Close up SEM micrograph showing dislocation cells [43].

Shamsdini et al. studied the effect of layer thickness on the microstructure and mechanical properties of MS1 maraging steel (same composition as M300 grade). The results suggest that thicker layer thickness leads to formation of higher density of core-shell structured Al-O-Ti-N oxides, the EDS map of as-built MS1 with a layer thickness of 40μm is shown in Fig 2.21 [44]. This shows that processing parameters can directly influence the microstructure via cooling rate control. In addition to process-induced nucleation of intermetallic compounds, boundary segregation of Ni Mo and Ti can also be observed. It is also proposed by Shamsdini et al. that Ti and Mo are more likely to be found in cell boundaries due to their relatively low distribution coefficient and high diffusional coefficient [45]. Their work on additive manufactured maraging steels demonstrates that AM segregation profile is mostly related to the strong solute rejection at solid/liquid interface, which then develops into trapping of certain solute elements based on their diffusional characteristics.

To achieve the abovementioned ultra-high strength, aging heat treatment has become a major interest in the research of M300 maraging steel. Mooney et al. studied the effect of heat treatment on the mechanical performance of additively manufactured M300 maraging steel, as demonstrated in Fig 2.22 [46]. Due to the anisotropy in the as-built M300, optimal ageing treatment results in a UTS of 1700 MPa and an elongation to failure of 10%. The highest ultimate tensile strength can be achieved with ageing at 460°C for 6 hours though a significant reduction in ductility can be observed. The best ductility is achieved when the sample is aged at 600°C for 6 hours, as the elongation to failure exceeded 15%.

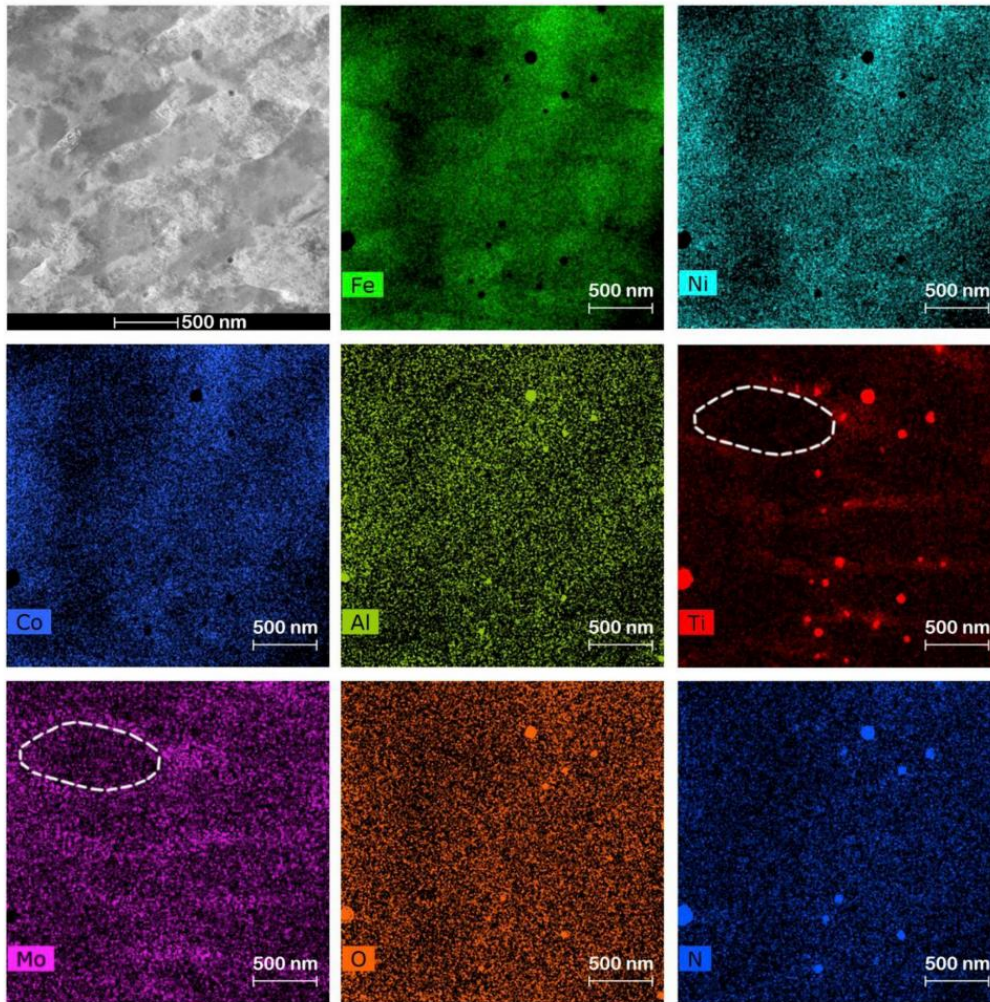


Figure 2.21: STEM EDS segregation maps of additively manufactured MS1 maraging steel. By comparing with the bright field STEM image at the top left corner, strong Mo cell-boundary segregation can be observed in bottom left map of Molybdenum. High density of Ti-Al nanoparticles is also observed in corresponding segregation maps [44]. The outline of a cell is circled in white.

The results also demonstrate the strong connection between mechanical properties and build direction. While similar performances were obtained in horizontal and vertically built tensile specimens, inclined samples displayed less desirable ductility values in both as-built and aged conditions. The systematic reduction of ductility in aged sample also indicate that ageing heat treatment cannot entirely eliminate the influence of as-built anisotropy.

Other studies have also reported similar mechanical performance results where the ductility tends to be compromised when peak tensile strength is achieved [47][48]. This is mainly attributed to the dislocation cells which do not dissolve at intermediate ageing temperature. With short ageing time and insufficient recovery of austenite, the martensitic matrix is hardened with intermetallic compounds and an overall low strain accommodation capability is

created. Fig 2.23 shows typical microstructure of aged M300, partial dissolution of cell boundaries and reversion of austenite can be seen as ageing length increases.

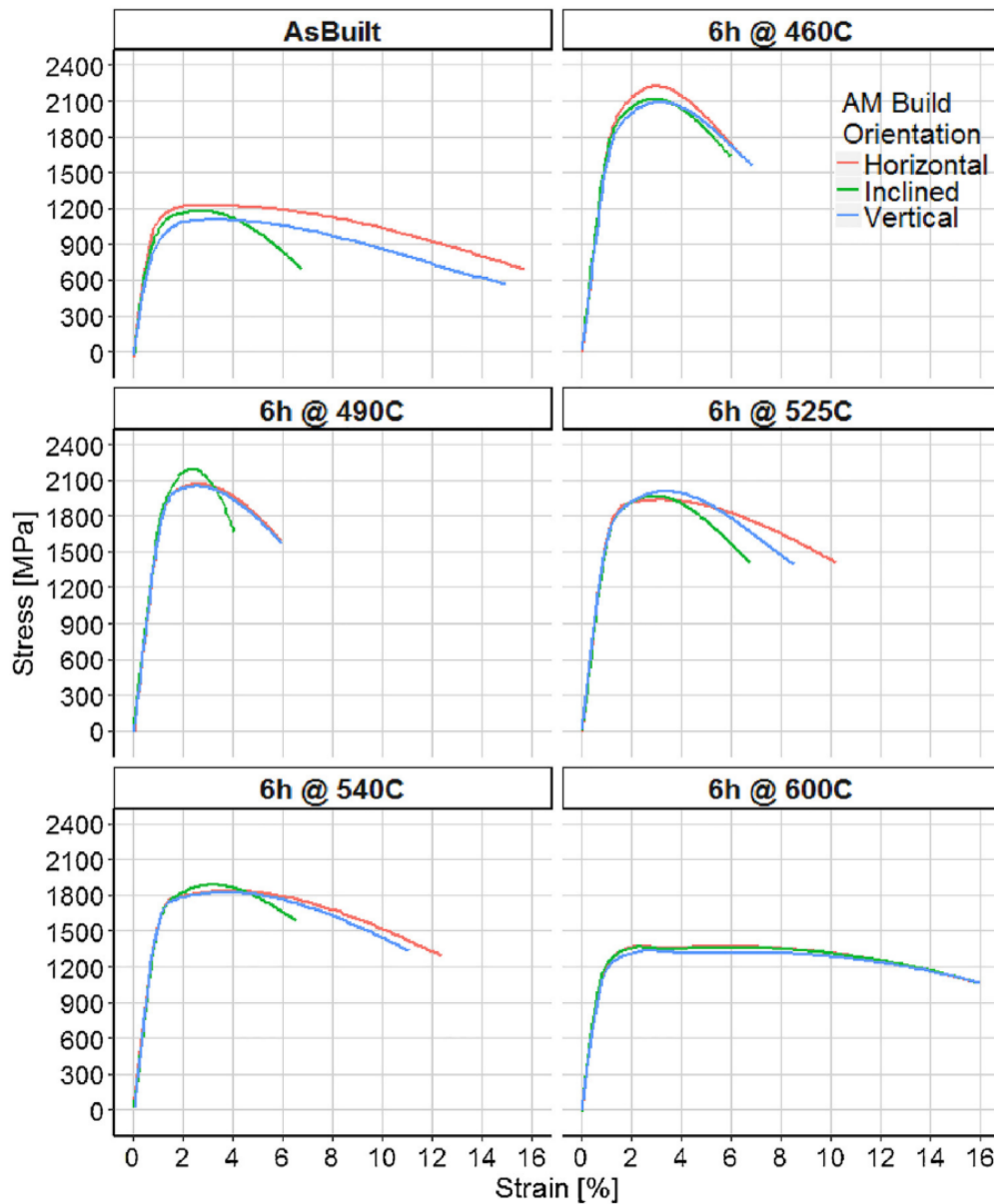


Figure 2.22: Engineering stress-strain curves of as-built and heat treated M300 samples. A trade-off between peak strength and elongation to failure can be clearly seen between as-built and aged samples. Inclined samples (coloured in green) exhibit overall inferior mechanical performance [46].

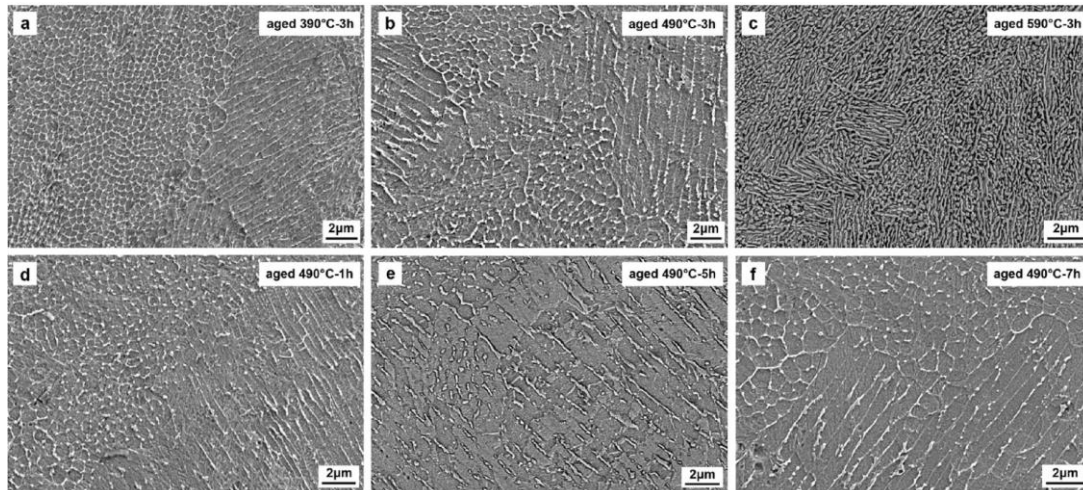


Figure 2.23: Secondary electron micrographs showing the partially dissolved dislocation network in M300 after substantial ageing heat treatment [49].

In addition to the mechanical properties of additively manufactured M300, recently a series of studies have critically analysed the phase constitution of additively manufactured 17-4PH and M300. It was discovered that while X-ray diffraction spectrums reveal a dual phase microstructure, magnetic testing suggested that as-built 17-4PH steel appeared to be fully austenitic. Freeman et al. suggested that the above mentioned dislocation cell structure once again acted as grain refinement and suppressed the athermal martensitic transformation which should have occurred well above room temperature [50]. Furthermore, no further transformation took place after as-built samples were submerged in liquid nitrogen, indicating that the martensitic transformation was indeed fully suppressed by the cell structure [51].

In summary, the unique dislocation cell structure has enabled significant yield strength increments in additively manufactured steels. While the deformation mechanism of metastable stainless steels favours this hierarchical microstructure, martensitic steels have encountered trade-off in performances due to the high stability of these dislocation cells. Additionally, athermal martensitic transformation can be suppressed by this unique microstructure and high-volume fraction of metastable austenite can be obtained in steels that are supposed to be mostly martensitic. Now the attention will move to some of the state-of-the-art steels that were introduced in the last few years.

2.5. Advanced high manganese steel

High manganese steels received intensive research attention in the last two decades. In comparison to legacy Hadfield steel which contains 13 wt.% manganese, modern high manganese steel triumphs in easy in production and superior ductility. Initial studies focused

on compositions with higher percentage of manganese and lower content of carbon [52]. With the advancements in characterisation techniques of high manganese steels, it was discovered that the deformation mechanism of high manganese steels can be tailored with alloying elements. Addition of lightweight elements such as aluminium and silicon resulted in a reduced density, making these steels suitable for body-in-white application in today's automotive industry. Table 2-3 shows common chemical compositions of high manganese steels that have yielded significant research output.

Table 2-3: Compositions and deformation mechanisms of high manganese steels

Author	Composition (wt.%)	Deformation Mechanism
Grässel et al. [52]	Fe-20Mn-3Si-3Al-0.02C	TWIP & TRIP
Welsch et al. [53]	Fe-30.4Mn-8Al-1.2C	TWIP & Microband
Rahman et al. [54]	Fe-15Mn-2Si-2Al-0.7C	TWIP
Gao et al. [55]	Fe-22Mn-4Cu-0.6C	TWIP
Xie et al. [56]	Fe-17.74Mn-2.96Si-0.44Al-0.57C	TWIP & TRIP

Two unique mechanisms can be activated by achieving certain stacking fault energies (SFE): transformation induced plasticity and twinning induced plasticity. The role of stacking fault energies on the deformation mechanism of steels is shown in Fig 2.24.

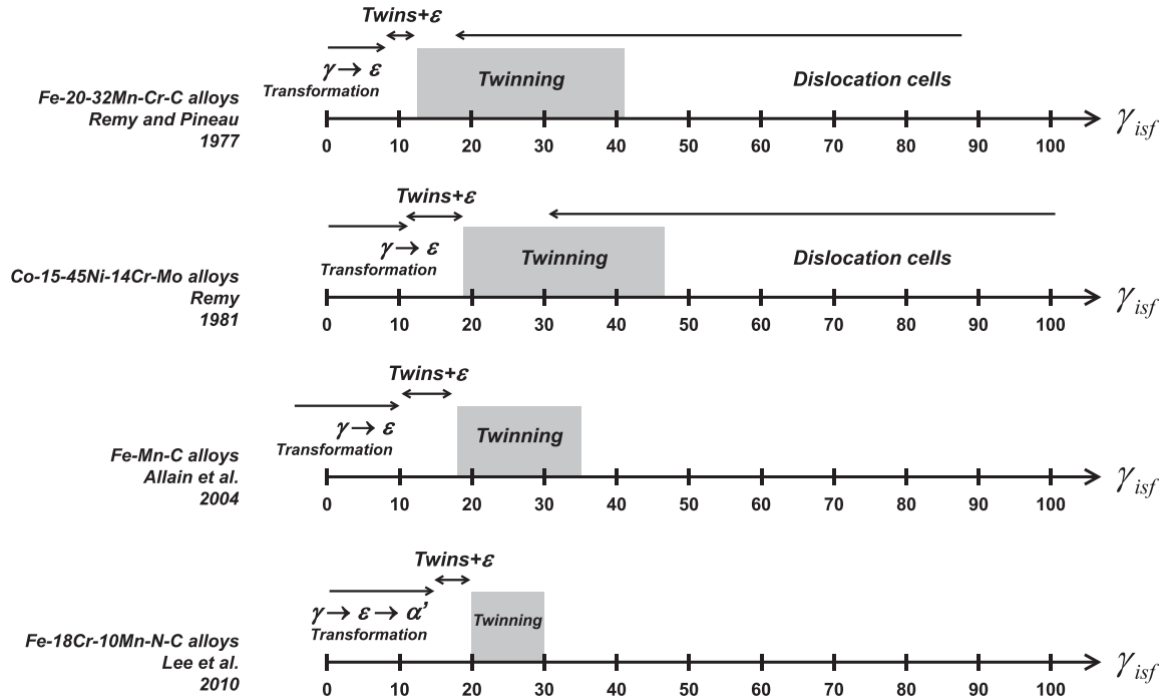


Figure 2.24: A series of studies showing how changing the chemistry can alter the deformation mechanism [57].

The effect of alloy elements on the SFE has been well discussed by De Cooman et al. [57]. In most high manganese TWIP or TRIP steels, the stabilisation of austenite at room temperature is achieved by manganese and carbon. Other elements such as aluminium and silicon plays subtle roles in controlling the intrinsic stacking fault energy (γ_{isf}), which governs the activation of deformation mechanisms. For TWIP steel compositions that contain 16-33 at.% manganese, simulation and experimental work shows that an 18 mJ/m² increase in γ_{isf} per wt.% manganese addition can be expected. On the other hand, the positioning of carbon is highly important as its distance from the stacking fault plane strongly affects its influence on the γ_{isf} of the TWIP steel [57]. Alloying with aluminium increases the stacking fault energy and suppresses the TRIP effect. Simulation and experimental works show that 8-10 mJ/m² can be induced by adding 1 wt.% of aluminium [58][59]. In addition, it was also discovered that aluminium is effective in reducing the mobility of hydrogen in high manganese steels [60][61]. Silicon is another element that is often added to high manganese steels. Apart from good solid-solution strengthening effect, the role of silicon on the intrinsic stacking fault energy is debatable as studies have found silicon to contribute to both increase and decreasing γ_{isf} . While TWIP steels are most likely to achieve a superior combination of strength and ductility, a substantial amount of manganese (around 20 wt.%) is often needed to achieve sufficient

stabilisation of the austenite phase. In comparison, TRIP steels have higher compositional freedom and can be alloyed to achieve other strengthening effects, such as the martensitic ageing effect discussed above. This has been demonstrated by a recently developed rapid alloy prototyping system reported by Springer and Raabe [62]. To summarise, a common TWIP steel composition comprises a substantial addition of manganese and a balanced amount of aluminium, silicon and carbon. While past studies could give a good indication to whether a new composition would yield a fully austenitic microstructure at room temperature, it is worthwhile noting that the abovementioned individual effect of alloying elements are subject to the compositions utilised in those studies and may not be entirely applicable to other steel compositions.

One of the key challenges in the development of TWIP steels is the low yield strength. Previously the issue is mainly circumvented by extreme plastic deformation and annealing which results in very fine grains. In Fig 2.25, it is obvious that coarse grained TWIP steel exhibit a low yield strength around 400 MPa. By conducting plastic deformation and 1~2 minute rapid annealing, the yield strength was successfully increased to 600MPa when the grain size is below 5 μ m, only at a cost of 10-15% elongation to failure [54]. However, such a short annealing time is hard to achieve with realistic sizes of steel sheets.

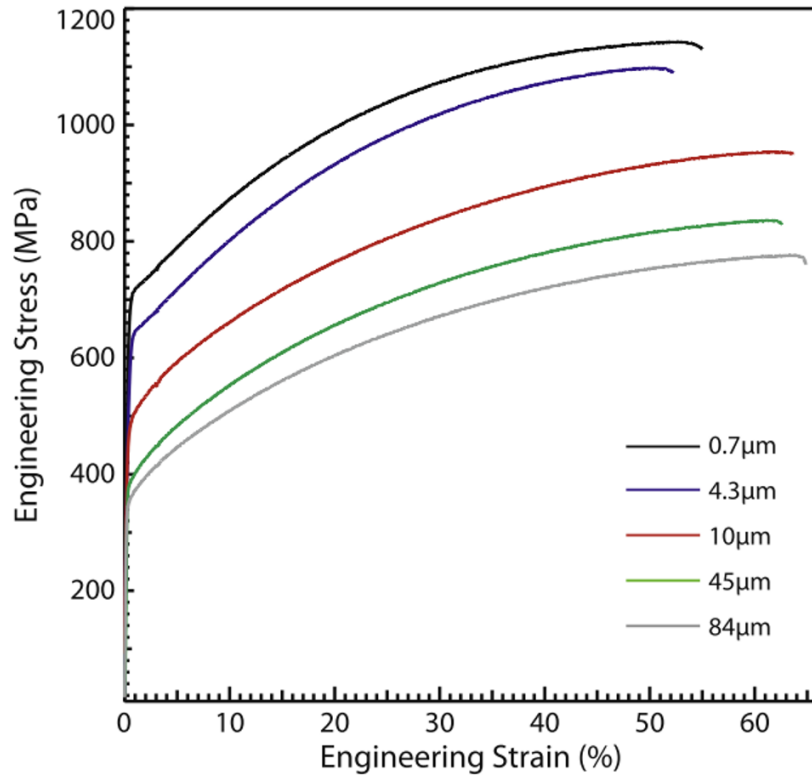


Figure 2.25: Engineering stress strain curve of TWIP steels with different grain sizes. Smaller grains lead to higher yield strength and slight reduction in plastic strain [54].

To enable fabrication of high strength TWIP steel with realistic annealing time, Gao et al. introduced a TWIP steel composition with copper addition where the nanoparticles provide extra pinning and strengthening effect [55]. As shown in Fig 2.26, the addition of Cu contributed to grain refinement during the annealing process.

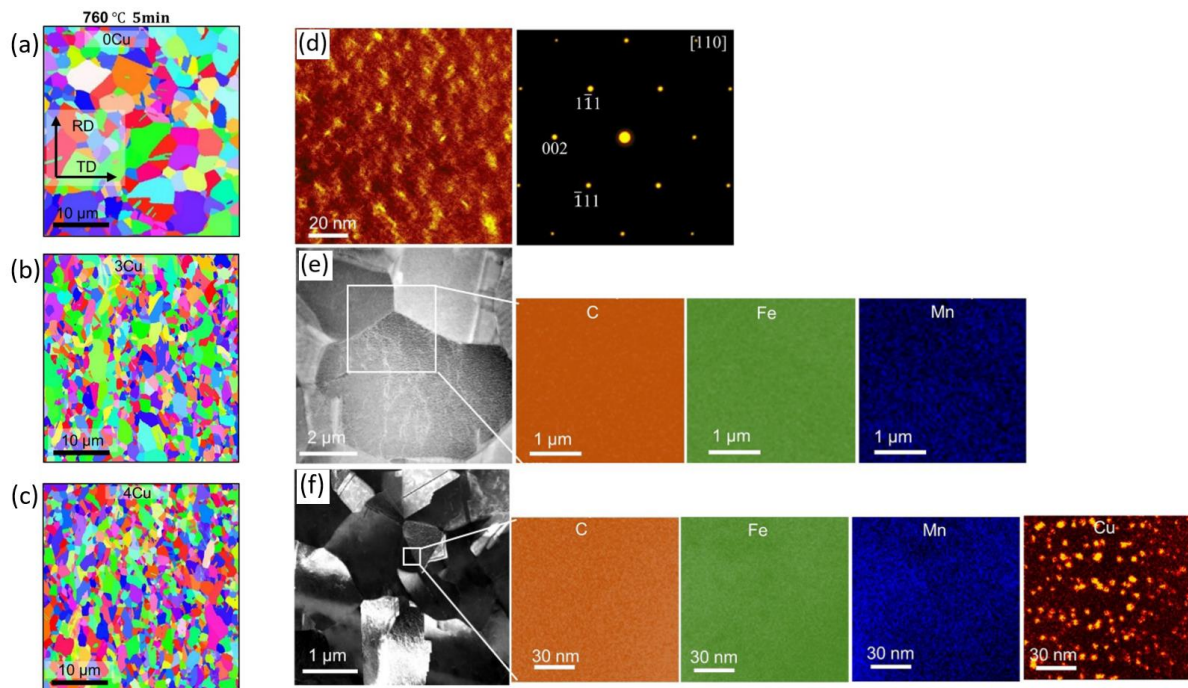


Figure 2.26: Grain refinement results of (a)Fe-22Mn-0.6C (b)Fe-22Mn-0.6C-3Cu and (c) Fe-22Mn-0.6C-4Cu. It is clearly displayed that increasing addition of Cu leads to finer grain size. STEM EDS map in (d) shows the distribution of Cu-nanoparticles in the TWIP steel with 4 wt.% of Cu addition. Diffraction pattern on the right indicates a single phase microstructure in the [110] FCC zone axis. (e) and (f) shows grain size and element segregation of Fe-22Mn-0.6C and Fe-22Mn-0.6C-3Cu, respectively. No grain boundary segregation can be seen, and a high population of Cu-nanoparticles are clearly visible in the 3Cu composition [55].

When a substantial amount of Cu is added, a high density of Cu-nano particles is also nucleated as the result of the annealing process. When strained, the increased deformation twinning density resulted in shearing of these Cu- nanoparticles and further refines the twinning-dominated microstructure. Fig 2.27 shows the mechanical properties and deformed microstructure of this novel TWIP steel. A combination of 1200 MPa ultimate tensile strength and above 55% elongation of failure is comparable to that of the ultra-fine grained conventional TWIP steel. This study shows that with careful engineering of chemical composition, the desired strength and ductility combination of high manganese steels can still be achieved when using more realistic manufacturing procedures.

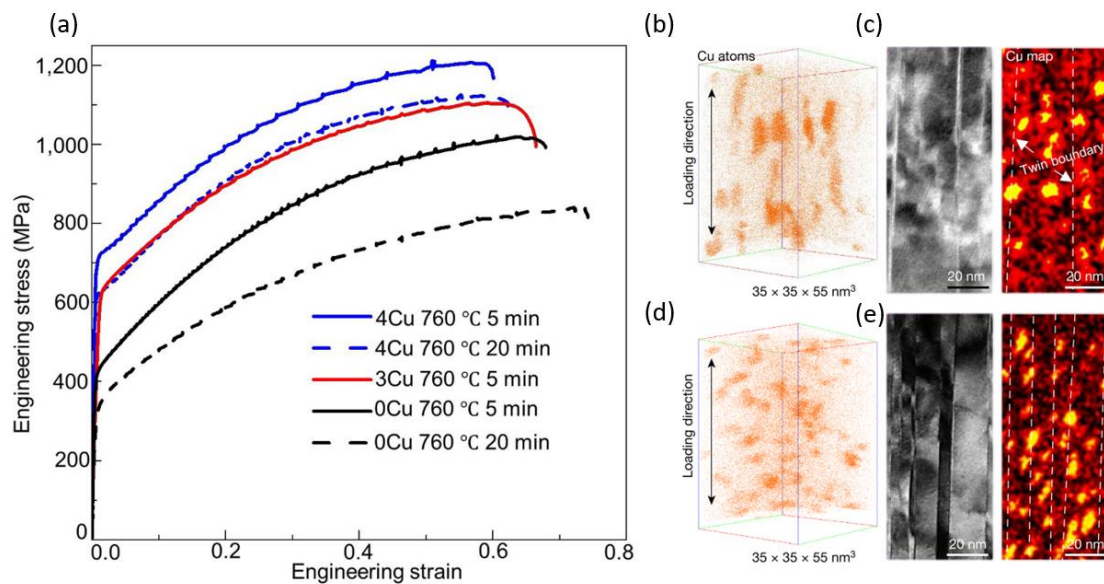


Figure 2.27: (a) Engineering stress-strain curves of Fe-22Mn-0.6C-xCu TWIP steels. The highest strength is achieved in the 4Cu composition after 5min annealing at 760°C. (b) and (d) are atomic probe tomography reconstruction of the distribution of Cu-nanoparticles at 15% and 45% strain, respectively. Detailed shearing of nanoparticles is shown in (c) and (e). As the darkfield images on the left show an increase in twin density at higher strain, nanoparticles are sheared by the formation of twins and further refine the microstructure. This process is confirmed by the STEM EDS elemental segregation maps of Cu on the right [55].

In addition to twinning only steels, TWIP steels containing lower fraction of manganese can also undergo deformation induced martensitic transformation. Fig 2.28 shows the electron backscattered diffraction (EBSD) phase map of Fe-16Mn-0.3C steel at different strain levels [63]. As plastic strain increases, the γ - ϵ - α' phase transformation process takes place in areas with lower content of manganese. This shows yet another major weakness of high manganese steel, where different deformation mechanisms may activate in regions with strong elemental partitioning. The non-equilibrium segregation of manganese is a well-known phenomenon in medium-high manganese steels. While it has little influence in TWIP only steels, the banding of manganese can heavily affect the austenite stability in medium manganese TRIP steels [64].

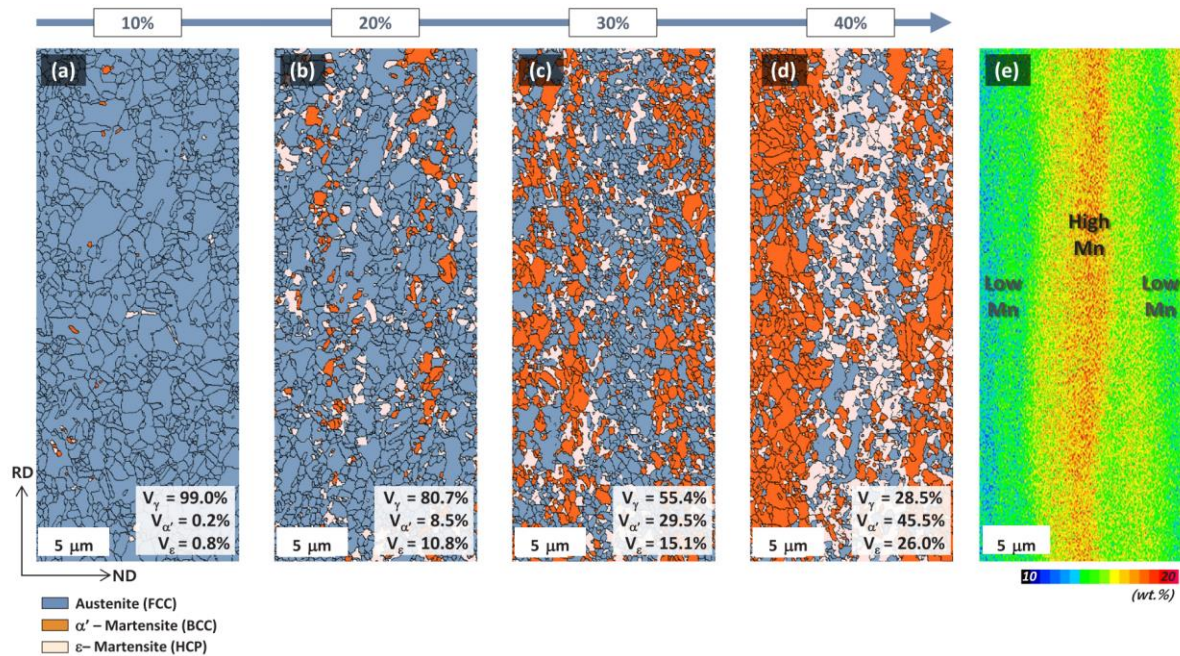


Figure 2.28: EBSD phase maps of Fe-16Mn-0.3C TRIP steel at different levels of strain. Significant transformation starts to occur after 20% plastic strain. The middle section of the sample shows a smaller magnitude of transformation due to being enriched in manganese [63].

To sum up, owing to their unique deformation mechanisms, TWIP and TRIP steels have achieved new levels in combinations of strength and ductility. However, the industrial application of this class of steels is difficult due to the flash heat treatment associated with the grain refinement process [55][65]. So far, it is established that state-of-the-art TWIP and TRIP steels have superior performances over market-available legacy steels that are applied to metal additive manufacturing. The hierarchical microstructure associated with L-PBF built steels happens to favour the grain refinement needed of TWIP steel. Based on the review of defects that are commonly found in AM, further reviews are conducted into alloys that are susceptible to AM conditions.

2.6. Low transformation temperature electrodes(LTTE)

Alloys are usually designed for applications and appropriate processing methods are adopted to achieve desired target properties. However, a very special category of alloys is designed for the processing itself. The joining of metal components often requires a third-party consumable alloy to be melted and re-solidify at the area of joining. These alloys are referred to as weld-fillers. The design goals of these fillers are more sophisticated as they cannot compromise the strength of the joint, nor cause further distortion to the final shape. The alloy composition of

these fillers also must be carefully chosen, as the chemistry of the alloy mixture decides the final phase constitution in the joint.

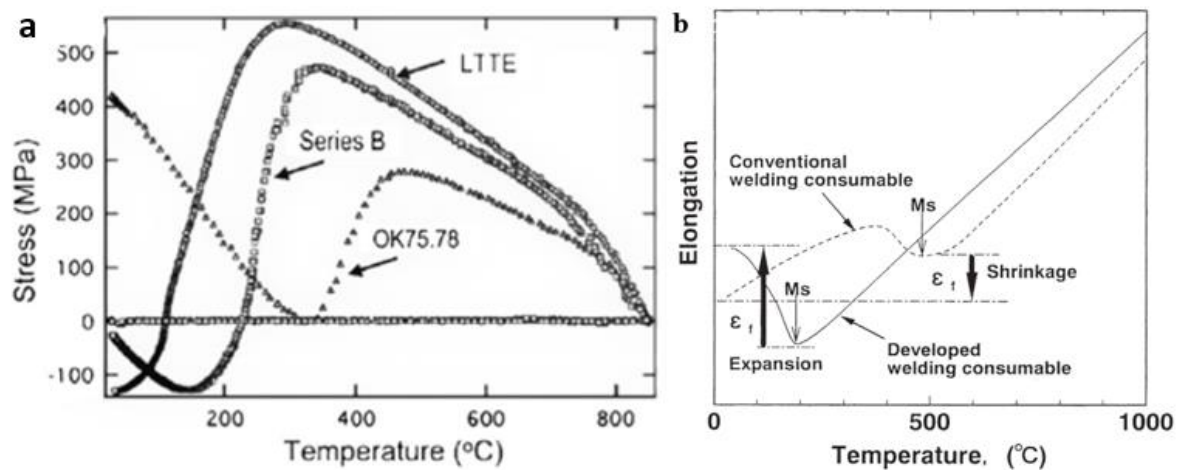


Figure 2.29: a: Comparison of welding electrodes with different M_s and its influence on the residual stress [66]. b: Schematic diagram showing the improvement made by reducing M_s [67].

Pursuing a better weld joint fatigue performance, Ohta reported a low transformation temperature electrode (LTTE) that displays a superior fatigue life [67][68]. The effect of phase transformation on the residual stress can be demonstrated by the Satoh test. As illustrated by Fig 2.29, linear increase in residual stress can be observed with fully austenitic stainless steel. A reduction of residual stress was observed on the steels with martensitic transformation. However, when the transformation depletes, an increase in the residual stress is once again observed. Therefore, by controlling the martensitic starting temperature (M_s), the period between transformation finish and fully cooled can be effectively minimised.

Laser based additive manufacturing suffers from shape distortion due to residual stress which can ramp up above 800MPa [69]. The concept of LTTE can be then considered and one can propose that alloys with low transformation temperature are likely to perform well in AM, due to the similarity in processing and solidification conditions. Many steels that are currently utilised in AM shares some of the main characteristics of LTTEs, namely a low martensitic transformation temperature. Commercial alloys such as 18Ni-300 (M300) and 17-4PH steel both have martensite starting temperature in the range of 100-200°C, which makes them suitable candidates for stress-relief studies [51][70].

To sum up, LTTEs have shown capabilities in minimising thermally induced residual stress. Reduction in M_s has led to the formation of compressive residual stress, which has a positive

impact on the fatigue life. Alloys such as M300 and 17-4PH are suitable candidates for investigating whether LTTE mechanisms can be applied to the L-PBF environment.

2.7. Summary

Through the literature investigation, it is obvious that powder based metal additive manufacturing is a disruptive technology that enables manufacturing of high strength parts with on-demand shapes. The significant enhancement in the tensile strength of additively manufactured steels mainly originates from the signature as-built microstructure which is a product of the steep thermal gradient: a unique dislocation network formed by low angle cell boundaries, high angle grain boundaries and nano-precipitates. Depending on the processing parameters, elemental segregation can also be found in cell boundaries and further pin the movement of dislocations during plastic deformation. Although these low angle grain boundaries are extremely effective in improving yield strength, the ultimate tensile strength of additively manufactured legacy steels saw limited increment due to the lack of work-hardening. In comparison, twinning induced plasticity steels, a class of high manganese steel that achieves high ultimate tensile strength via deformation twinning, is struggling to find realistic and practical pathway to higher yield strength. The unique microstructure associated with the AM mechanism is a good fit to the challenge of TWIP steels, therefore the main aim of this study: application of high manganese steels in laser additive manufacturing.

In addition to reaching new heights in materials performance, the formation of defects in metal additive manufacturing was also reviewed. The steep thermal gradient can result in unwanted thermally induced transformation and residual stresses. In particular, residual stresses can lead to shape distortion and deterioration in mechanical performances. The latest progress in welding metallurgy shows that a class of low transformation temperature filler steels possess self stress-relief capability through athermal martensitic transformation around 200°C. A side quest is then set off to identify the role of martensitic transformation in additive manufacturing and how it influences the final residual stress present on the build part with 18Ni-300 maraging steel. Detailed experimental procedures will be described in the following chapter.

3. Methods

3.1. Additive manufacturing with metal powder

3.1.1. Powder preparation

Metal powders are kept in Ar-charged containers after production. After each build, used powder was then sieved with adequate test sieves and residues above 45µm will be discarded. New and unused powder was also inspected in SEM before use as a quality check. Table 3-1 below shows the exact chemical composition of steel powders used in the present study.

Table 3-1: Chemical composition of steels used in this study

Steel	Composition in wt. %
High manganese TWIP steel	Fe-18.3Mn-2Al-0.5Si-0.3C
M300 maraging steel	Fe-18Ni-8.5Co-4.85Mo-0.75Ti
316L stainless steel	Fe-17Cr-12Ni-2.5Mo-2Mn-1Si

3.1.2. Build file design

For the DoE experiments, Autodesk Netfabb software was utilised to generate build files by combining 3D geometries with processing parameters.

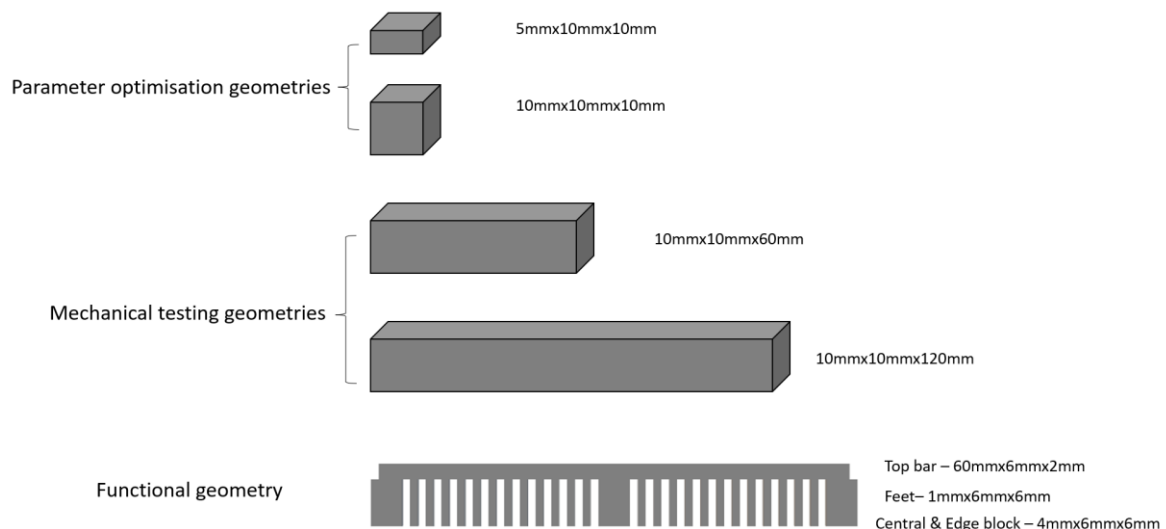


Figure 3.1: Geometries utilised in this study. Cuboids were mostly used for design of experiment purpose and can be further cut-off for microscopy investigations. Tensile bars were extracted from bar structures. The presence of as-built residual stress was revealed by the cantilever structure.

As illustrated in Fig 3.1, a 10mm³ cube structure is used for parameter optimisation experiment and as-built microstructure characterisation. For mechanical properties characterisation, tensile bars were electrical discharge machined (EDM) sectioned from rectangular bars. Detailed tensile specimen drawings are shown in Appendix Fig 1 and Appendix Fig 2. In addition, the cantilever structure mentioned in the literature review has been adopted to display the process induced residual stress in additively manufactured steels.

3.1.3. Machine setup

A schematic of the Aconity L-PBF machines is displayed below in Fig 3.2 and the heating element installed in Aconity Lab is shown in Fig 3.3. Rubber wiper blades are used, and argon is the main re-circulation gas. The machine is cleaned and checked before loading the powder. The first layer is manually dosed to ensure a good stitching between the first layer and the substrate. Before the printing process begins, the chamber is purged below 400 ppm of oxygen and the oxygen content will eventually drop to 0 ppm. Argon is constantly flowing in the chamber from right to left as indicated in the schematic diagram.

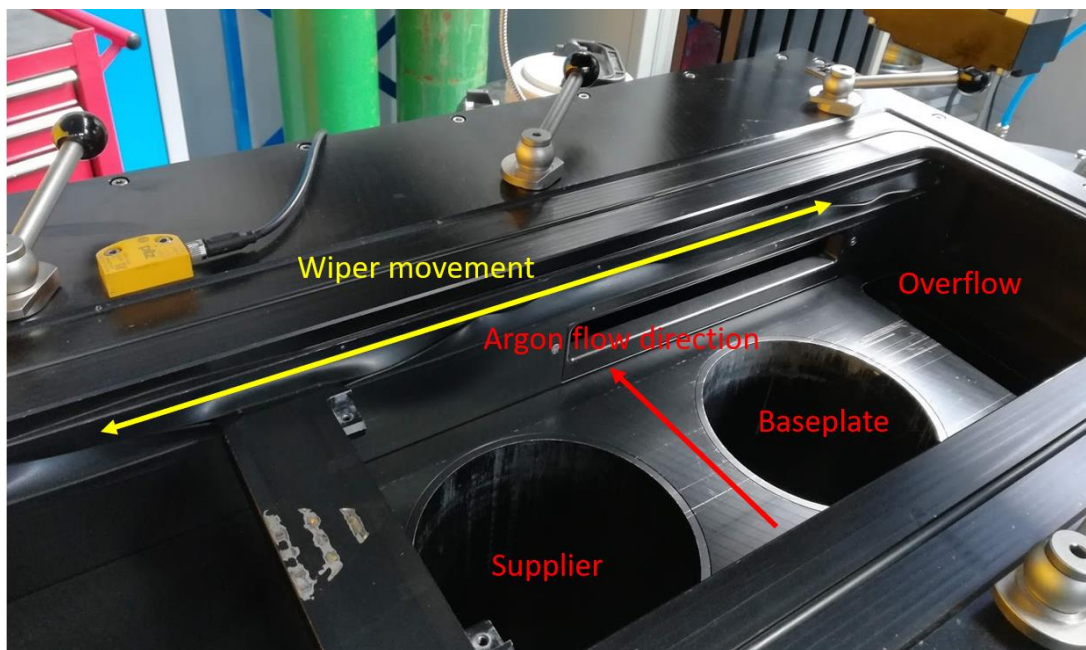


Figure 3.2: Processing chamber of the Aconity Mini. The supplier sits in front of the baseplate column. Each layer the wiper blade brings new powder from raised supplier platform to the lowered baseplate platform. Excess powders are swept to the overflow.

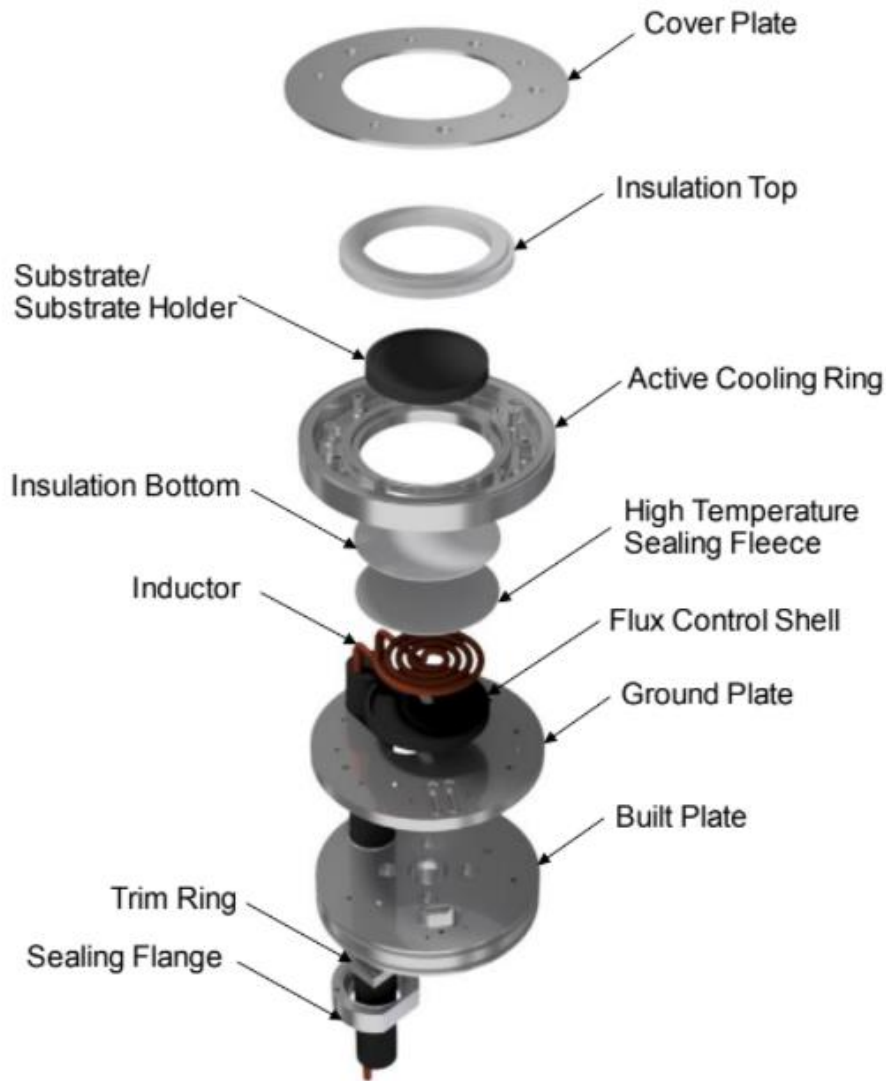


Figure 3.3: Inductive heating element installed in Aconity Lab. The baseplate can be kept at a constant temperature during the build and slowly cooled back down to room temperature after the build.

For heated bed builds, the substrate is heated to a temperature of 700°C which is recorded by a thermocouple sitting beneath the substrate. Due to convection from the shielding gas and possible conduction with other components in the chamber, readings from the top of the heated substrate seems to be lower than the designated temperature, as shown in Fig 3.4. As the ambient temperature is artificially increased, processing parameters are adjusted accordingly using melt-pool shape tracing technique. 2D plots of AM melt-pools can be created using a MATLAB script introduced by Felicity Freeman [71]. The script itself is created based on Eagar’s interpretation of a continuous gaussian laser beam in welding conditions [72]. After applying corresponding thermal properties of the alloy of interest, length of both the melt-pool and heat-affected zone can be calculated and plotted. A sensitivity test of the script with regards

to step size is shown in Appendix Fig 8. The script in this study is primarily used for calibrating processing parameter for the heated bed condition and generating melt pool length for estimating the thermal stress related to different materials. The effect of escalated ambient temperature on the length of the melt-pool is shown in Fig 3.5.

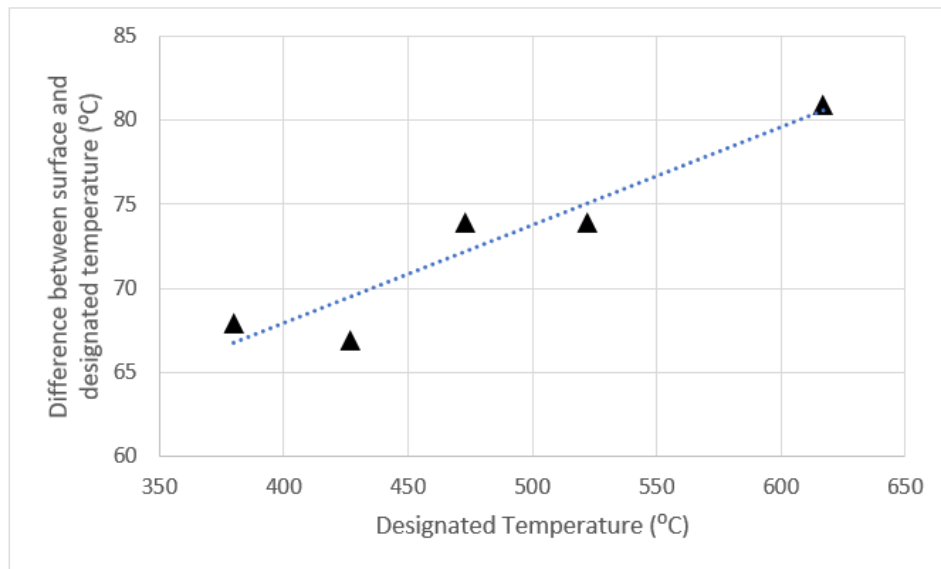
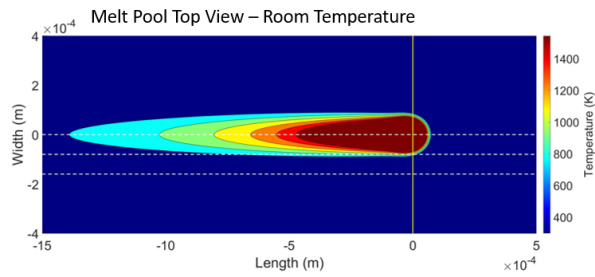
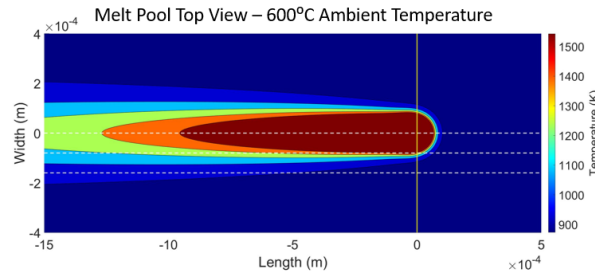


Figure 3.4: Thermocouple readings from top surface of the heated substrate and designated temperature in the heating element showing a steady increase in heat loss at higher operating temperature.

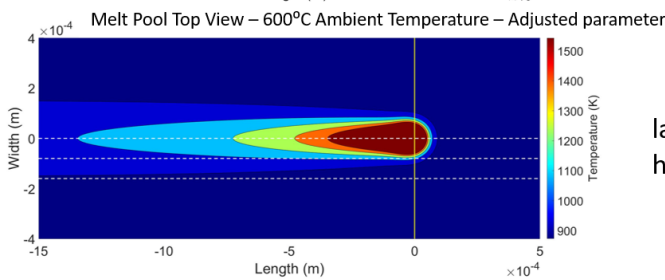
As the ambient temperature increased from 25 to 600, the predicted length of the melt-pool in the horizontal direction has significantly increased as the lowest temperature contour extend out of the figure. This means that the melt-pool is now elongated and overheat can occur in small geometries as the laser returns to the starting point of a hatch faster. To resolve this issue, the melt-pool length can be corrected by reducing the energy density. In Fig 3.5, size of the overall heat-affected zone was successfully restored in the high temperature environment by reducing the laser power from 140W to 80W, as well as adjusting the laser scan speed to 1.4m/s.



laser power: 140W. laser scan speed:1.2m/s.
hatch spacing: 80 μ m



laser power: 140W. laser scan speed:1.2m/s.
hatch spacing: 80 μ m



laser power: 60W. laser scan speed:1.4m/s.
hatch spacing: 80 μ m

Figure 3.5: Melt-pool top view temperature contour plots of M300 steel processed at room temperature and heated bed environment. The laser scan power, scan speed and hatch space of each condition is presented alongside with the plot.

3.1.4. Post build inspection

After the printing process. Baseplates are removed from the chamber and inspected for visual defects. Inadequate parameters can result in visible defects such as missing layers and cavities on the side of the samples. The baseplate is then sent off for EDM cut-off and the density of as-built samples are measured with Archimedes method.

3.2. Application of high manganese TWIP steel in AM

3.2.1. Alloy selection

Based on the literature review, a high manganese TWIP steel composition is to be proposed for the present study. Since mechanical property breakthrough is not a priority in this study, the chemical composition of the proposed steel mainly focuses on achieving a fully austenitic microstructure and possible activation of both deformation mechanisms. Based on the review of weldability diagrams, a relatively lower content of carbon should be considered to reduce the crack susceptibility of the proposed steel. A manganese fraction of 18 wt.% and a carbon content of 0.3 wt.% are considered to achieve sufficient austenite stabilisation. 2 wt.% of aluminium will also be added to promote hydrogen-cracking resistance, as well as 0.5 wt.% of

silicon for solid solution strengthening. A similar composition has been introduced by Jo et al., where TRIP mechanism was activated in Fe-16Mn-0.3C composition and TWIP mechanism was more dominant in the Fe-16Mn-0.5C composition [63]. The proposed composition in the present study should favour TWIP mechanism as the 2 wt.% addition of aluminium also effectively increases intrinsic stacking fault energy.

Due to the manganese evaporation during the processing, the Mn content varies slightly throughout the research and the results from chemical analysis can be found in Table 3-2:

Table 3-2: Chemical composition of the proposed TWIP steel at different processing status.

Processing Condition	Alloy Composition (wt.%)
Design Phase	Fe-18Mn-2Al-0.5Si-0.3C
Arc Melting	Fe-16.6Mn-2Al-0.5Si-0.3C
L-PBF	Fe-17Mn-2Al-0.5Si-0.3C

To ensure a fully metastable austenitic microstructure is obtained in the as-built status, the martensite transformation start temperature is estimated with equation 3.1[73]:

$$M_s = 539 - 423C \text{ wt. \%} - 30.4 \times Mn \text{ wt. \%} - 17.7 \times Ni \text{ wt. \%} - 12.1 \times Cr \text{ wt. \%} - 7.5 \times Mo \text{ wt. \%} + 10 * Al \text{ wt. \%} \quad (3.1)$$

Using this equation, martensite start temperatures of the steels utilised in this study are estimated and listed in Table 3-3 below.

Table 3-3: Calculated martensite start temperatures of the steels studied in this project

Steels	Estimated Ms (°C)
Fe-18Mn-2Al-0.5Si-0.3 (Nominal composition)	-155.1
Fe-16.6Mn-2Al-0.5Si-0.3C (Conventionally processed)	-118.62
Fe-17Mn-2Al-0.5Si-0.3C (Additively manufactured)	-124.7
M300 maraging steel	179.465

3.2.2. Arc melting and heat treatment

To assess the mechanical properties through conventional process and welding susceptibility of Fe-Mn steel, rectangular ingots were prepared with arc melting. The raw materials were purchased from Goodfellow and Sigma Aldrich with a minimum purity of 99.9%. The alloy was then arc-melted in an Edmund Buhler MAM-1 arc-melter with water-cooled crucible and casting mould. Highly evaporative elements such as manganese are wrapped with aluminium foil or fully covered by iron pieces to avoid direct contact with the electric arc. Each sample is flipped and re-melted for at least 12 times to achieve a fully homogeneous mixture. Tensile samples were then cast into a 5x5x60 mm water-cooled copper mould. Other samples for composition analysis were in hemispherical melt spun shape.

The tensile specimen ingots were homogenised at 1100°C for 2 hours before receiving a 60% thickness reduction to a final thickness of 1.7mm in a cold-rolling mill, the samples were then recrystallised at 900°C for 3 min, all heat treatments were followed by water-quenching. This sequence is portrayed in Fig 3.6.

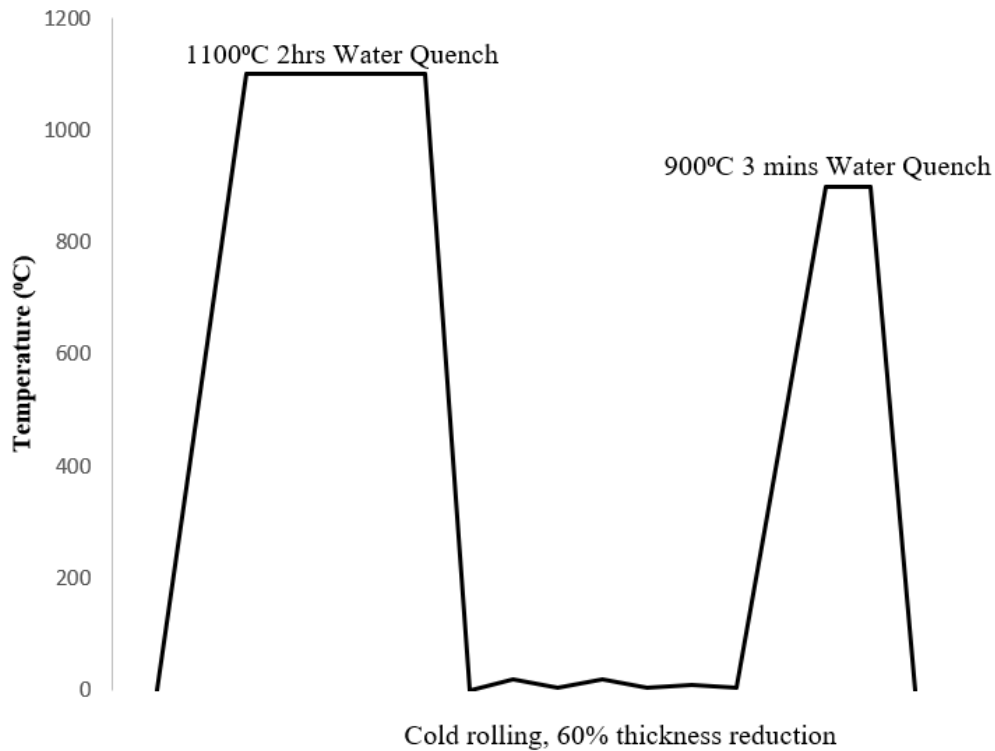


Figure 3.6: : Thermomechanical processing pathway of conventionally manufactured Fe-Mn TWIP steel. Cast steel sheet was homogenised at 1100°C for 2 hours and quenched in water. Cold rolling was then conducted to achieve 60% thickness reduction and the rolled sheet was recrystallised at 900°C for 3 minutes followed by water quenching.

The cold-rolled and recrystallised sample was then EDM and the tensile bars received slight polishing before tensile testing.

3.2.3. Weldability examination

To evaluate the printability, weld tracks were created using Aconity Mini and Aconity Lab L-PBF machines equipped with Ytterbium fibre laser units which provides a maximum power output of 190W (Mini) and 390W(Lab). The build platform height was lowered by 1-2 mm so that the top surface of samples is lined up to the laser focal plane. Samples tested received slight polishing but not to a mirror finish, to avoid direct reflection of the laser beam and possible damage to the optic system. Due to the simplicity and the short duration of the weld test, the machine was not in an inert environment.

3.2.4. Additive manufacturing of high manganese TWIP steel

TWIP steel powder is gas atomised by PSI Ltd with a size range of 15-45µm. A chemical testing result of the raw and unused powder is depicted in Appendix Fig 6. Processing parameter and build quality inspection results are shown in Fig 4.7. One-time density measurements were taken with Archimedes method.

3.2.5. Characterisation of high manganese TWIP steel

Phase analysis of all samples were carried out using a Bruker D2 Phaser with Cu K α Radiation ($\lambda=1.5406\text{\AA}$). To confirm the phase fraction in deformed microstructure, Rietveld refinement was carried out with PANalytical HighScore software. The peaks used for the calculation are shown in Appendix Fig 9. Visible light micrographs were captured in an Olympus BX51 microscope at different magnifications. EBSD analysis of strained specimens was carried out with a FEI Inspect F50 field emission scanning electron microscope equipped with an Oxford Instrument Nordlys detector operating at 20kV. The EBSD indexing step size for conventionally manufactured TWIP steel was set to $0.05\mu\text{m}$ for higher resolution. A step size of $0.1\mu\text{m}$ was selected for additively manufactured TWIP steel. High resolution characterisation was carried out on a JEOL F200 Analytical TEM equipped with Oxford Instrument silicon drift EDS detectors. The tensile properties were characterised using a Zwick/Roell Z050 at various strain rates. An optical extensometer was used to accurately measure plastic strain.

3.3. Additive manufacturing of M300 maraging steel

3.3.1. Part fabrication

M300 maraging steel powder in the size range of $15\text{-}45\mu\text{m}$ are provided by Carpenter LPW Ltd. $5\text{mm} \times 10\text{mm} \times 10\text{mm}$ cuboids for microstructure analysis were fabricated in Aconity Lab L-PBF platform with a minimum spot size of $80\mu\text{m}$. 10mm ASTM E8 tensile specimens were built at a reduced energy density. To create slow cooled thermal stress-free samples, 10mm^3 cubes and a $70\text{mm} \times 10\text{mm} \times 10\text{mm}$ tensile specimen block were built at an escalated temperature with a molybdenum induction heating element. All samples were cut off from the baseplate and further sectioned by electrical discharging machining. The processing parameters used in the study are listed below in Table 3-4.

Table 3-4: Processing parameters of this study.

	Power (W)	Scan (m/s)	Speed	Hatch (μm)	Spacing	Layer thickness(μm)
Room Temp	180	1		35		40
Heated Bed	80	1		80		40
Tensile Bars	150	1		80		40

3.3.2. Investigation of phase transformation

Dilatometry of the as-built M300 part was conducted with a Netzsch DIL402. Heating rate was set to 10°C/min from 30°C to 850°C and cooling was allowed at a rate of 5°C/min. Effect of mechanical surface preparation is determined by comparing the X-ray diffraction spectra obtained from as-built and sand-paper ground surfaces with Malvern PANalytical X'pert³. Specimen was cut from the top of a 1cm³ cube with the EDM method and the EDM surface has been used for the experiment. Diffraction peaks between 40 and 50 two theta (2θ) were obtained on the cut surface first. The sample is then taken out and the cut surface is ground with 800-1200 grit paper and sent back to the machine for the second set of scans. Since lab based XRD machines have relatively low penetration range, this process is repeated with the Feritscope for direct measurement of magnetic phase fraction.

3.3.3. Austenite reversion heat treatment

To investigate the highest possible volume fraction of austenite in the composition, cuboid samples built at room temperature were further sectioned to smaller pieces and heat treated in a vacuum tube furnace at 600°C followed by water quenching. One sample was held at 600°C for 24hrs for investigation of the integrity of dislocation cells.

3.3.4. Austenite phase fraction measurement

To evaluate the rate and volume fraction of austenite reversion, bulk martensite phase percentage is measured with a Fischer Scientific FMP30 Feritscope on all heat-treated samples. Feritscope is widely used in measuring magnetic phase fraction in steels. As a magnetic field is generated by the primary coil of the Feritscope, all magnetic phases in the testing region interacting with that field will induce a voltage on the secondary coil of the Feritscope and this voltage is proportional to the magnetic phase fraction in the specimen. Calibration is usually made with standard samples supplied by Fischer Scientific which contain different levels of ferrite phase fractions. Additional calibration can be carried out for thin samples that are less than 2mm thick.

Due to the surface roughness of AM specimens, readings were taken at the centre of samples so that the Feritscope is guaranteed to be levelled and the same interaction volume is maintained.

In addition to direct measurement, image analysis was also conducted on EBSD phase maps with ImageJ software. The phase map was set to grey scale and threshold was adjusted to colour

appropriate regions where austenite phase is present. The grey scale images used for the measurement are shown in Appendix Fig 7.

3.3.5. Microstructure characterisation of M300 maraging steel

After EDM cut-off, samples were first ground with 1200-2500 grit grinding paper for removal of deep scratches and fine polished with OP-S on Struers Tegamin-20 with minimum load setting (5N). A Gatan PECS II was used to slightly etch the grain boundary as well as the removal of narrow scratches that are not easily visible.

Initial microstructure inspection was conducted with a FEI Inspect F50 scanning electron microscope equipped with Oxford Instrument EDS and EBSD detector. The EBSD acquisition step sizes for as-built and aged M300 samples are 0.1 μ m and 0.02 μ m, respectively. Transmission electron microscopy (TEM) was carried out on a FEI Tecnai T20 operating at 200kV. Scanning transmission electron microscopy and analytical TEM was conducted with JEOL F200 operating at 200kV. Thin-foils samples were chosen from regions with low defects and ground to a thickness of 100 μ m with 80-4000 grit paper. After punched out, thin foil with a 3mm diameter were twin jet polished with a mixture of 5% perchloric acid, 35% 2-Butoxyethanol and 60% Ethanol at -35°C and immediately cleaned with Gatan PIPS II to remove residual chemical on the surface.

3.4. Cantilever cut-off

After prototyping, the feet were sectioned off from the baseplate with EDM while the central beam is still connected to the baseplate. The distortion level was then measured in the form of gap between the feet and the substrate.

3.5. Covid influenced work

Due to the Covid-19 pandemic, some of the follow-up work in each chapter was unable to proceed. Here are some of the key experiments that would provide further understanding to the scope of the study.

- To understand of effect of partial and complete dissolution of the dislocation network on the mechanical properties, as-built TWIP steel will be subject to annealing and homogenisation heat treatments.
- Hot isostatic pressing of as-built TWIP steel for removal of nano-gas pores and partial recrystallisation.
- Study of the austenite-martensite interface in additively manufactured M300. TEM thin foils will be obtained from etched as-built samples with focused ion beam lift-out.

- XRD residual stress measurement of M300 samples built with different energy densities, scan strategies and build heights.

4. Application of a High Manganese Steel for L-PBF

4.1. Background

Additive manufacturing (AM) provides a unique pathway to achieve one-step fabrication of sophisticated geometry with superior resource efficiency. Metal AM processes often involve high cooling rate, localised energy input and relatively fast heat source movement speed. Trials of numerous commercial alloys demonstrated that ferrous materials are more processable with AM due to a smaller freezing range and adequate thermal properties. Among the commercially steels that are extensively studied in AM, austenitic 316 stainless steels fabricated in laser powder bed fusion (L-PBF) platforms have been shown to possess significant simultaneous improvement in both strength and ductility [16][33]. However, very little work hardening capacities were observed in these steels and the ultimate tensile strength of L-PBF built 316L SS was limited to ~700MPa. In the last decade, advanced high manganese steels were studied extensively and have been proven to be able to obtain excellent strength and ductility combinations [62][55][74]. Transformation and twinning induced plasticity (TRIP & TWIP) are the signatures of this class of steels and the activation of these two mechanisms are governed by the stacking fault energy, which directly correlates to the chemical composition of the steel [75]. Early stages of TWIP steel development highlighted the excellent uniform elongation which favours the formability and crashworthiness desired by the automobile industry. To circumvent the low yield strength commonly observed in most TWIP steels, grain refinement was conducted via severe plastic deformation (SPD) and rapid annealing process, which cannot be applied to realistic dimensions [55]. In comparison, the hierarchical microstructure associated with L-PBF provides consistent strengthening in the “as-cast” status of the part, making L-PBF a suitable candidate for processing TWIP steels.

Previous trials of applying TWIP steels to AM mainly focused on creating lattices for energy absorption applications with known TWIP steel compositions [76][77]. Since the comparison of mechanical properties is often made against wrought material the advantage of additively manufactured steels may be exaggerated. To provide better understanding in designing alloys for additive manufacturing and how the microstructure responds to strain differently after AM processing, a direct comparison study is needed to testify whether L-PBF is a viable strengthening process for all alloys. In the present study, a highly printable TWIP steel was designed. Thermomechanical processing was applied to maximise its cold-worked mechanical performance. Weldability based on conventional welding diagrams and laser weld test was examined and the mechanical properties were registered. This was followed by atomisation

and L-PBF fabrication of test parts with the exact chemical composition. The microstructure and mechanical properties of additively manufactured TWIP steel was then studied in detail to understand the offset in mechanical properties, providing guidance to future studies of designing alloys for additive manufacturing.

4.2. Scope of this study

To fully utilise the unique hierarchical microstructure resulting from L-PBF, a high manganese austenitic twinning induced plasticity steel will be designed. The alloy composition is designed based on the following aspects

- Achieving sufficient stacking fault energy to allow deformation twinning to occur
- Good weldability for minimum defect susceptibility in an additive manufacturing environment
- Superior mechanical properties compared to L-PBF built 316L stainless steel
- Possible stress-relief capability enabled by ϵ -martensite

Further to this, comments will be made on whether L-PBF has the capability to replace conventional multi-stage processing of high manganese steels and result in superior properties in its as-built status.

4.3. Alloy design and weldability test

Fully austenitic TWIP steels often contain 15-30 wt.% manganese and 0-1 wt.% carbon. Table 4-1 shows a range of TWIP steels that contains a reasonable amount of carbon.

Table 4-1: Chemical composition of previously reported TWIP steels and their deformation mechanism.

	Composition	Deformation Mechanism
Gao et al. [55]	Fe-22Mn-0.6C-xCu	TWIP
Springer & Raabe [62]	Fe-30Mn-1.2C-xAl	-
Escobar et al. [78]	Fe-17Mn-3Al-2Si-1Ni-0.06C	TWIP+TRIP
Mujica et al. [79]	Fe-22Mn-0.6C	TWIP
Rahman et al. [54]	Fe-15Mn-2Al-2Si-0.7C	TWIP

From a welding metallurgy perspective, high carbon is usually not desired as it increases the hardenability of the steel. In addition, since this study does not pursue breakthroughs in mechanical performances, the combination of manganese and carbon only need to provide enough stabilisation of the austenite phase. To achieve a balance in weldability and austenite stability, a composition of Fe-18Mn-2Al-0.5Si-0.3C was proposed in this study. Apart from providing oxidation resistance, 2 wt.% of aluminium was added to provide resistance to hydrogen embrittlement. 0.5 wt.% silicon was added for further solid solution strengthening. Fig 4.1 shows the positioning of this steel on Suutala diagram and Schaeffler diagram.

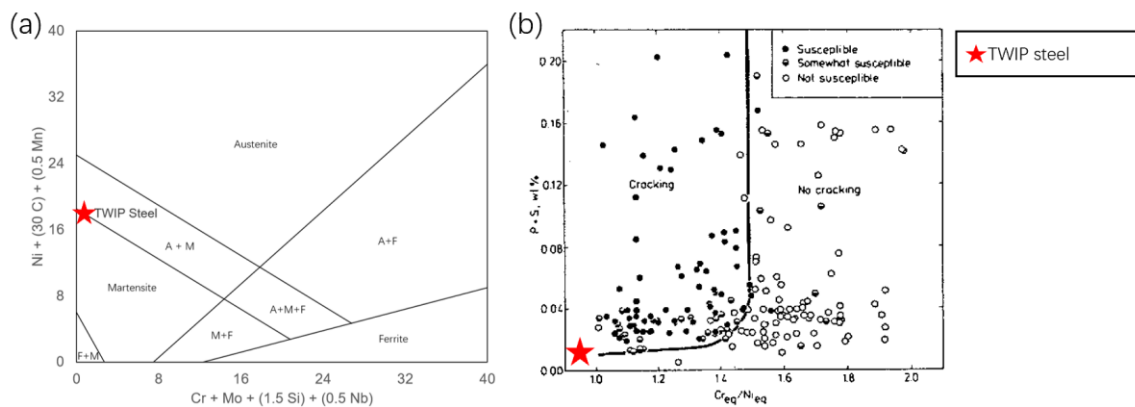


Figure 4.1: (a) Schaeffler diagram prediction based on the composition proposed for this study, the present composition is predicted to yield austenite and martensite in the weld region. (b) Original Suutala diagram showing that the present TWIP steel is susceptible.

A dual phase austenite & martensite microstructure is predicted to be present in the solidified microstructure with its positioning on the Schaeffler diagram. Due to the large wt.% of Mn present in high manganese TWIP steels, the calculated Cr/Ni equivalent ratios suggest that regardless of minor alloying alterations, high manganese TWIP steels are most likely predicted to be susceptible to solidification cracking on the original Suutala diagram.

The laser welding test carried out in Aconity Mini with a laser power of 150W and a scan speed of 1000 mm/s reveals presence of cracking along the laser scan direction. Fig 4.2 shows an optical micrograph of the crack location.

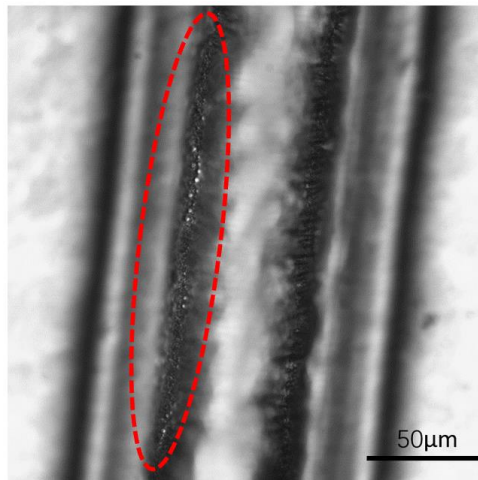


Figure 4.2: Optical micrograph of the crack formed in weld test of proposed TWIP steel.

Although the Suutala diagram has predicted the proposed composition to be susceptible to cracking, previous studies in laser joining of TWIP/TRIP steel have shown good weld quality in steels with much higher carbon and manganese content [79]. Parameters associated with this experiment will be utilised in the atomised powder and discussion will follow.

4.4. Mechanical properties of conventionally manufactured TWIP steel

The mechanical properties of conventionally manufactured TWIP steel are shown in Fig 4.3. A yield strength of 357MPa and a UTS of 873MPa were obtained from this specimen. An elongation to failure above 60% was also obtained. Based on the review of grain size effect on the strength and ductility of TWIP steel, higher UTS might be achievable with more refined grain size [54].

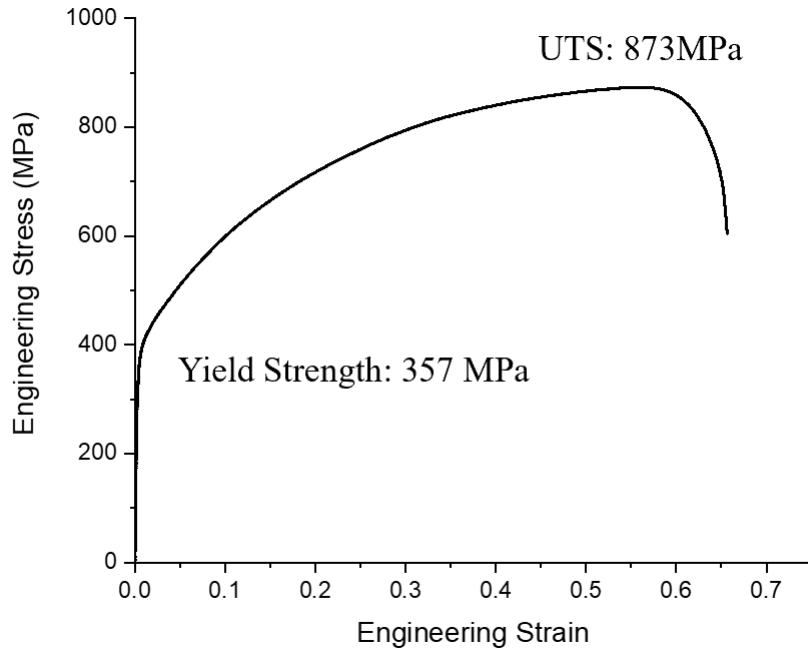


Figure 4.3: Engineering stress-strain curve of cold-rolled & annealed TWIP steel.

Strain hardening analysis of this specimen shows that a highest strain hardening rate of 2931MPa was achieved at 488 MPa true stress. The strain hardening rate then decreased to 1650MPa before serrated flow took place at 40% strain.

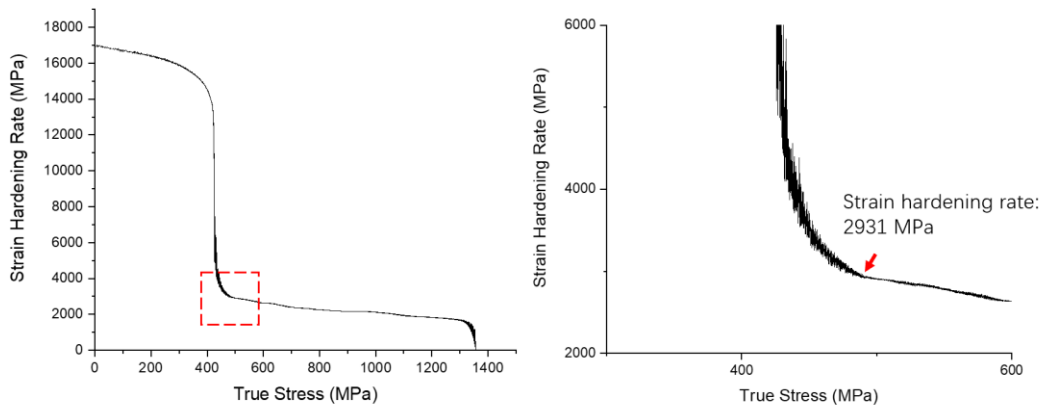


Figure 4.4: Kocks-Mecking analysis of conventionally manufactured TWIP steel.

As shown in Fig 4.4, the peak strain hardening rate of 2931 MPa in the present TWIP steel is comparable to some of the ultra-fine grained TWIP steels, such as 2900MPa reported by Gao et al. [15]. However, the reduction in strain hardening rate is very noticeable. Interestingly, the study conducted by Liu et al. demonstrated a continuous increasing strain hardening rate in additively manufactured 316L SS [33]. It is suggested that the dislocation cell structure contributed to this sustaining increase in strain hardening rate. Wang et al. however shows a

declining strain hardening behaviour similar to this work [16]. The role of the dislocation network will be further investigated.

4.5. Deformation mechanism of conventionally manufactured TWIP steel

To further investigate the origin of high work hardening rate found in the proposed composition, electron microscopy analysis was conducted on a strained-to-failure sample. Fig 4.5 shows the EBSD IPF and phase map taken 2-3mm from the fracture surface.

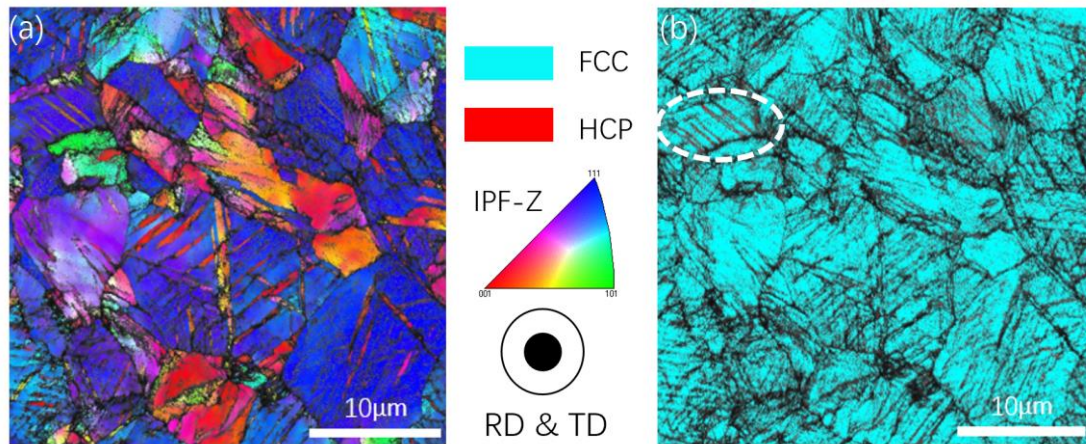


Figure 4.5: (a) EBSD IPF-Z of fractured TWIP steel. High density of deformation bands can be seen in the microstructure. (b) EBSD phase map of fracture sample, red deformation bands circled in white in the top left corner of (b) are indexed as ϵ -martensite.

From literature, twinning is the dominant deformation mechanism of TWIP steels that have similar compositions [57]. In later stages of deformation, thin bands of ϵ -martensite have nucleated in pre-existing deformation bands, as illustrated in Fig 4.5b. This observation is in agreement with the XRD spectrum of the rolled TWIP sheet in this study, shown in Fig 4.6. After rolling to a 60% thickness reduction, the steel sheet exhibits a tri-phase microstructure, with austenite and martensite being the dominant phases. This shows that γ - ϵ - α might have taken place during the rolling of TWIP steel sheet. Similarly, the ϵ -martensite observed in the fractured sample shows that γ - ϵ occurred during a later stage of plastic deformation. Rietveld refinement calculation shows that 42.2% of austenite, 41.4% of α' martensite and 16.4% of ϵ martensite are present in the as-rolled microstructure.

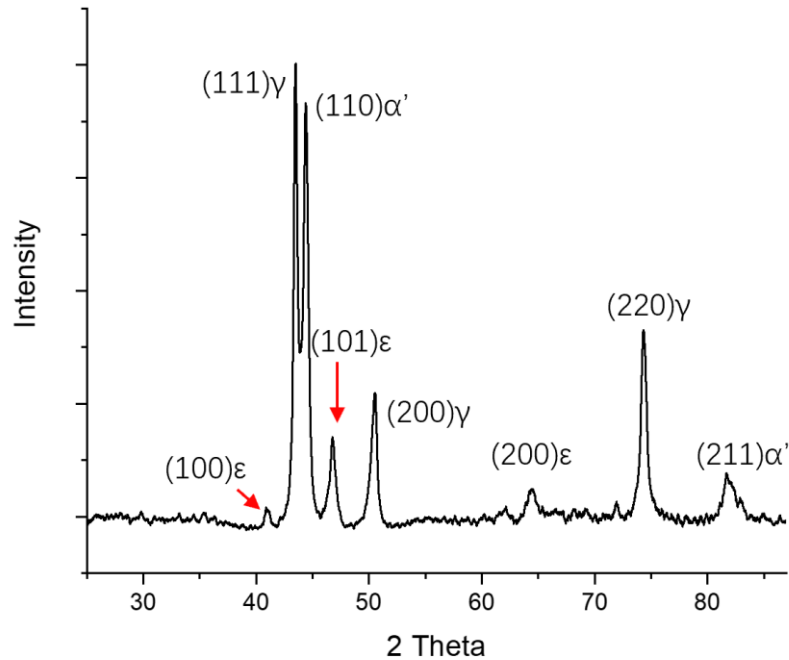


Figure 4.6: XRD spectrum of as-rolled TWIP steel sheet. Both transformation products (ϵ and α') can be seen.

To summarise, the proposed Fe-18Mn-2Al-0.5Si-0.3C composition achieved a desirable combination of strength and ductility with conventional thermomechanical processing. A relatively low yield strength is present due to the realistic annealing condition that was applied. In terms of weldability - although a lower carbon content would normally be considered to contribute to better printability, the initial laser weld test revealed cracking to occur close to the bottom of the melt pool.

4.6. L-PBF of atomised TWIP steel powder

To discover the processing window of atomised TWIP steel, a 5 by 5 processing parameter optimisation design of experiment was carried out. Densities measured with Archimedes method are shown in Fig 4.7. The as-built samples were only measured once due to severe oxidation when in contact with water. Interestingly all parts from the measurement achieved 99% dense. The parameter that induced crack in the laser weld test even registered 99.71% density.

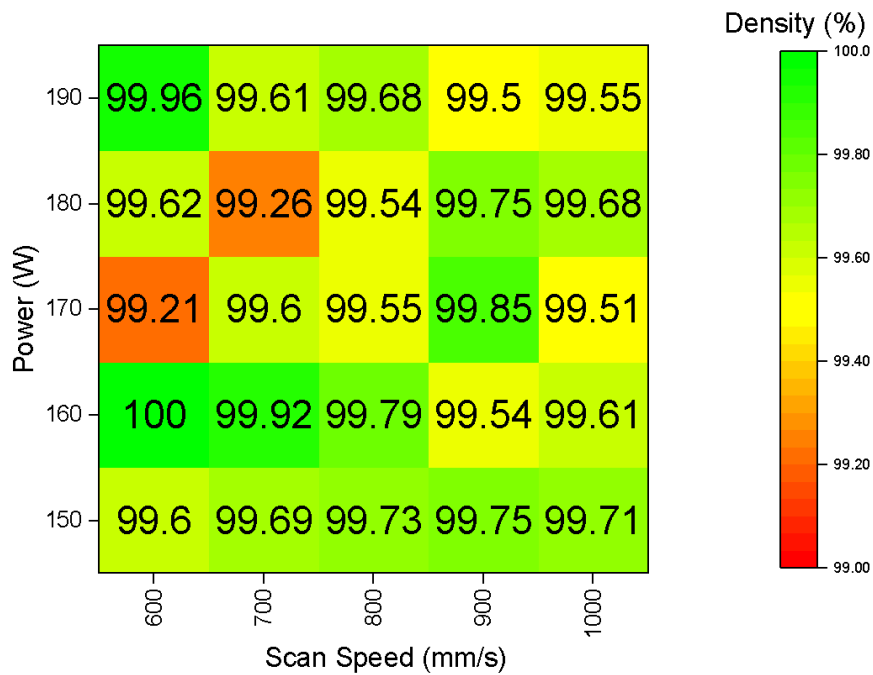


Figure 4.7: Density measured from cubes built in the DoE. All samples registered above 99% density indicate that the proposed TWIP steel exhibits good printability.

4.7. Microstructure of as-built TWIP steel

The microstructure of as-built TWIP steel is shown in Figure 4.8. It resembles a typical AM microstructure of high aspect ratio grains and nano-meter dislocation cells. A high proportion of nano-gas pores can be seen alongside dislocation cells.

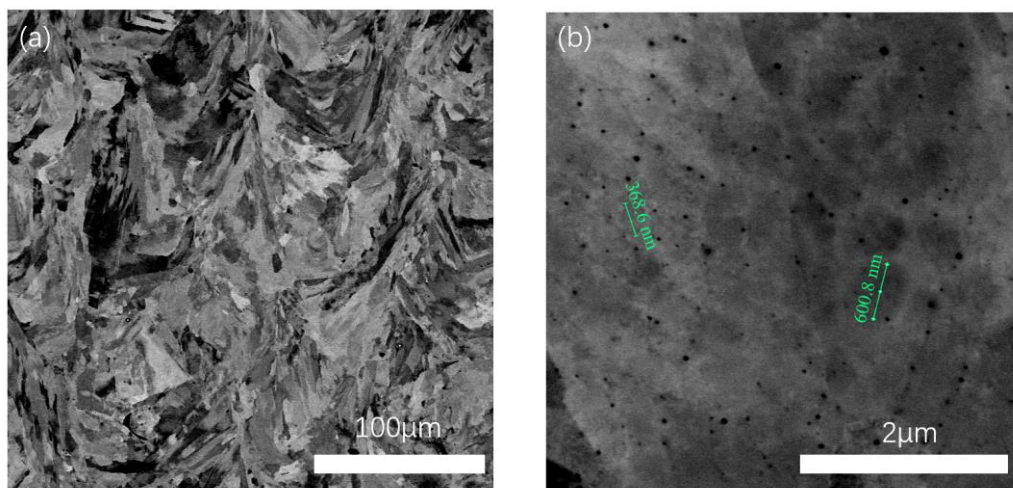


Figure 4.8: (a) Back scattered electron micrograph of as-built TWIP steels taken in the build direction. (b) Dislocation cell structure in the as-built TWIP steel. Nanometre sized gas pores can be seen in (b).

Further investigation with EBSD shows that as-built TWIP steel is fully austenitic with traces of $\Sigma 3$ boundaries. This phase constitution is further confirmed with XRD, which is shown in Fig 4.9. In addition, Fig 4.10 shows that a strong texture is present in the L-PBF built TWIP steel as the $(220)\gamma$ peak intensity is higher than that of the $(200)\gamma$ peak.

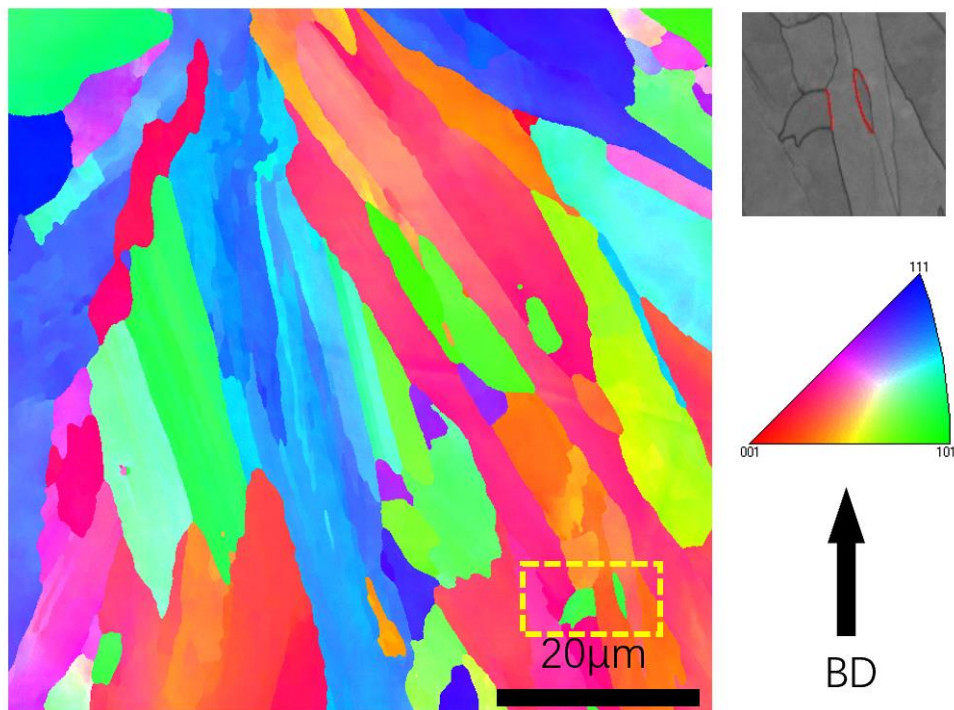


Figure 4.9: EBSD IPF-Z of as-built TWIP steel. Large aspect ratio grains contain neighbouring elongated cells with low misorientation angles. A site in the bottom right corner of the IPF containing $\Sigma 3$ boundaries highlighted in red is shown in the top right corner.

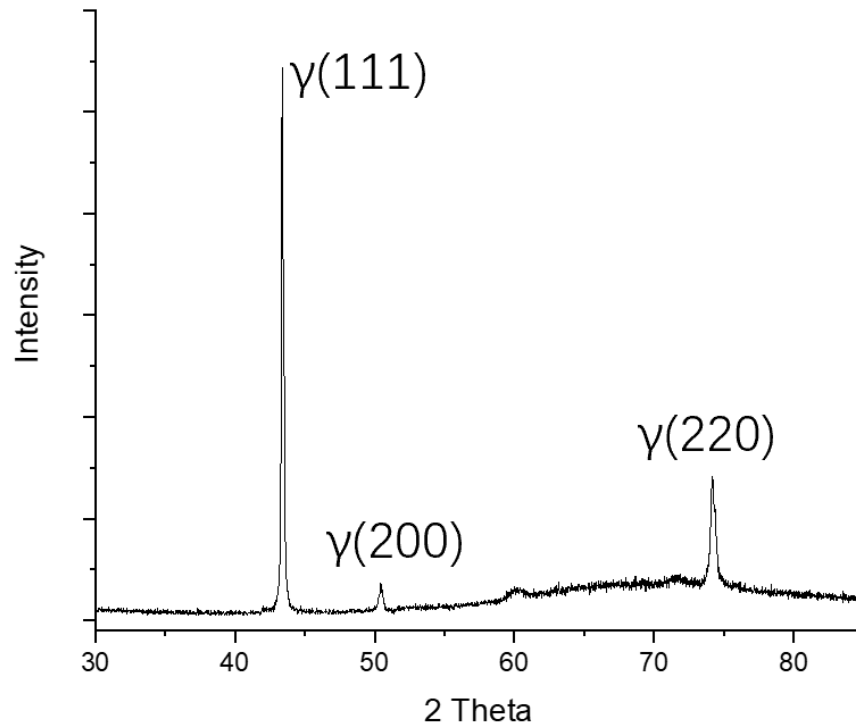


Figure 4.10: XRD spectrum taken from as-built TWIP steel. Note the higher intensity in (220) FCC peak.

To further investigate the presence of $\Sigma 3$ boundaries indexed in the as-built EBSD IPF, transmission electron microscopy was carried out. Bright field images confirmed the presence of twinning in $\{110\}$ planes. Fig 4.11 shows the nano-twins found in the as-built TWIP steel. These twins are likely formed by the thermal stress/strain associated with the L-PBF process. Apart from the thicker annealing twins shown in the yellow circled region of Fig 4.11, the red box also highlights annealing twins at a much finer thickness.

Previous studies in 316L SS highlighted the importance of the dislocation network. Scanning transmission electron microscopy and energy dispersive X-ray mapping were employed to image the dislocation cells and identify the segregation profile. The integrated STEM image is shown in Fig 4.12. Apart from the expected dislocation cell structure, some cell interiors also consist of high density of dislocations. Strong segregation of manganese and silicon can be observed in cell boundaries.

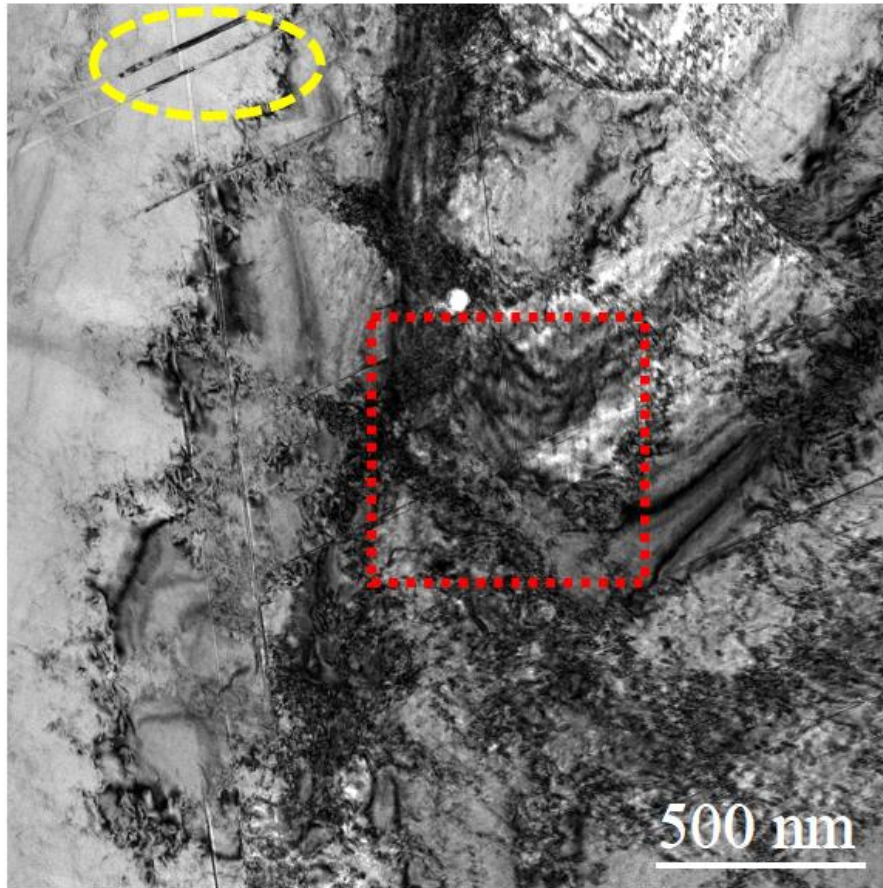


Figure 4.11: Bright field TEM micrograph showing the distribution of nano-twins in the as-built TWIP steel. The location of a grid-like finer twin intersection is highlighted in red.

In summary, the as-built TWIP steel exhibits a hierarchical microstructure formed by high aspect ratio grains and sub-micron dislocation cellular structure. Segregation of manganese and silicon is observed at cell boundaries, as well as low density of thermally induced nano twins.

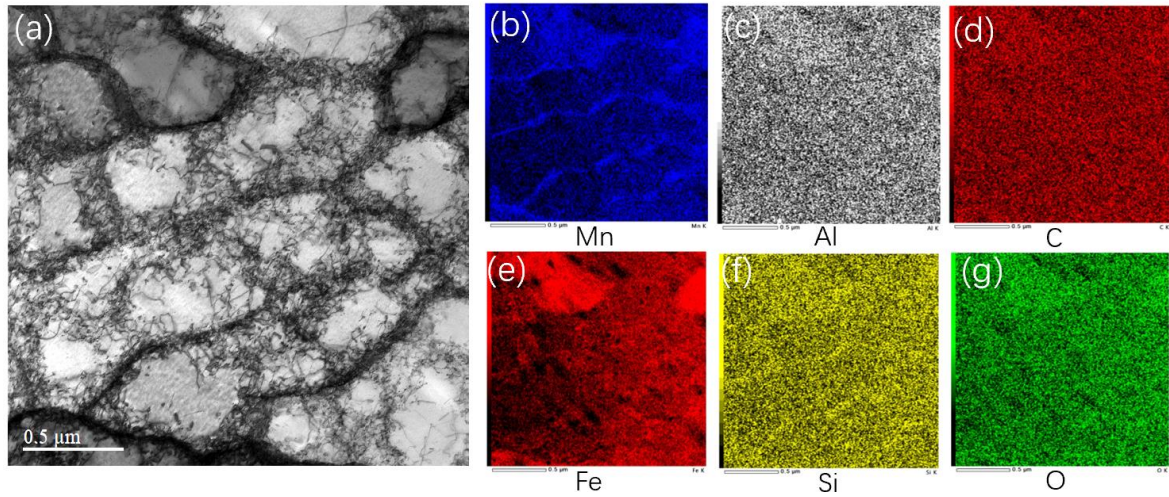


Figure 4.12: Bright field STEM image and EDS maps of the as-built TWIP steel. Strong segregation of Mn can be observed in (b).

4.8. Mechanical performance of L-PBF built TWIP steel

The tensile properties of L-PBF built TWIP steel are demonstrated in Fig 4.13. An increase of 243MPa was observed in the yield strength of additively manufactured TWIP steel. However, this improvement came at a cost of total elongation. Moreover, not only does the plastic deformation start with a lower strain hardening rate of 2335 MPa, the rate of decline in work hardening rate is more significant than that of the conventionally made TWIP steel.

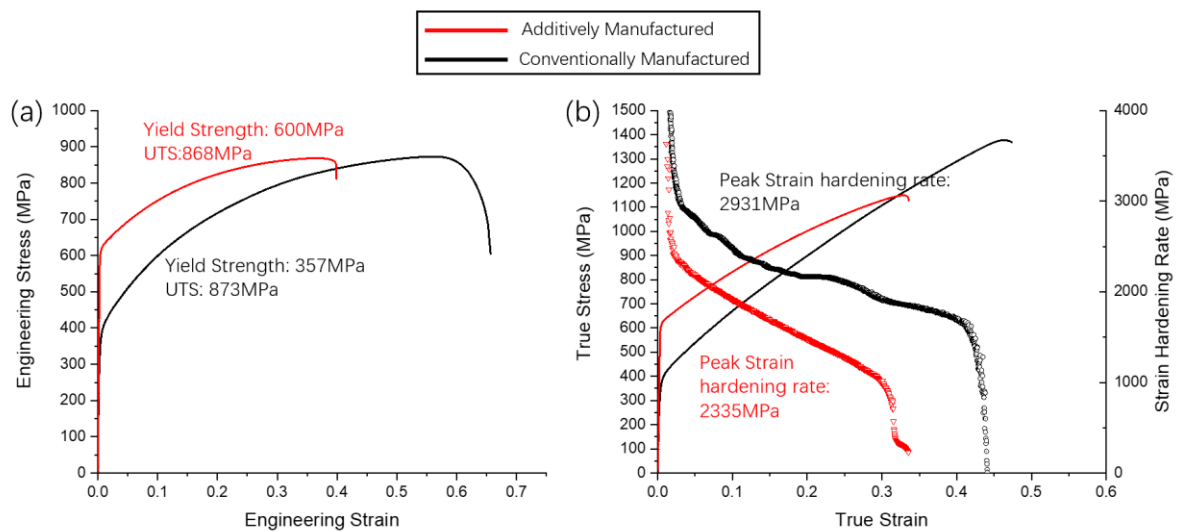


Figure 4.13: (a) Engineering and true stress strain curves of conventionally and additively manufactured TWIP steel, the trade-off between ultimate tensile strength and ductility can be seen in the AM built TWIP steel. (b) True stress-strain curve combined with strain hardening rate analysis showing the lower peak strain hardening rate of additively manufactured TWIP steel, as well as the step decline in strain hardening rate.

4.9. Deformation mechanism of additively manufactured TWIP steel

To further decipher the trade-off in tensile properties, advanced microscopy work was carried out on intermediate strained samples. Fig 4.14 shows the EBSD IPF and phase map of L-PBF built TWIP steel at 25% total strain. Apart from two sets of elongated deformation bands, a small fraction of ϵ -martensite can be seen in the twinned regions.

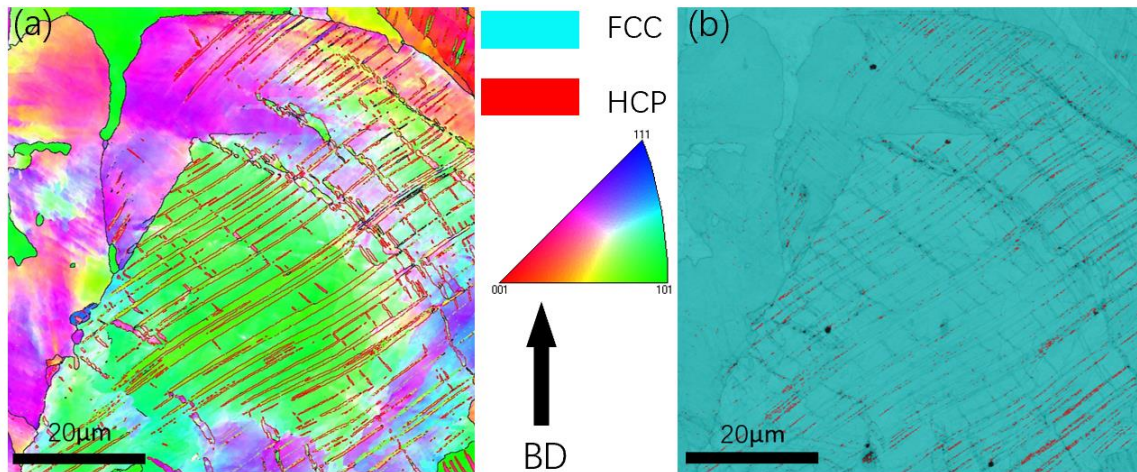


Figure 4.14: (a) EBSD IPF with $\Sigma 3$ grain boundaries highlighted in red showing the distribution of deformation twins in the TWIP steel sample strained to 25%. (b) Phase map of L-PBF built TWIP steel showing the presence of ϵ -martensite formed in twin bands.

Interestingly, the corresponding XRD spectrum does not reveal the presence of ϵ -martensite, as illustrated in Fig 4.15. This indicates that transformation took place but at a limited proportion. The steady decline in the strain hardening rate also confirms this statement, compared to the multi-stage variations observed in the conventional sample. TEM diffraction also shows that FCC deformation twins are present in the microstructure, illustrated in Fig 4.16.

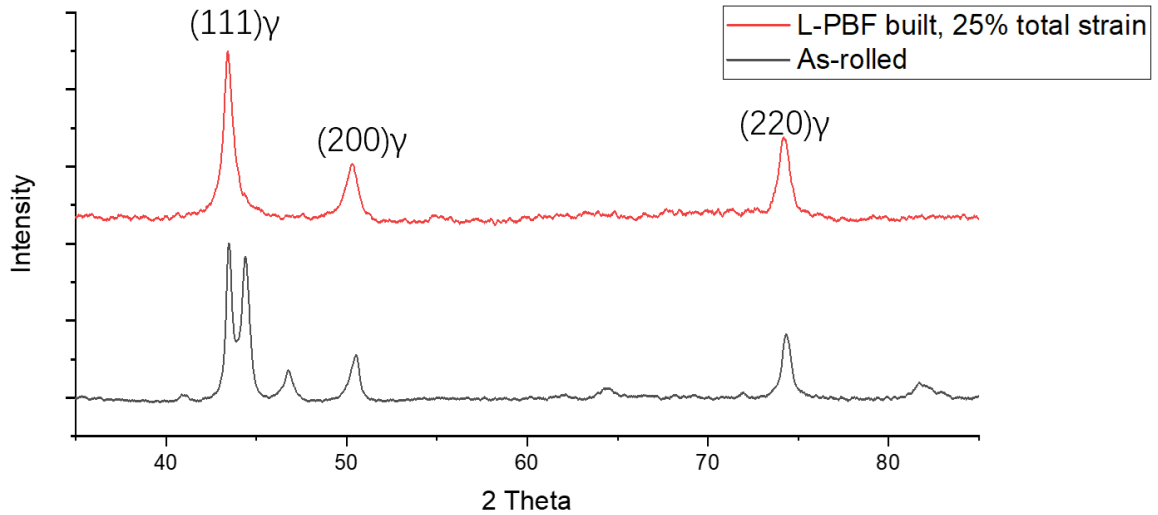


Figure 4.15: XRD spectrum comparison between strained L-PBF built tensile bar and severely deformed TWIP steel. Absence of transformation product can be seen in the L-PBF built steel. Peaks in the as-rolls sample are labelled in Fig 4.6.

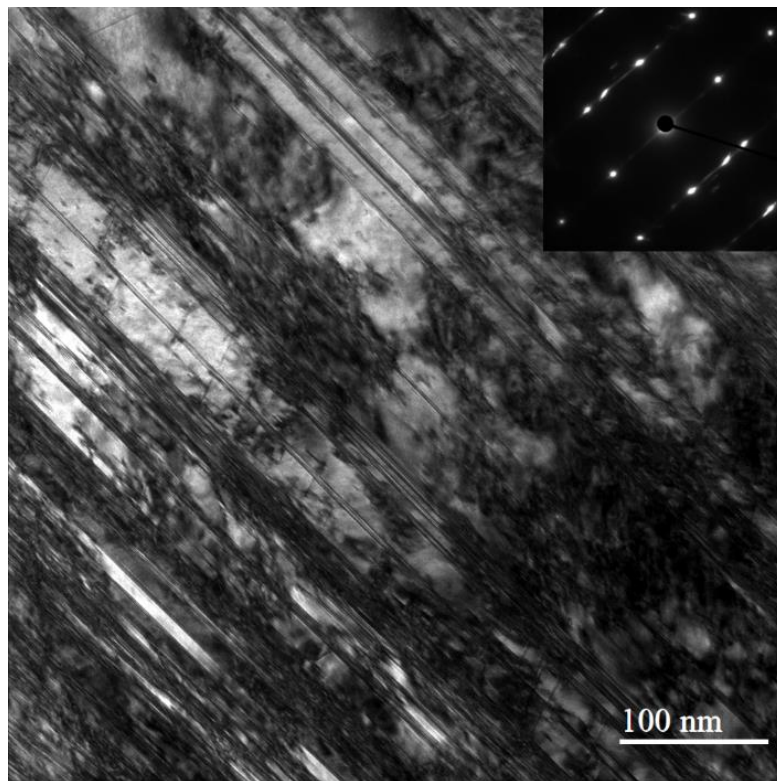


Figure 4.16: Bright field TEM micrograph showing high density of deformation twinning and dislocation forests. SAD insert shows diffraction spots of the FCC matrix and twin. Image taken in $[110]$ zone axis.

4.10. Discussion

During the L-PBF process, materials with low crack susceptibility, good powder flow rate and small freezing range are more likely to be fabricated successfully [80]. The TWIP steel

proposed for this study does not contain any high melting point carbide forming elements such as niobium and molybdenum. Alongside with a relatively small addition of carbon, this steel is supposed to be more printable than some of the high carbon tool steels and high alloy steels [81][69]. While the present alloy composition exhibits a relatively large processing window, the weld test results show a clear conflict between welding metallurgy prediction and experimental results. This conflict can be explained by the cooling rate difference between welding and AM, as well as the re-melting nature of additive manufacturing [36]. In addition, more accurate results can be obtained from adding power to the weld test, which enables the simulation of melt-pool shape and realistic parameter estimations [20]. Therefore, further work is needed to propose more compatible weld test or simulation techniques for novel alloy compositions.

In the present study, the yield strength of as-built Fe-Mn TWIP steel is successfully enhanced to 600MPa, matching that of some of the nano-grained TWIP steel [55][54]. The yield strength increment is mainly attributed to the dislocation cell structure which is still retained at 25% total strain. Fig 4.17 shows the enlargement of nanopores and formation of cavities in the deformed microstructure.

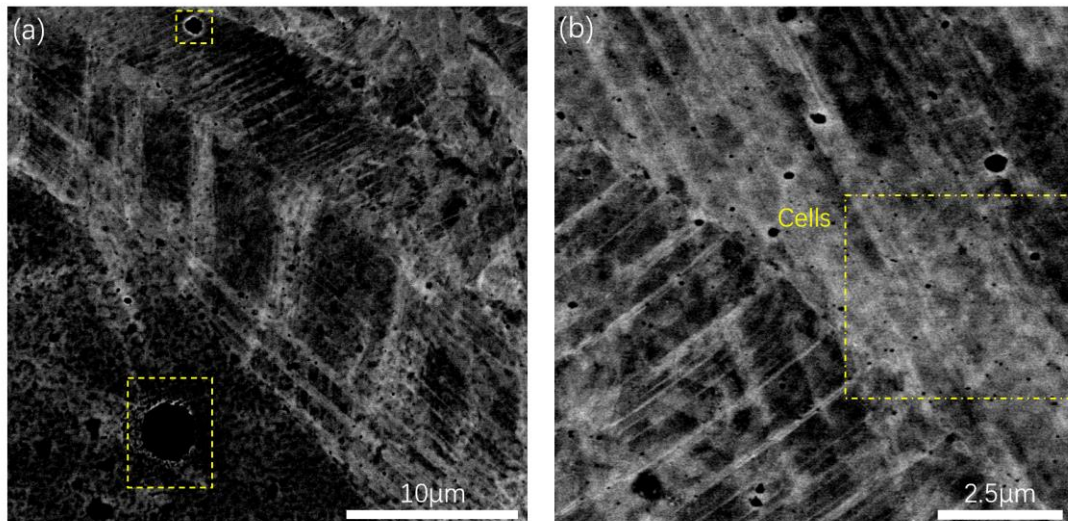


Figure 4.17: Backscattered electron micrographs showing cavities and remaining dislocation cells in L-PBF built TWIP steel strained to 25%.

Alongside with the formation of deformation twinning at intermediate stage of straining, a stable work hardening behaviour was achieved in the L-PBF built TWIP steel. Yet when compared to conventionally manufactured TWIP steel, the UTS of as-built Fe-Mn TWIP steel failed to improve. This is as a result of the noticeably lower initial strain hardening rate (2235

MPa) and its steeper rate of decay during plastic deformation with comparison to the conventionally processed material.

Unlike other studies where the AM samples were compared to well-annealed material, the counterpart specimen in this work was produced through well-controlled thermomechanical processing. Although deformation twinning occurs in both groups of samples, conventionally manufactured TWIP steel triumphs in finer grain size which led to higher population of intrinsic high angle grain boundaries. The high aspect ratio grains in additively manufactured TWIP steel resulted in larger mean-free-path for dislocation movement even after plastic deformation, which can be seen in Fig 4.14(a).

Furthermore, the prolonged activation of γ - ϵ - α' transformation in conventional TWIP steel also delays the onset of necking, resulting in a superior elongation to failure. This transformation was only observed in local regions of the L-PBF built TWIP steel and thus contributed little to both the strain hardening rate and the elongation to failure. As the conventionally manufactured TWIP steel exhibit more than 40% α' and 16% ϵ martensite after the rolling process, it is evident that large scale martensitic transformation maybe suppressed in additively manufactured TWIP steel. In addition to the differences in strain accommodation mechanisms, the constant appearance of minor defects in L-PBF built TWIP steel also has a profound influence on the plasticity. Fig 4.18 shows the effect of tensile bar geometry on the tensile properties of L-PBF built TWIP steel. All three samples were fabricated with the same parameter, yet the larger tensile specimen exhibits 7% extra elongation to failure. This could be attributed to the laser return time which is defined by the time it takes to complete a single hatch line. When scanning on the long axis of the tensile bar, the build process will be 1.67 times faster in the smaller tensile specimen which may lead to overheating and formation of unwanted defects.

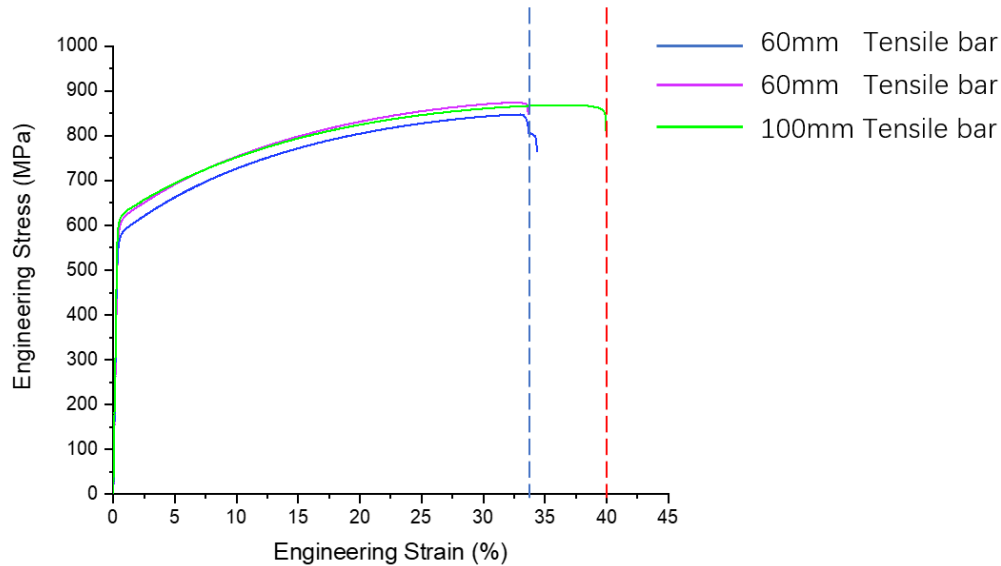


Figure 4.18: Engineering stress strain curves showing the size effect in L-PBF built TWIP steel.

Currently, additively manufactured high manganese TWIP steels are primarily proposed for structurally complex energy absorption applications that targets crash worthiness [76]. The present AM TWIP steel exhibits an energy absorption coefficient of 34720 MPa% (UTS x elongation to failure). Similar Fe-Mn TWIP/TRIP compositions built by L-PBF have also displayed similar level of crash worthiness [76][77]. This is a drastic reduction, especially comparing to the 52380MPa% calculated from the conventionally manufactured TWIP steel and 51200MPa% of the 316L stainless steel studied by Wang et al. [16]. This demonstrates that while L-PBF has the capability to significantly enhance the strength of legacy steel without compromising plasticity, the signature AM microstructure has mainly levelled up the yield strength of high manganese TWIP steel.

Although a fully austenitic steel was selected for this study, it is worthwhile pointing out that the metastability of austenite can be heavily influenced by the solidification cell structure. The effect of austenite grain size on the martensite start temperature was studied by Takaki et al. and it has been suggested that the elastic strain energy required for nucleating thin plate martensite is dramatically increased when the grain size is below 1 μm [82]. Figure 4.19 shows experimental observation of single variant transformation in ultrafine grained steel in comparison to multiple laths of martensite formed in fine grained steel.

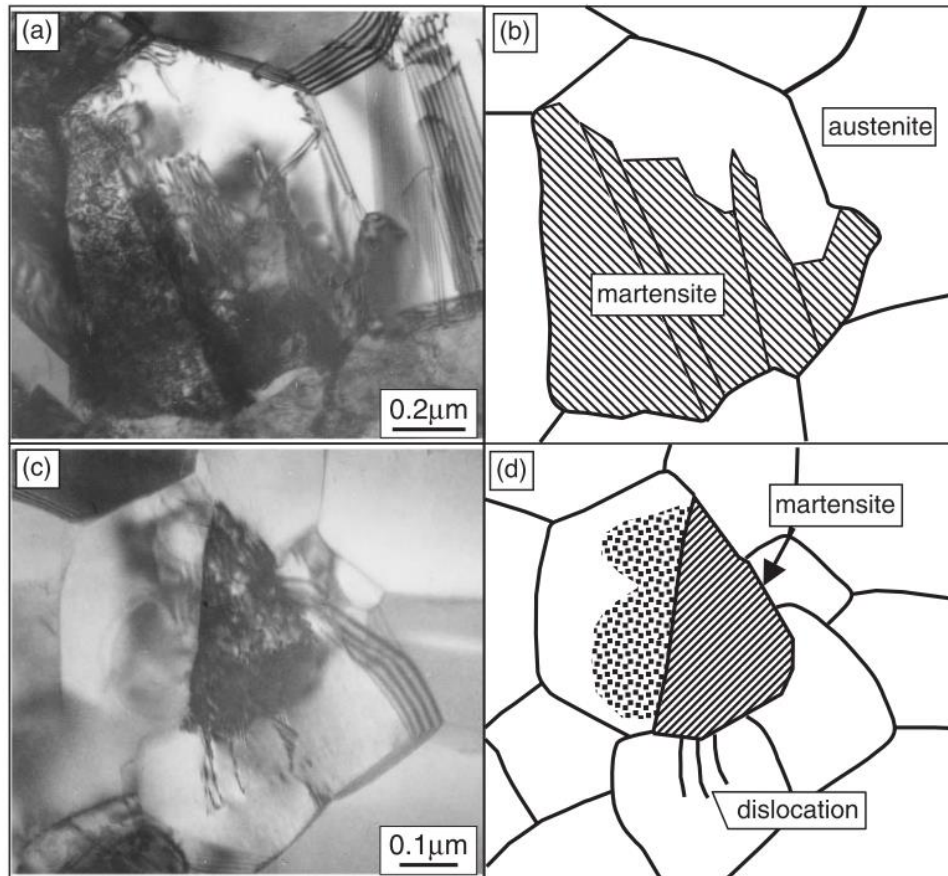


Figure 4.19: Transmission electron micrographs and corresponding drawings of the morphology of martensite inside (a) fine and (c) ultrafine austenite grains. With approximately 1 μm grain size, multiple laths with similar orientation are formed. When the grain size is further refined below 1 μm , a single lath of martensite is formed [82].

Recent studies in 17-4PH stainless steel show evidence of this phenomenon as martensitic steels such 17-4PH have retained significantly more austenite after the AM process. Facchini et al. demonstrated that retained austenite in additively manufactured 17-4PH can undergo martensitic transformation at room temperature and thus leading to a good combination of mechanical properties [83]. Freeman et al. further investigated the presence of retained austenite in as-built 17-4PH and it was discovered that with appropriate parameters a fully austenitic microstructure can be obtained in the as-built status, and that tailoring of phase fraction can be achieved with higher energy density which led to higher thermal strain [50]. These studies show that the solidification cell structure associated with L-PBF may result in complete suppression of martensite in steels with low martensite transformation temperature and thus enabling spatial grading of build parts where areas of fully austenitic and partially martensitic can be deposited.

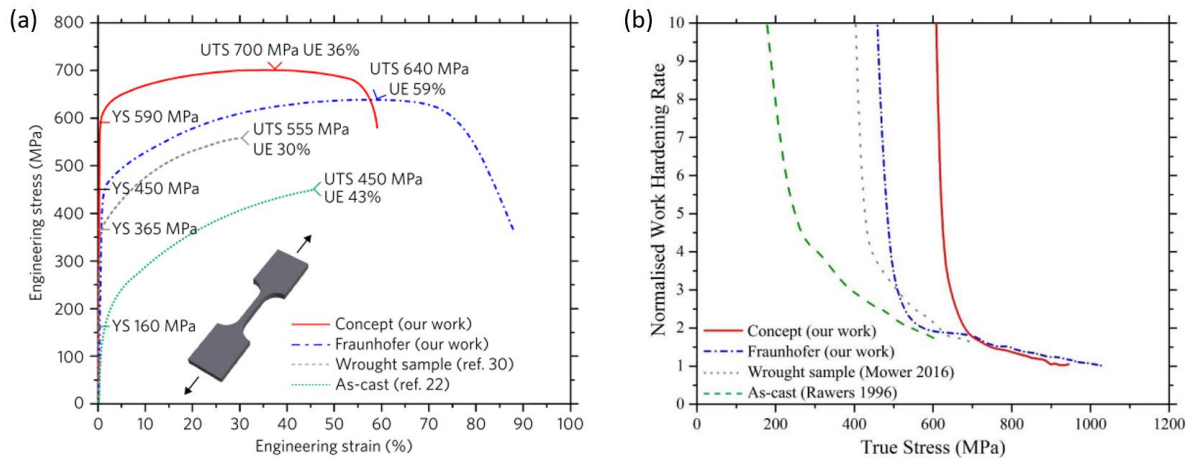


Figure 4.20: (a) Engineering stress strain curves of additively manufactured 316LSS. (b) Kocks-Mecking analysis of data presented in (a) showing a different strain hardening behaviour. Peak strain hardening rates were obtained after yielding and a steady decrease can be observed [16].

In comparison, the dislocation cells in the current chapter mainly serve as obstacles for dislocation movement. While the trapping of elements in cell wall regions was reported, its strengthening effect was not commonly regarded as significant [33]. Meanwhile, uncertainty can be seen in the strain hardening rate reported in additively manufactured 316L stainless steel, as depicted in Fig 4.20 where two different strain hardening behaviours are displayed in the Kocks-Mecking analysis. This shows that although the dislocation network indeed provided significant yield strength improvements, uncertainties sit within its role on ductility, strain hardening and its ability in altering the local chemistry. For high manganese TWIP steels that have potential application in energy absorption objects, the elimination of the cell structure may lead to better energy absorption capabilities.

4.11. Conclusion

In summary, a comprehensive study was commenced to compare the microstructure and mechanical performance between cold-rolled & annealed and additively manufactured high manganese TWIP steel. A typical dislocation cell structure was obtained in the as-built steel and deformation twinning was the main strain accommodation mechanism. The cellular walls contributed to the yield strength enhancement. As deformation twins were growing through low angle cell boundaries and terminating at high angle grain boundaries, coarse-grained L-PBF TWIP steel experienced a lower initial strain hardening rate which continuously declined. A superior elongation to failure was observed in the conventionally manufactured TWIP steel which attributes to a more pronounced γ - ϵ - α' transformation. This trade-off in mechanical properties is shown in Fig 4.21.

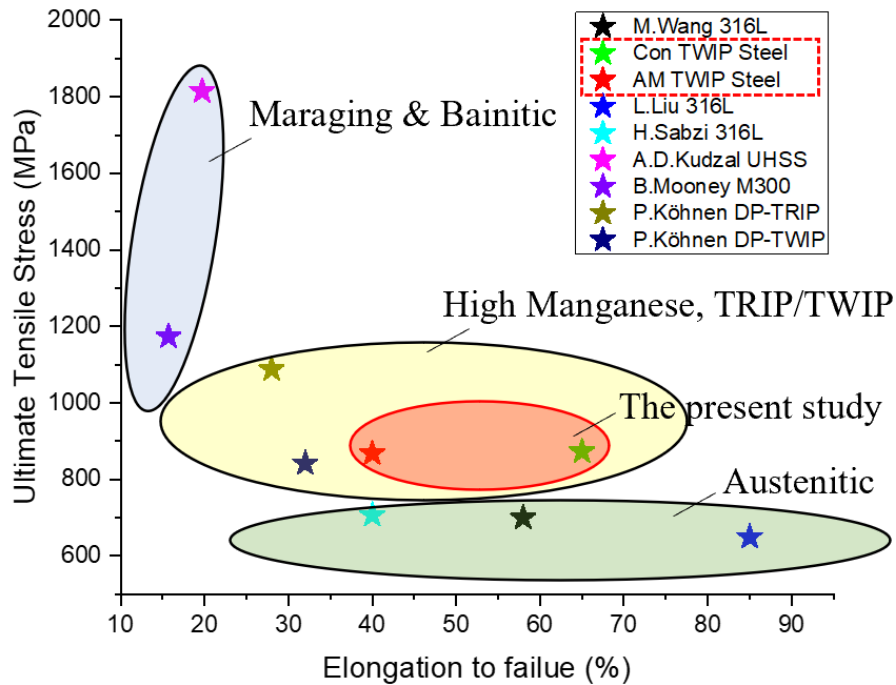


Figure 4.21: Performance comparison between the known studies of L-PBF built steels and the present study. The steels designed in the present study shows improved ultimate tensile strength when compared to legacy austenitic stainless steels and superior ductility in comparison to previously reported additively manufactured high manganese steels [16][33][84][46].

This study demonstrates that additively manufactured steels may not triumph in all aspects of mechanical performance when compared to thermo-mechanically processed counterparts. The conflict between build quality and weldability prediction shows that non weldable alloys can indeed be processed with L-PBF, and pre-existing empirical welding equations need adjustments towards the high cooling rate and layer by layer rescan nature of additive manufacturing. The enhancement in yield strength indicates that the L-PBF is a viable pathway to address the low yield strength drawback of high manganese TWIP steel though the trade-off in ductility leads to a less appealing energy absorption coefficient. The dislocation network in additively manufactured steels have shown different behaviours as it has demonstrated to directly influence the work hardening rate. Moreover, although the parameters used in the present study have resulted in densities above 99%, the porosities observed in the microstructure is also affecting the ductility of as-built samples. The preparation of conventional counterpart material in this study is simple and should be readily applicable to other engineering alloys. The present study should provide enough insights to rapid comparison between conventional and additive route of manufacturing the same alloy.

5. Metastability of Austenite in Additively manufactured M300 Maraging Steel

5.1. Background

Laser powder bed fusion (L-PBF) is a novel technique for producing high strength alloy parts with improved resource efficiency. The rapid thermal cycles associated with the additive manufacturing (AM) process result in a hierarchical microstructure, giving rise to excellent mechanical properties observed in legacy alloys such as 316L stainless steel. In addition to enhancement in mechanical properties, interesting findings were reported around martensitic steels manufactured by AM. Facchini et al. stated that L-PBF has enabled transformation induced plasticity (TRIP) behaviour in additively manufactured 17-4PH, resulting in a superior combination of strength and ductility [69]. Freeman et al. followed up on the metastability of austenite and discovered that a fully austenitic microstructure can be achieved in 17-4PH, a steel that is supposed to be fully martensitic [50]. Interestingly, retained austenite in 17-4PH is so sensitive that magnetic testing was the only way to confirm the phase constitution in additively manufactured 17-4PH, as any form of metallurgical preparation leads to phase transformation, which made microscopy characterisation of the “true” as-built microstructure extremely difficult.

Retained austenite that can further undergo phase transformation has engineering significance as the TRIP behaviour can be utilised to improve ductility in ultra-high strength steels [85]. The capability of retaining additional volume of metastable austenite is therefore desirable and should be studied further. Moreover, since surface preparation can lead to bulk transformation, it shows that additively processed metastable steels can act like structure sensors or even in-situ strain gauges. To gain further understanding of the metastability, a nickel rich maraging steel will be fabricated using L-PBF. Microstructure analysis of as-built and heat treated parts will be carried out to evaluate the retention of austenite. Surface magnetic testing will be introduced to accurately measure the amount of austenite transformed as a product of different levels of deformation.

5.2. Scope of the study

A wide range of literature can be found about M300 maraging steels. While the austenite reversion behaviour was investigated, none have demonstrated the use of magnetic testing except Freeman et al. [86][43]. It is assumed that a certain fraction of retained austenite undergoes martensitic transformation and the prepared surface led to a false understanding of the as-built phase fraction present in additively manufactured M300.

The aims of this study are listed as following:

- Characterise the microstructure of as-built M300, identify possible traces of transformation.
- Recover transformed austenite with sub-critical heat treatment. Investigate the difference in microstructure and segregation profile.
- Measure the response of metastable austenite to different levels of deformation.

5.3. Microstructure of as-built M300 maraging steel

Fig 5.1 shows scanning electron micrographs of as-built M300. Keyhole shaped defects and gas pores can be seen in the cross-sectional plane. Transitioning between dendritic and cellular structures can be seen. Interfaces in Fig 5.1 (b) are highlighted due to the presence of retained austenite and possible enrichment of solute elements.

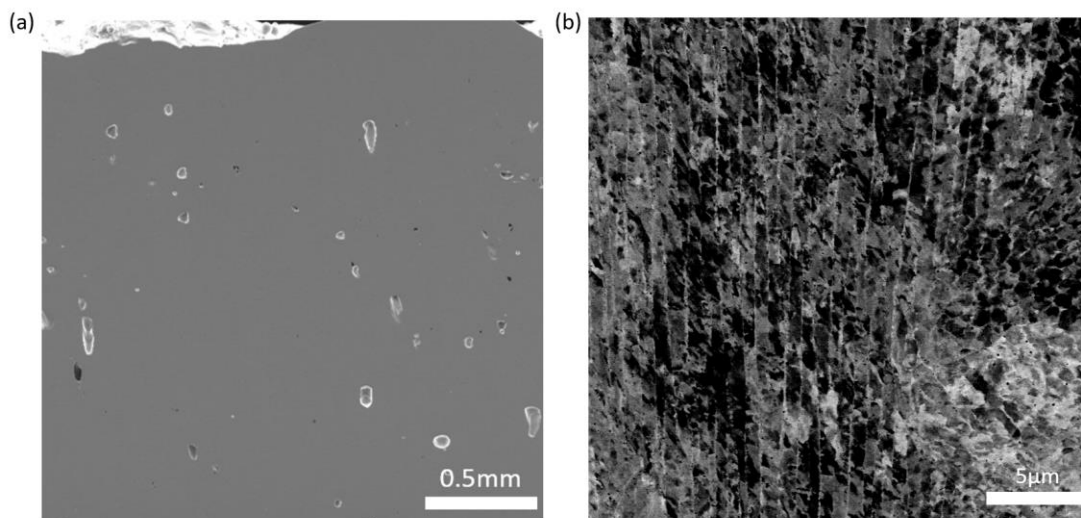


Figure 5.1: (a)Secondary electron micrograph showing the distribution of keyhole type defects in as-built M300. (b)Backscattered electron micrograph of as-built M300 showing solidification cell structures. Cell boundaries are highlighted due to the presence of retained austenite.

To further evaluate the phase constitution of the as-built M300, EBSD mapping was conducted and presented in Fig 5.2. In addition to the large grains and nanometre size cells with different orientation, a crescent-shape austenite band was obtained [87]. Interestingly, the dislocation cell network was not indexed within the areas of large austenite bands. Transmission electron microscopy images reveal that transformed solidification cells in M300 contain high density of dislocations, as illustrated in Fig 5.3.

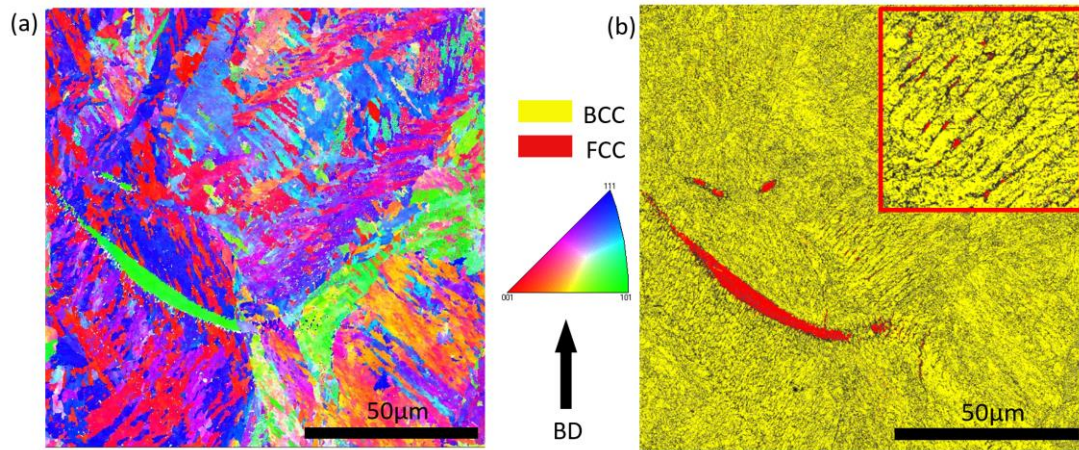


Figure 5.2: (a) EBSD IPF and (b) phase map of as-built M300. Insert in (b) shows a magnified region where distribution of retained austenite can be seen. The colouring of phases is shown in the legend. ImageJ calculation shows around 6.9% of austenite is present in b).

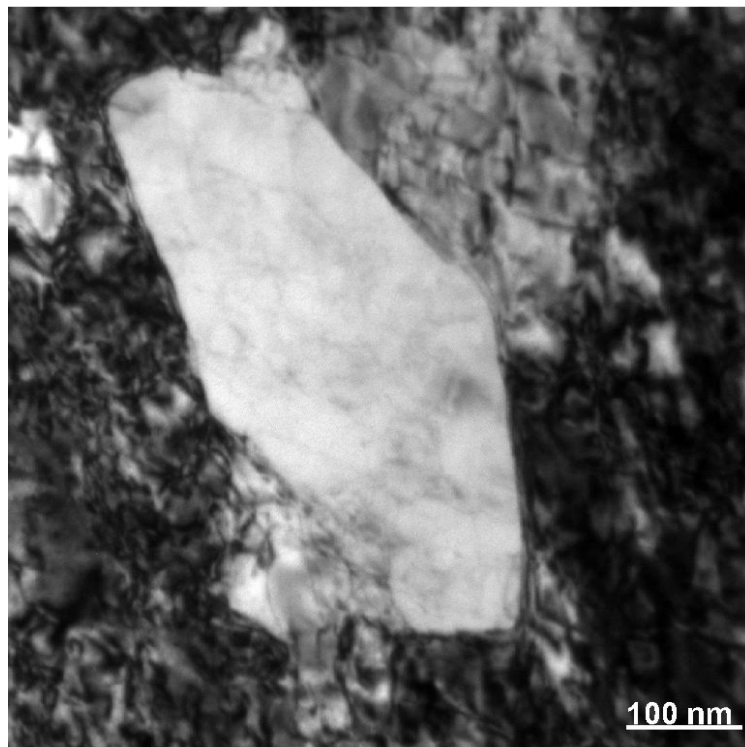


Figure 5.3: Off-axis imaged dislocation cell in additively manufactured M300.

To confirm elemental segregation in cell boundaries, STEM EDS mapping was carried out and the results are depicted in Fig 5.4. Titanium was the only element found in cell boundaries where retained austenite does not exist.

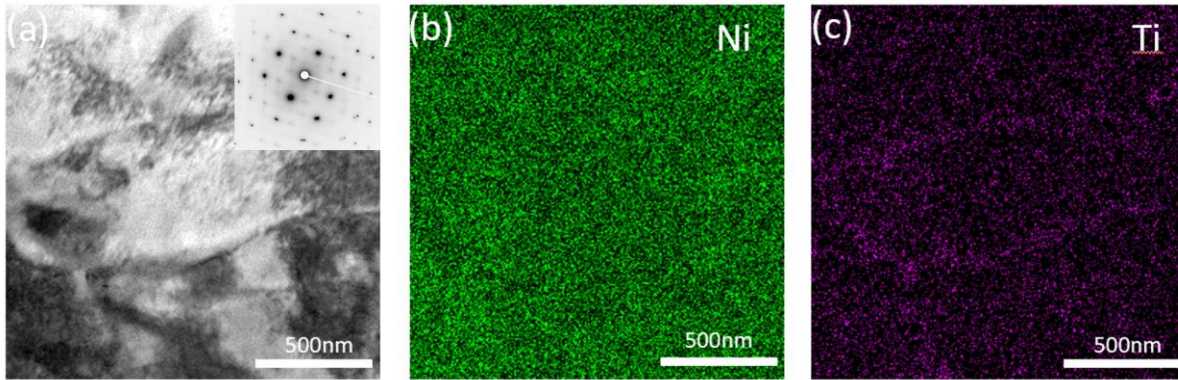


Figure 5.4: (a) BF-STEM micrograph showing the outline of a dislocation cell. Insert SAD shows the [110] BCC zone axis with weak response of precipitates and largely confident fully martensitic matrix. (b) and (c) STEM EDS maps showing the segregation profile of Ni and Ti, respectively.

So far, it is established that the as-built M300 is near fully martensitic after surface preparation. Large bands of crescent shape austenite can be seen and their presence is possibly linked to keyhole type melt pools. To reveal the true fraction of austenite in the as-built M300 and its forming condition, the sample will be heat treated below the critical temperature without the homogenisation step.

5.4. Microstructure of additively manufactured M300 maraging steel aged at 600°C

EBSD phase map of the aged M300 specimen is depicted in Fig 5.5. Massive reversion of austenite can be seen as some areas display a 50:50 ratio of austenite and martensite.

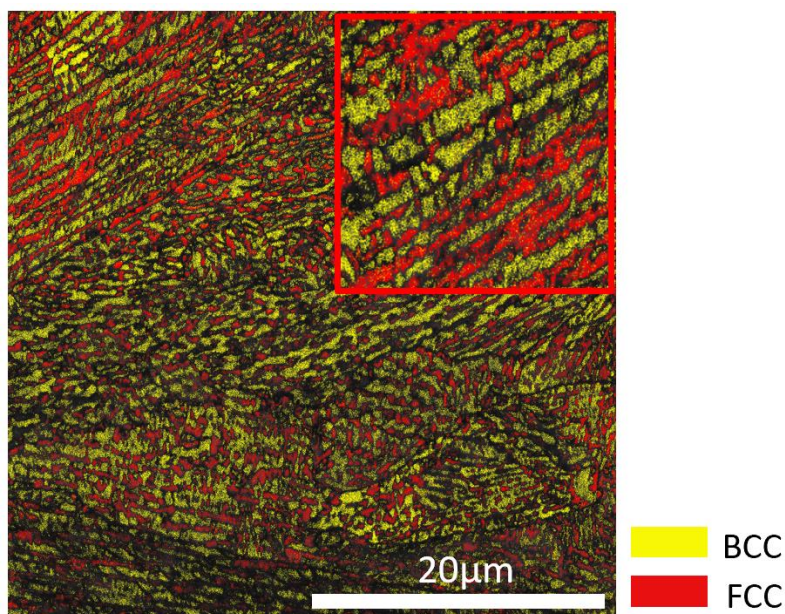


Figure 5.5: EBSD phase map of M300 heat treated at 600°C for 24hrs. Insert shows partial dissolution of cell boundaries. Map acquired at a step size of 0.1µm. ImageJ calculation shows 13% of austenite is present.

Due to the overall holding time, some dislocation cell walls are starting to dissolve, as demonstrated in the insert of Fig 5.5. Despite this, some regions still exhibit near-single variant martensitic transformation, as shown in Appendix Fig 3. Ex-situ EDS map was conducted near the EBSD site. Fig 5.7 shows strong Ni segregation in the austenite area. Point analysis shows that the grey region (austenite) is higher in nickel content, illustrated in Fig 5.6. This confirms that for austenite to obtain enough stability and circumvent transformation during surface preparation, a strong Ni segregation must be present. The amount of austenite recovered during the heat treatment process is displayed in Fig 5.8. The process completed after 50 minutes of holding.

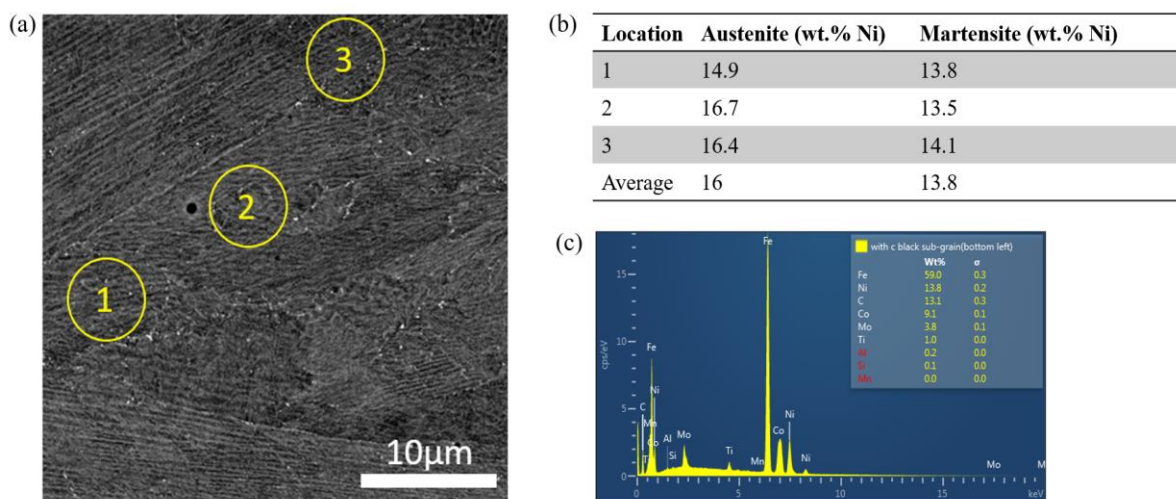


Figure 5.6: (a) Backscattered micrograph of the site of EDS point analysis. (b) Nickel content in grey (austenite) and black (martensite) islands, a clear enrichment of nickel in austenite can be seen. (c) Typical EDS spectrum of the point index, high carbon content is caused by the deposition during EBSD mapping.

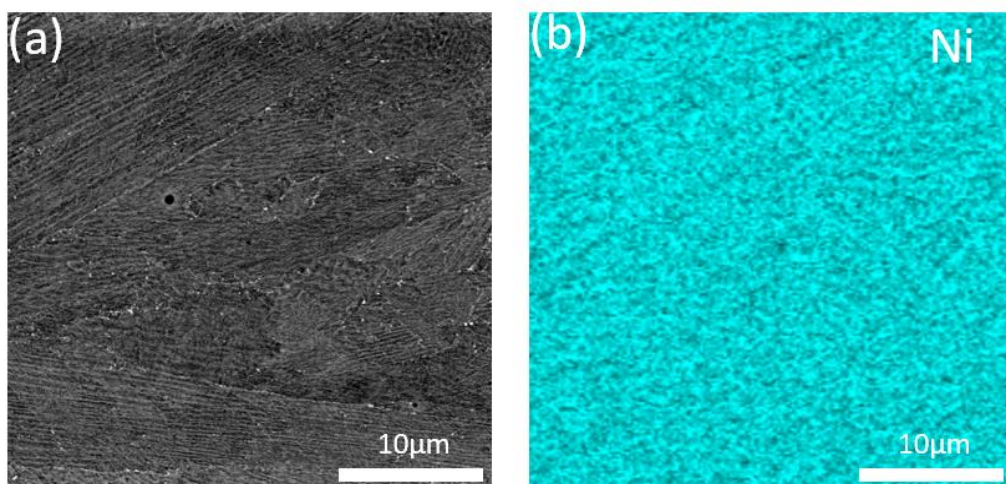


Figure 5.7: (a) Backscattered electron micrograph of aged sample. High contrast particles are precipitates. (b) SEM EDS map of Ni.

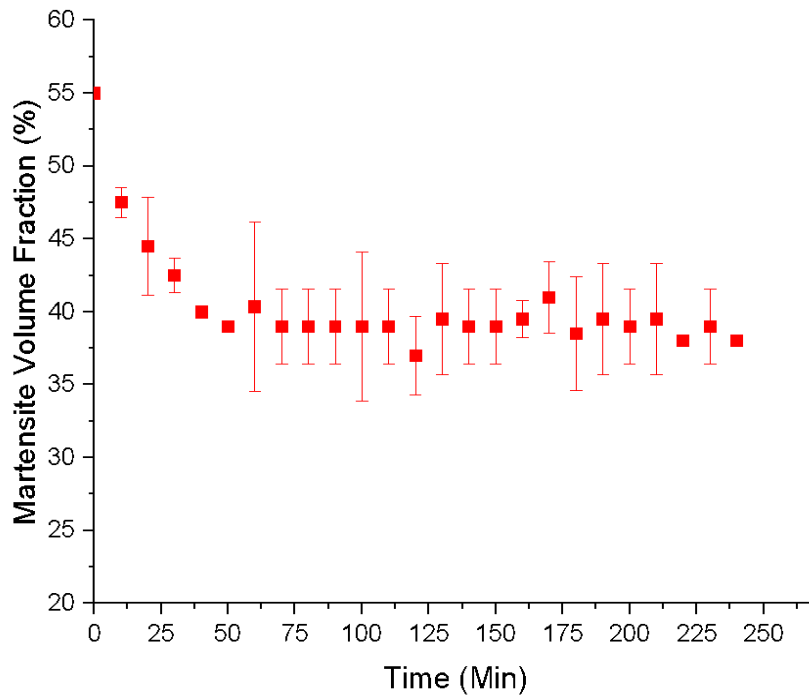


Figure 5.8: Recovery in austenite during the ageing heat treatment of M300 Rapid recovery of austenite can be seen in the first 40 minutes of ageing. The recovery process terminates after 50 minutes of ageing as the maximum austenite stability is reached. Further holding led to homogenisation and dissolution of cell boundaries which caused the fluctuation in readings.

5.5. Feritscope measurement of phase constitution

The phase fraction of magnetic material found in as-built, polished and tensile fractured M300 was compared to that of stress-free counterparts. The result can be seen in Table 5-1 were the Feritscope results are grouped with the state of surface preparation and deformation. Heated substrate is an established method for reducing residual stresses in metal additive manufacturing and low heating temperature is often adopted. In this study, the stress-free M300 samples were fabricated through a different pathway: The build temperature was raised to 500°C (substrate temperature at 700°C) to completely bar the martensitic transformation during the build, in addition to a much smaller temperature gradient. Upon completion, the build plate was gradually cooled down to room temperature in 90 minutes, which further eliminated any chances of quenching induced residual stress.

Tensile testing result in Fig 5.9a shows that heated bed built M300 exhibits slight reduction in yield strength and ultimate tensile strength. This is due to the recovery of dislocation in the microstructure while holding at 600°C in the duration of fabrication. However, the escalated

build temperature did not lead to complete dissolution of the solidification cell structure, nor the precipitation of intermetallic phases.

Table 5-1: Feritscope readings taken from M300 tensile specimens at as-built, strained, polished and fractured status. A clear trend of increasing volume fraction in martensite can be seen when the sample is subject to surface alteration or strain.

Detection Location	Vol.% of Martensite
Heated bed build, as built, holding area	52.61±1.08
Heated bed build, as built, gauge area	47±1.79
Heated bed build, cut condition, fractured, holding area	53.24±2.27
Heated bed build, cut condition, fractured, gauge area	55.46±2.68
Heated bed build, polished, fractured, holding area	54.25±4.69
Heated bed build, polished, fractured, gauge area	59.22±1.67
Room temperature build, as built, holding area	54.57±2.08
Room temperature build, as built, gauge area	54.15±2.50
Room temperature build, polished, fractured, holding area	61.75±7.38
Room temperature build, polished, fractured, gauge area	66.69±2.43

In this study, any form of surface or structural modification resulted in an increase in martensite phase fraction. Interestingly, almost the same amount of austenite transformed during the tensile testing of both room temperature and heated bed built M300, indicating that building at an escalated temperature did not alter the deformation behaviour of M300. In addition to the deformation induced martensitic transformation, surface polishing has also resulted in martensitic transformation. While 7.18% austenite was transformed to martensite purely through polishing the holding area surface of room temperature built sample, a much smaller fraction of 0.63% was introduced in the holding area of heated bed built specimen, indicating a difference in the metastability of austenite in these two samples. An additional 7.39% of martensite was found at the gauge area of room temperature built tensile bar prior to tensile testing. This is in good agreement with the 7.47% difference between the polished and fractured samples. It is thus speculated that around 7.5% of austenite transformed purely due to the thermal stress and strain associated with the L-PBF process. To demonstrate the influence of abrasion, XRD spectra were taken before and after surface grinding with the same sample, as illustrated in Fig 5.10. As-built M300 exhibits a dual phase microstructure. After surface grinding with grit paper, γ peak disappears and a significant increase in the intensity of α' can be seen.

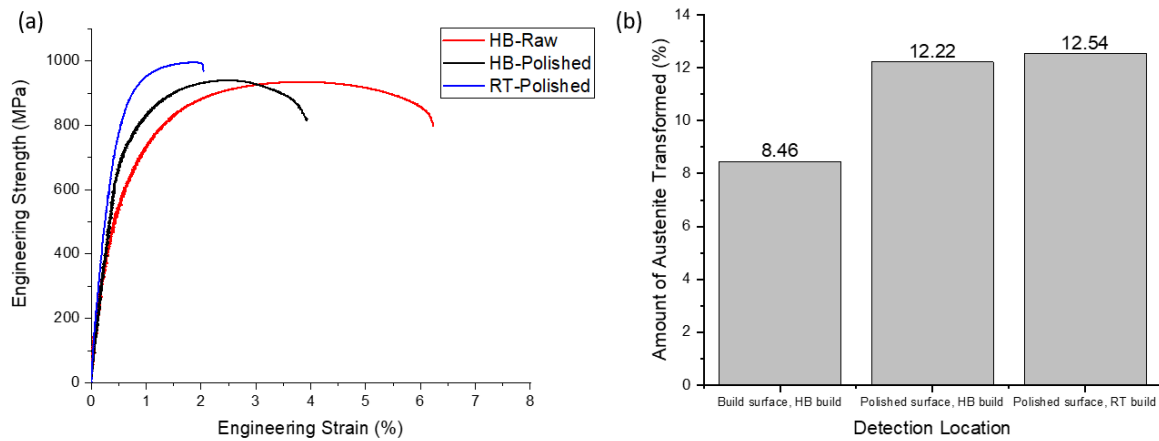


Figure 5.9: (a) Engineering stress/strain curve of room temperature and HB built M300 steel. Lower yield and tensile strengths are registered by the HB built specimens. (b) Transformation of austenite during tensile testing.

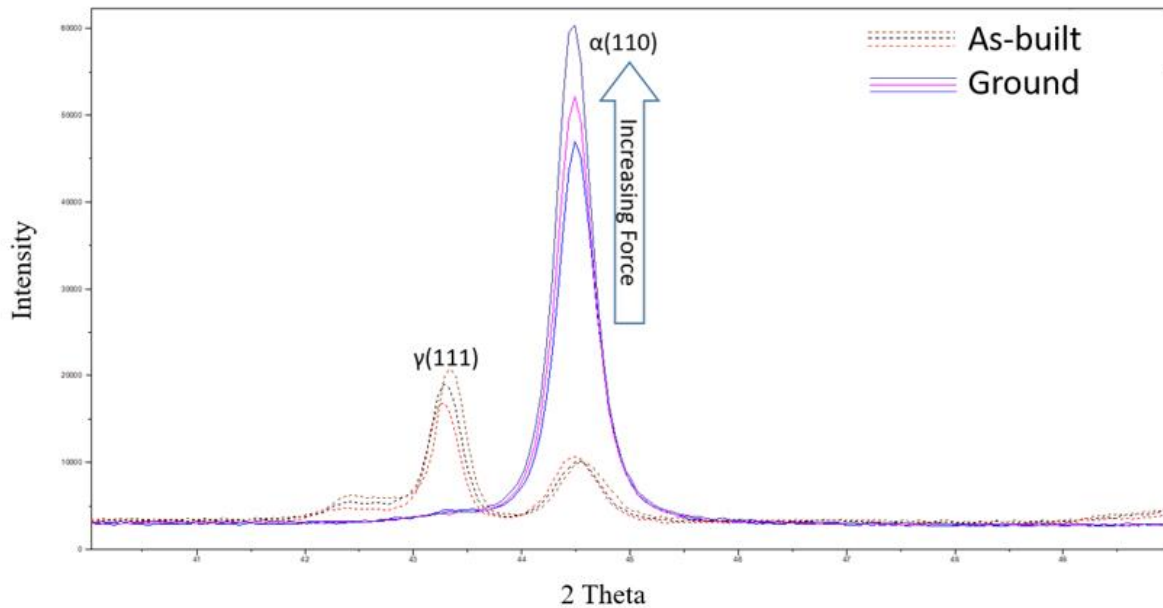


Figure 5.10: Combined XRD spectrums of ex-situ study of the effect of surface abrasion.

5.6. Discussion

5.6.1. Phase constitution of additive manufactured M300 maraging steel

A higher than usual austenite volume fraction in M300 is demonstrated in the present study, which primarily attributes to the crescent shaped austenite band obtained at room temperature. Allam et al. investigated the possibility of manipulating phase fraction with post-build heat treatments [88]. A thin slice of austenite was successfully reverted by a combination of solution and ageing heat treatments. What's interesting is that this slice of reverted austenite is situated between two melt-pool boundaries. Conde et al. studied the effect of ageing heat treatment carried out at different temperatures [86]. Extra stability of austenite was gained in samples

aged below 690°C. The recovery of austenite can be separated into diffusional and displacive [89]. While diffusional transformation is strongly dependent on the heat treatment temperature and mobility of atoms, displacive transformation is more dependent on the heating rate. In the cases of heat treatment applied to as-built parts, holding between Ac1 and Ac3 temperature enabled slow diffusion to occur and eventually forming austenite with sufficient nickel content and stability that does not undergo transformation during metallurgical preparation [86]. This is more desirable compared to applying solution treatment or using higher ageing temperature, as dissolution of cell boundaries lead to martensitic transformation to occur and lower fraction of retained austenite will be obtained [88].

In comparison, the austenite crescents obtained in the present study were purely formed by processing induced *in-situ* heat treatment, namely a combination of tighter hatch spacing and higher energy density (117%). The effect of 30µm hatch overlap is shown in Fig 5.11.

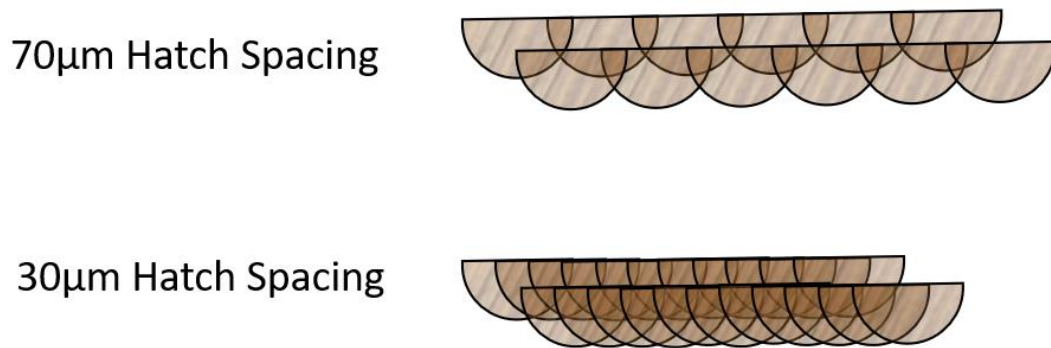


Figure 5.11: Drawings demonstrating the influence of hatch spacing. The volume of weld track overlap and consequent heat affected zone is much bigger in the scan strategy with 30µm hatch spacing.

It is obvious that with a tighter hatch spacing, larger areas are remelted on every layer and the previous layer will also receive more intense *in-situ* heat treatment. In addition, the keyhole shaped melt pool also contributes to deeper range of melting, as depicted in Fig 5.14. In comparison to conduction mode melt pools, keyhole shaped melt pools have significant advantage in the penetration depth and a good vertical heat affected zone. With correct spacing, a much larger area of the previous layers can be heat treated. Nevertheless, due to the keyhole type defects illustrated in Fig 5.1, it is suggested that build-quality orientated parameter optimisation must be carried out to minimise the volume of defects while providing sufficient overlap to promote the retention of austenite. The engineering stress-strain curve in Fig 5.10 shows that while a good yield strength was reached, premature fracture occurred due to the

population of defects. To preserve a good ductility in the as-built M300, processing parameter should be adjusted to minimise the occurrence of keyhole related porosities. This optimisation process can be carried out using processing maps such as Fig 2.9 where the fraction of retained austenite and defect population can be plotted in addition to energy densities and keyhole shapes.

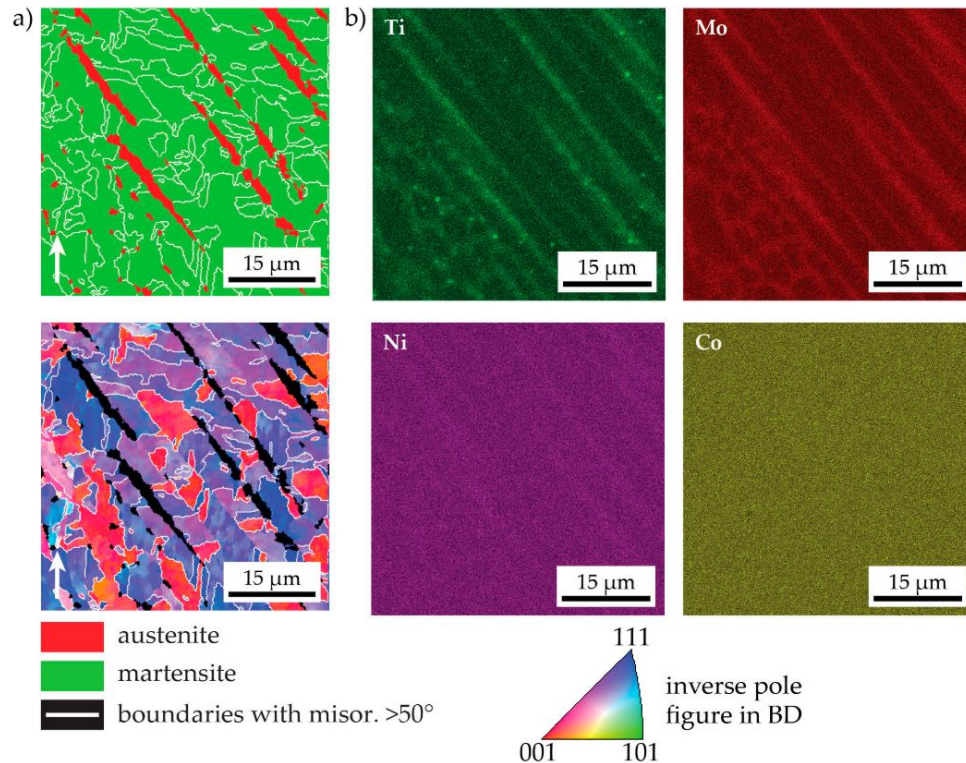


Figure 5.12:a) EBSD phase map and IPF map of LMD-built M300 maraging steel, FCC austenite is coloured in red and BCC martensite is coloured in green. b) Elemental segregation maps showing clear segregation of Ti, Mo and Ni at cell boundaries. The location of the segregation site matches to the location where austenite phase is indexed in a) [90].

Further to the apparent difference in melt-pool overlap scenario, this scan strategy may have influenced the segregation profile which strongly affects phase stability. It is commonly reported that as-built M300 displays weak Ti, Mo and Ni segregation at cell boundaries. As depicted in Fig 5.12, Jagle et al. demonstrated that bands of retained austenite are stabilised by strong presence of Ti, Mo and Ni at interdendritic regions of LMD-built M300 [90]. In comparison to SLM, LMD has a slower moving heat source and a much smaller cooling rate, which enabled sufficient time to allow partitioning of austenite-forming elements. Therefore, it is possible that enhanced in-situ heat treatment associated with the scan strategy utilised in the present study could have led to an enlarged area of retained austenite that exhibits higher percentage of Ni. Interestingly, this crescent shaped phase band is not exclusive to M300. As

shown in Fig 5.13, Köhnen et al. have illustrated a melt-pool shaped structure in additively manufactured high manganese steel [81]. It is suggested that this structure is mainly caused by the dissimilar solidification rate experienced by two parts of a melt-pool, where solute rejection takes place in the high solidification rate region and results in the formation of BCC phase [91][92]. In the present study, a similar situation may have taken place due to the keyhole mode melt-pools though further inspection of the chemical distribution near the crescent shaped-austenite is needed to confirm the exact segregated elements and their role in stabilising the austenite bands.

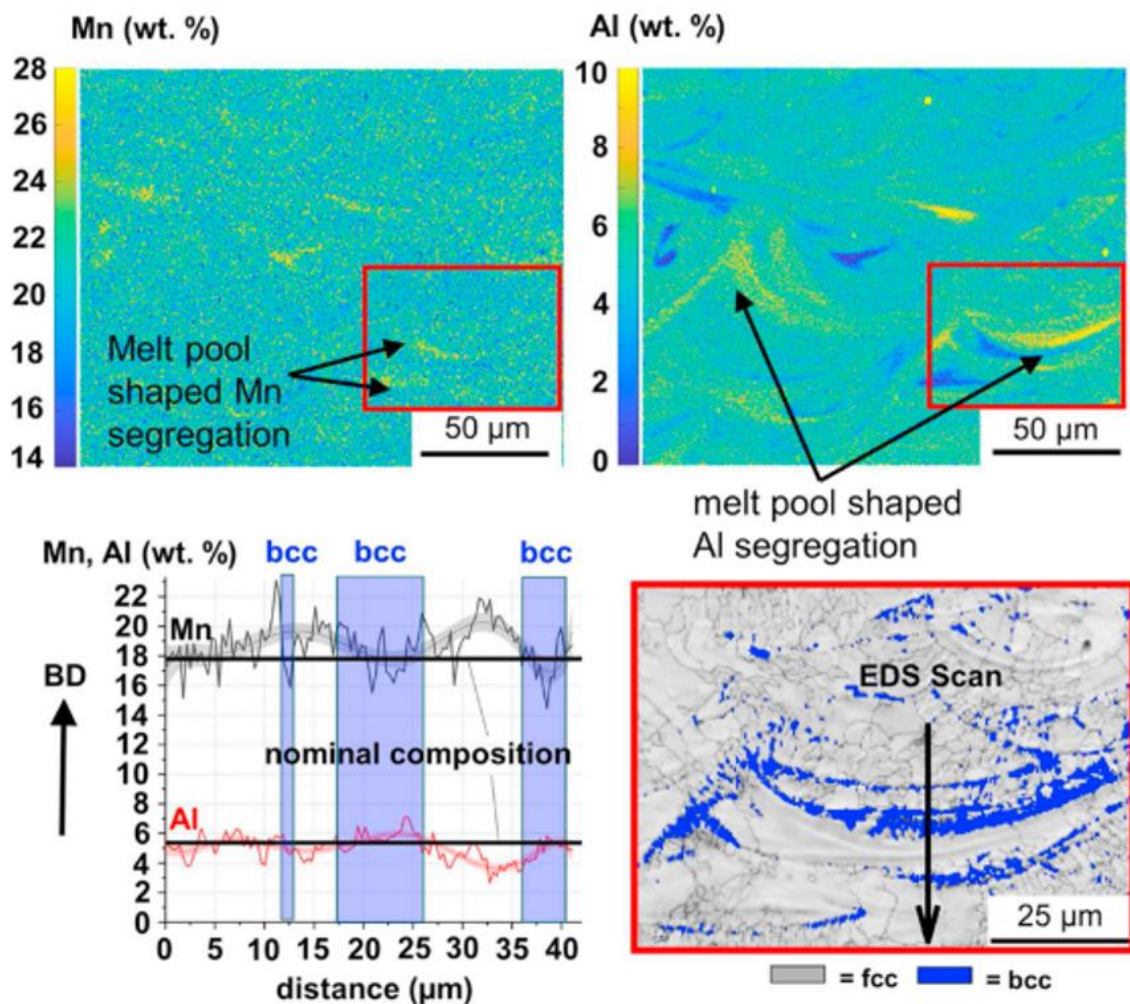


Figure 5.13: EDS maps of additively manufactured Fe-Mn-Al-C steel showing clear presence of band-like structures. EDS Line analysis shows coupled depletion of Mn and enrichment of Al in BCC phase areas, with corresponding EBSD phase map showing the location of measurement area [81].

Ageing heat treatment of M300 at 600°C shows that reverted austenite is stable enough to not undergo martensitic transformation even with partially dissolved cell boundaries. EDS analysis shows a distinct partitioning of nickel, which stabilises the austenite phase. In some regions up

to 3 wt.% difference in Ni content was indexed. This shows the amount of nickel needed to stabilise austenite through the microscopy preparation process and thus explaining why previous experimental works show a very “martensitic” microstructure of M300.

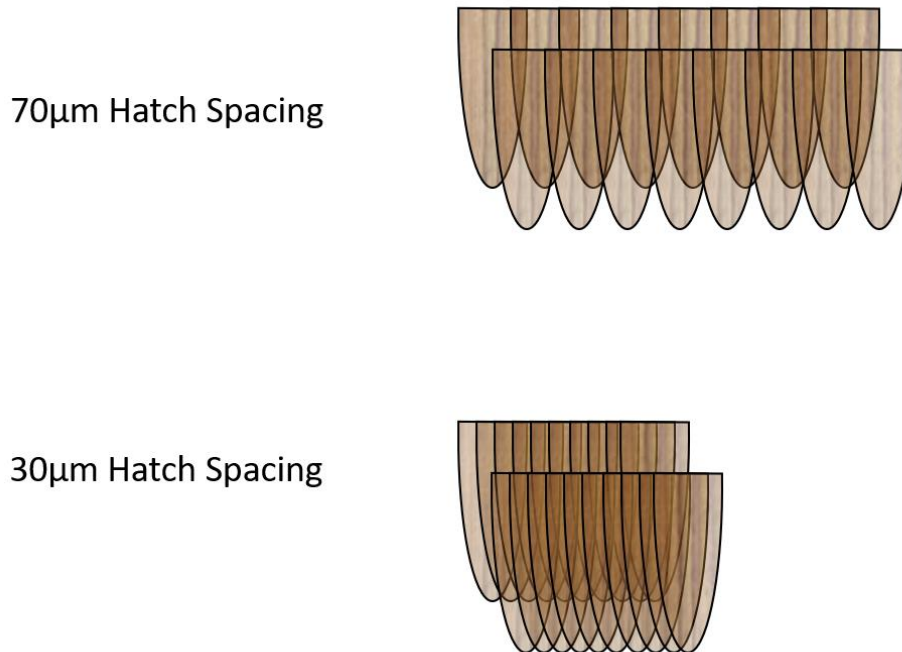


Figure 5.14: Schematic drawing of the effect of keyhole type melt pool. Not only does the melt pool penetrate further into the previous layer, the effect of 30µm hatch spacing is further magnified.

It is now established that nickel plays a key role in the stability of the austenite phase in additively manufactured M300. Apart from applying lengthy ageing heat treatment to additively manufactured M300, additional retained austenite can also be stabilised with keyhole type melt pools. The two methods of stabilising austenite are shown in Fig 5.15.

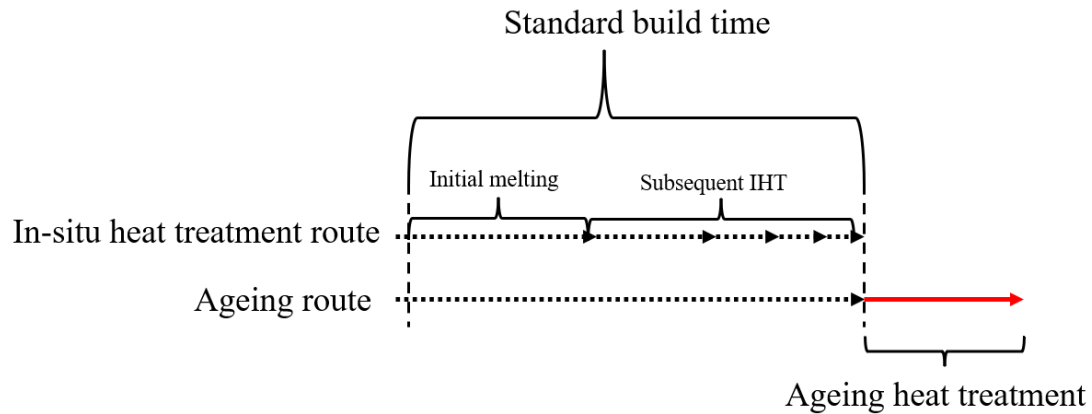


Figure 5.15: Two methods of obtaining additional austenite in additively manufactured M300. In-situ heat treatment route involves heat treating the sample through subsequent layers, whereas the ageing route revert austenite after the AM process.

5.6.2. Application of retained austenite as a damage sensor

Unlike neutron diffraction and magnetic testing techniques such as vibrating sample magnetometer which requires exact sample sizes, Feritscope can acquire readings from bulk, unaltered surfaces purely through magnetic induction method. Feritscope can also operate with materials containing multiple magnetic phases, as illustrated by Wang and Beese who conducted study on additively manufactured 304 stainless steel [7].

In the present study, Feritscope is the most critical evaluation equipment as it records the true microstructure phase fraction through a thickness rather than on a surface. During the abrasive & strain experiment, it can be seen that the retained austenite in as-built M300 has high sensitivity and transforms upon surface grounding with grit paper. Image analysis conducted on the EBSD phase map shows that less than 10% of austenite still exists after microscopy preparation, which includes steps such as cutting, grinding and polishing. Zarudi and Zhang investigated the machining induced microstructure evolution in quenchable metastable steel and the results showed that substantial phase transformation was induced by CNC machining [93]. Interestingly, the strain experienced by the test piece was most noticeable within the first 150 μ m depth, with its impact being fully negligible at 0.45mm. This explains the difference in martensite volume fraction obtained from Feritscope testing and EBSD image analysis, as Fertiscope readings are taken from a significant volume rather than the freshly prepared surface. In addition, Raghavan et al. conducted a systematic comparison between multiple means of measuring martensite content in a metastable austenitic steel deformed to different degrees [94]. As shown in Fig 5.16, the results suggest that an overestimation can be present in Fertiscope

results in comparison to methods such as X-Ray diffraction and neutron diffraction. This demonstrates that the discrepancy in the martensite volume fraction in the present study is not entirely AM-related. While the absolute variations in the phase fraction can be captured using the Feritscope, the values taken from as-built samples should be interpreted with care.

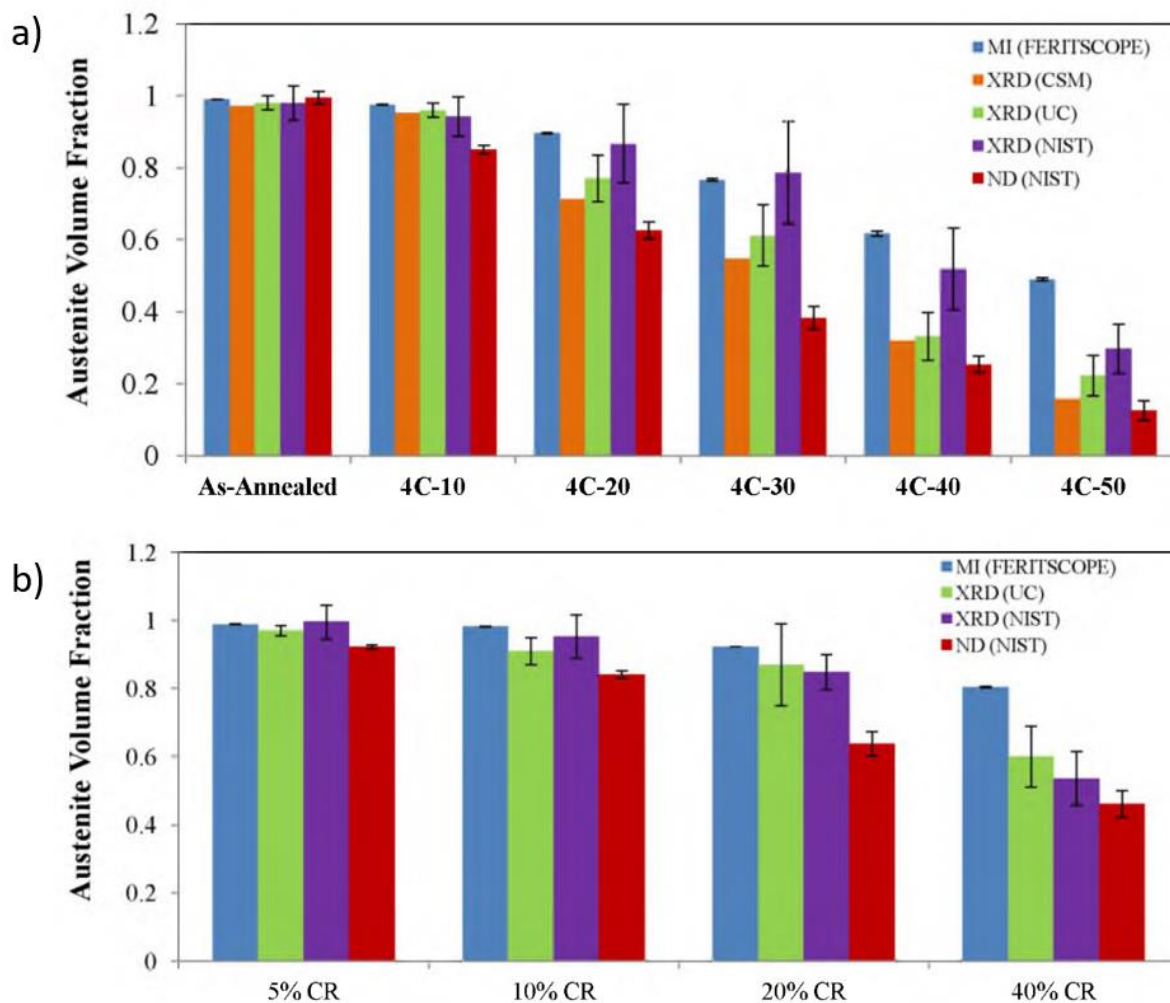


Figure 5.16: Remaining volume fraction of austenite in a deformed/rolled metastable austenitic steel obtained with magnetic induction, X-ray diffraction and neutron diffraction. a) shows the results of samples deformed to different engineering strain at 4°C. The results obtained in samples rolled to different levels of thickness reduction is illustrated in b) [94].

One can now suggest that there are three critical points that affect the final austenite volume fraction. Firstly, the chemistry of the steel will have the most dominant influence by affecting the martensite start temperature. Secondly, by metallurgically preparing the surface for electron microscopy study, a substantial fraction of austenite transforms to martensite on the surface. Moreover, since XRD also requires smoothing of the sample surface, a false identification will be confirmed in the XRD spectrum taken from the ground surface. Finally, as demonstrated in

this study, tensile testing of pre-ground samples has resulted in further reduction in the volume fraction of austenite, indicating TRIP behaviour is active during plastic deformation of M300. This entire sequence is illustrated in Fig 5.17.

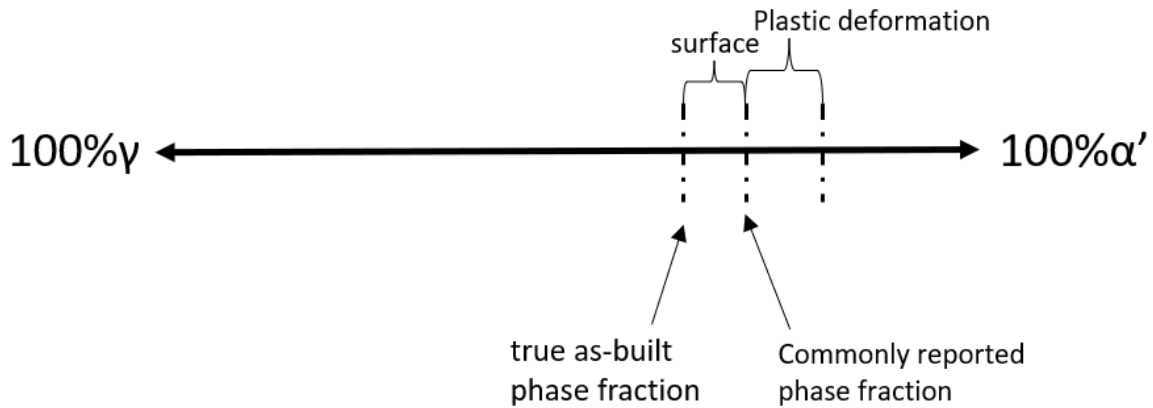


Figure 5.17: Analysis on the factors that influence the final volume fraction of martensite.

5.7. Conclusion

In summary, an additively manufactured M300 steel with higher volume fraction of austenite is presented. Feritscope characterisation on the bulk distribution of austenite and martensite revealed that about 7.5% austenite transformed purely due to the thermal stress during the AM process. Further studies of the microstructure shows that a dual-stage metastability was obtained in the M300 built with keyhole-inducing processing parameters. The following conclusions are drawn based on the experimental results

- As-built M300 possesses a dual phase microstructure with retained austenite situated in regions that are enriched in nickel.
- Depending on the local chemical composition, retained austenite can either undergo transformation upon surface preparation or remain stable.
- Keyhole type processing parameters can induce crescent shaped austenite bands during the build process through solute rejection phenomenon. These bands are stable during surface preparation.
- Nickel segregation plays an important role in stabilising and creating nucleation sites for retained and reverted austenite.
- While Feritscope readings indicate a significantly higher austenite content in the as-built M300 maraging steel, microscopy study suggests that less than 10% of retained austenite is present in the as-built material. Ageing at 600°C for 24 hours resulted in 13% total reverted austenite.

- A two-stage metastability was observed in the as-built M300. Stage one activates up on surface abrasion and up to 7.18 vol.% of austenite transformed in room temperature built sample. Upon straining, up to 8.46 vol% of austenite undergoes further transformation. Additional transformation may take place in samples with greater elongation to failure.
- Although Feritscope is suitable for investigating the TRIP effect in additively manufactured M300 maraging steel, the dramatic difference in the as-built austenite phase fraction obtained from Feritscope and other methods demonstrate that one should be mindful with the possible overestimation that is associate with the magnetic induction technique when quantifying phase fractions of metastable steels.
- The heated bed built sample has higher stability in retained austenite which resisted surface abrasion. Around 7.5 vol% of austenite difference was identified between room temperature built and heated bed built M300. The possibility of utilising this fraction of austenite for self-stress relief purposes will be investigated in the next chapter.
- The keyhole parameters used in the present study have resulted in regular appearance of keyhole porosities. Further optimisation to the processing parameters is required to achieve more desirable ductility values in the as-built tensile specimen.

6. Self Stress-Relief Capability in Additively Manufactured Steels

6.1. Background

So far, it is found that AM has the capability of levelling up yield strength in austenitic steels and enabling phase distribution control in martensitic steels. However, as the previous chapter has demonstrated, the phase fraction in additively manufactured M300 is also influenced by the processing condition. Due to the rapid heating-cooling nature of laser AM, the thermal stress and strain lead to the development of residual stress, magnifying the influence of AM defects such as gas porosity and solidification cracking which are detrimental to the plasticity and fatigue life of built parts. In certain cases, the magnitude of the residual stress can exceed the yield strength of the alloy and built parts must undergo stress-relief heat treatment with the substrate attached to prevent immediate cut-off distortion [20]. To circumvent post-build stress relief heat treatment and keep the manufacturing process as efficient as possible, it is therefore desirable for the alloy to possess stress-relief capability during the AM process.

Recently, zero or compressive residual stresses were characterised in steels welded with martensitic filler materials, which lead to a better fatigue performance [66]. This stress-relief phenomenon was attributed to the athermal martensitic transformation which occurred at a relatively low temperature (<300°C). Further studies of these low transformation temperature electrodes (LTTEs) suggested that the martensite start temperature (M_s) is critical for controlling the mode and magnitude of the residual stress. Some of the commercial steel powders available to the AM market happen to exhibit low transformation temperatures yet there have not been many studies mentioning the stress-relief capability of athermal martensite in additively manufactured steels. Most residual stress related works utilise X-ray diffraction and the peak shifts of crystalline planes to determine the magnitude of residual stresses. Lab based X-ray machines often have limited penetration thus the result is mainly acquired from the sample surface. In this study, a cantilever structure is selected to visually reveal the presence of residual stress present in the bulk form of additively manufactured transforming and non-transforming steels.

6.2. Scope of the study

To isolate mechanisms that may contribute to self stress-relief, three steels are selected and cantilever structures are fabricated to reveal the presence of AM residual stress. The transformation mechanisms of all three steels are illustrated in Fig 6.1.

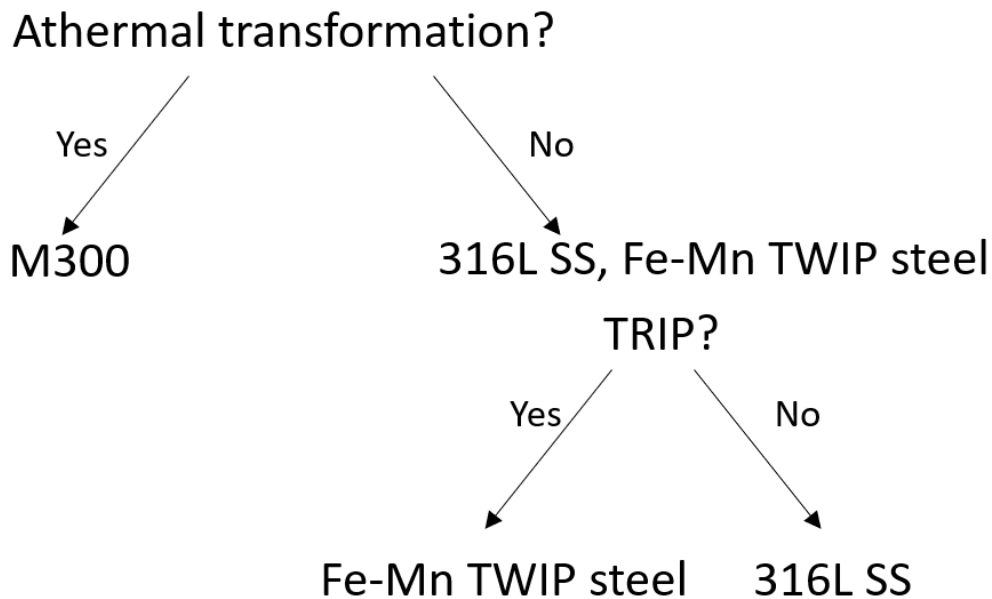


Figure 6.1: Alloy selection in the study based on where a steel can undergo athermal or deformation driven transformation.

Conventionally manufactured M300 has a martensite start temperature of 186°C [95]. Given that additively manufactured steels may exhibit lower martensite start temperatures compared to conventionally processed counterparts, a moderate level of stress-relief is expected in the cantilever structure [87]. 316L SS and Fe-Mn TWIP steels are fully austenitic as-built. Although high manganese TWIP steels may undergo γ - ϵ or γ - ϵ - α' transformation during plastic deformation, it is not clear whether this transformation can take place due to thermal strain. Therefore, the objectives of the present study are outlined:

- Fabrication of cantilever structure to confirm the presence of residual stress through cut-off distortion.
- Combined with characterisation results of both M300 and Fe-Mn TWIP steel in chapter 4 and 5, suggest the origin of self-stress-relief in additively manufactured steel and how steel compositions can be modified to enable this capability.

Numerical measurement of the residual stress in additively manufactured cantilevers will not be part of the objective. Instead, the angular distortion value due to cut-off will be used to evaluate the material's response to the residual stress.

6.3. Cantilever distortion in L-PBF built 316LSS and M300

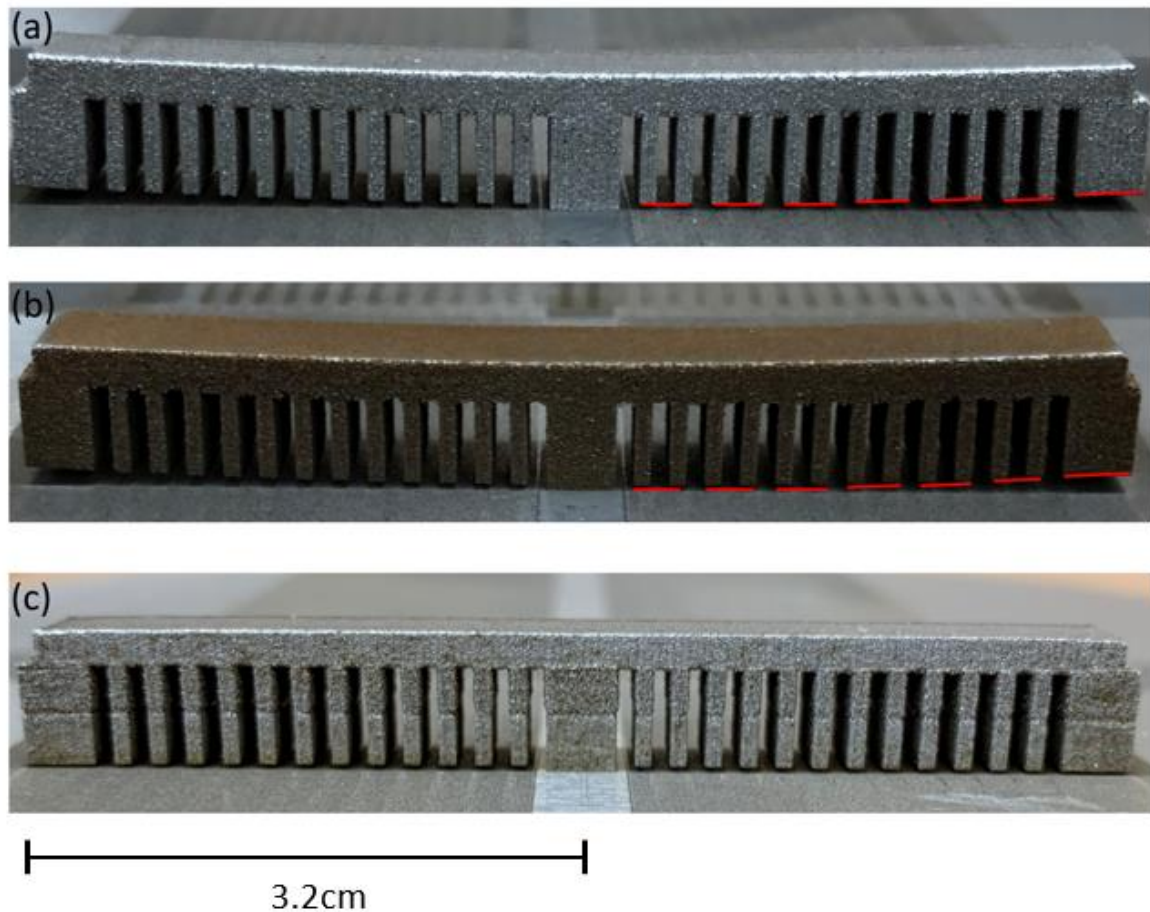
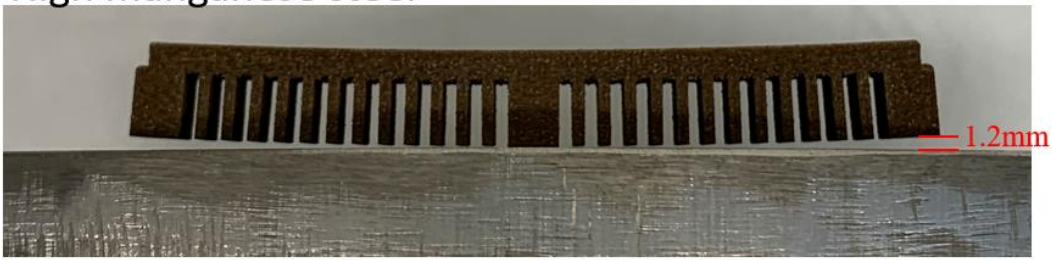


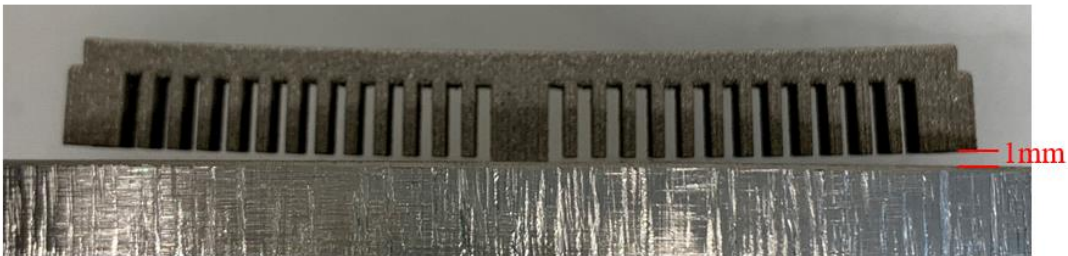
Figure 6.2: Cantilever structures built in (a) 316L stainless steel (b) Fe-Mn TWIP steel and (c) M300 maraging steel. Upward bending can be seen in cantilevers built with austenitic steels, whereas the M300 cantilever shows slight downwards bending.

Fig 6.2 and Fig 6.3 illustrate the direct comparison between the cantilevers built with three different steels. All three cantilevers show no distortion when fully attached to the baseplate. After cut-off, similar magnitudes of distortion can be seen in cantilevers printed in 316L SS and Fe-Mn steel, indicating a strong presence of tensile residual stress. In comparison, very negligible downwards bending was observed in M300 cantilevers which suggests that a compressive residual stress may be present in the structure. By measuring the distance between the bottom surface of the cantilever and the upper surface of the substrate, high manganese TWIP steel displays the highest level of distortion in the form of a 1.2mm gap. While 316L SS shows a very similar displacement value of 1mm, additively manufactured M300 achieved complete stress relief and no displacement is shown from the cantilever.

High manganese steel



316L SS



M300

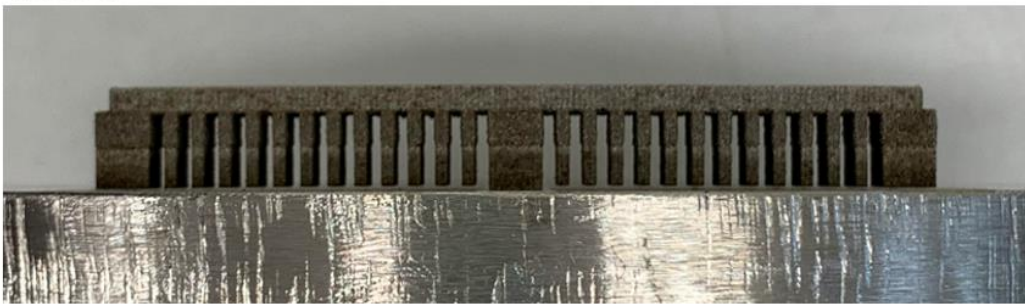


Figure 6.3: By measuring the gap of distortion, it can be seen that Fe-Mn TWIP steel displays the highest magnitude of distortion after cut-off. This is closely followed by 316L SS which shows a similar level of angular distortion. Meanwhile, the M300 shows no distortion.

The presence of a compressive residual stress is more pronounced in thinner slices of tensile specimens, as shown in Fig 6.4 where only the top build surface samples display downwards bending.

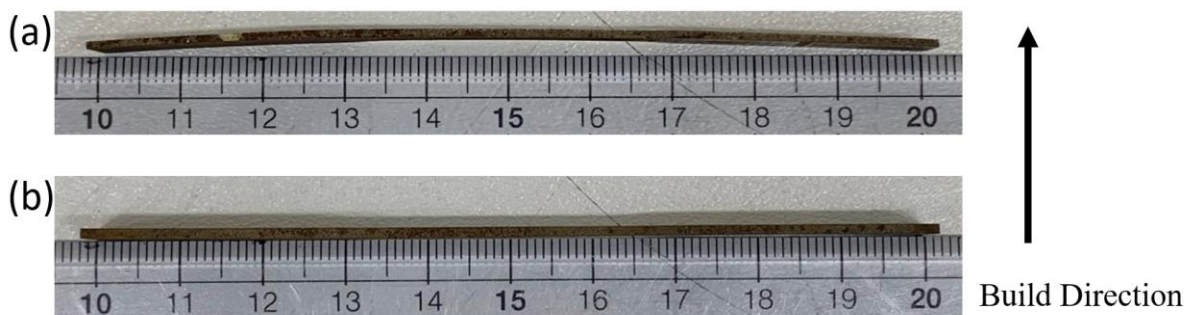


Figure 6.4: EDM sectioned M300 tensile bars. Significant distortion can be seen in (a) which is the top surface of the build part. Meanwhile, the tensile bar (b) sectioned below the build surface shows no distortion.

6.4. Dilatometry of as-built M300 maraging steel

The martensite start temperature was previously described to play an important role in the final stress level. In this study, dilatometry experiment was carried out on a cuboid sample and the result suggests that a M_s of 148.9°C was obtained with the present processing parameters. The heating and cooling graph is depicted in Fig 6.5.

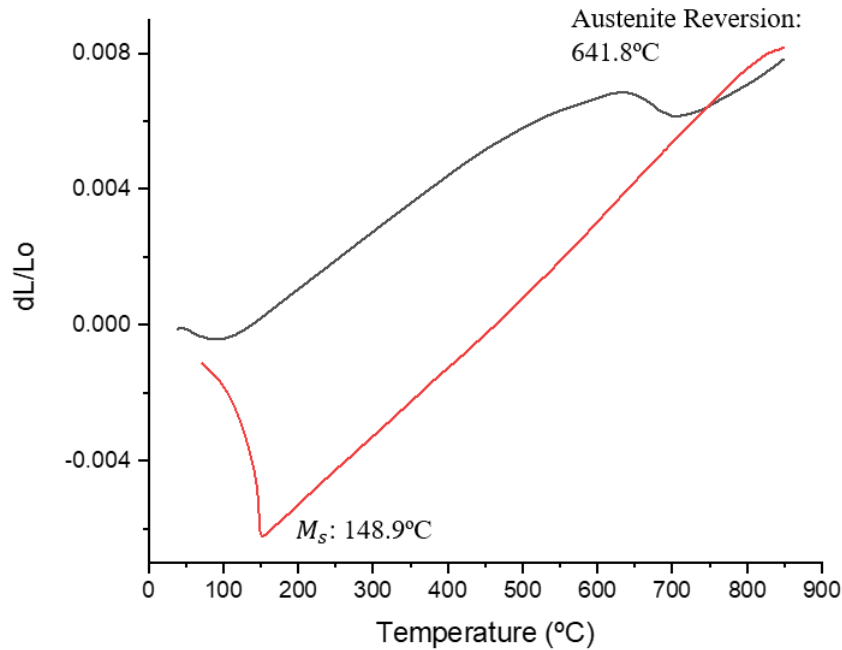


Figure 6.5: Displacement diagram showing the transitioning point during the heating and cooling of additively manufactured M300. The exact temperature of austenite reversion and martensite transformation are labelled.

During the heating process, the reversion of austenite can be seen at 641.8°C, as the graph shows an endothermic reaction. The martensitic transformation was observed at 148.9°C. This is lower than the predicted temperature made in chapter 3.

6.5. Validation of the self stress-relief effect

To further validate the stress-relief effect by showing that equal level of thermal strain was subject to all three cantilevers, the thermal strain associated with the AM process is estimated with a dimensionless strain term introduced by Mukherjee et al. [96]. The original model covers a wide range of materials and processing parameters such as volumetric change to heat input and heat input time. To fit the purpose of this study, a simplified version of this strain term utilised by Freeman et al. is used [50]. as shown in equation 6.1.

$$\varepsilon = \frac{Aw}{lh} \left[\frac{Q}{V} \right]^{3/2} \quad (6.1)$$

Where ϵ is the process driven thermal strain parameter, w represents the melt pool length and h stands for hatch spacing. The other terms such as sample area(A), second moment of inertia (I) laser power(Q) and scan speed(v) are assumed as 1 as the same processing parameters were used to manufacture the cantilevers. The 3D melt pool model is then used to generate melt pool length of all three compositions [71]. The shape and the lengths of the melt pools are demonstrated in Fig 6.6. Very small variations in melt pool length can be observed which largely attributes to the similarity in the thermal properties of these three steels. Fig 6.7 shows the influence of the strain term on the distortion level. Again, it can be seen that M300 clearly exhibits stress-relief behaviour as no distortion can be seen while subjected to the highest strain parameter value. In comparison, the positioning of Fe-Mn TWIP steel and 316L SS indicates that for non-transforming steels a higher thermal strain will lead to larger distortion scale. This is in agreement with the original work presented by Mukherjee et al. where a linear response between thermal strain and the strain parameter can be observed [96].

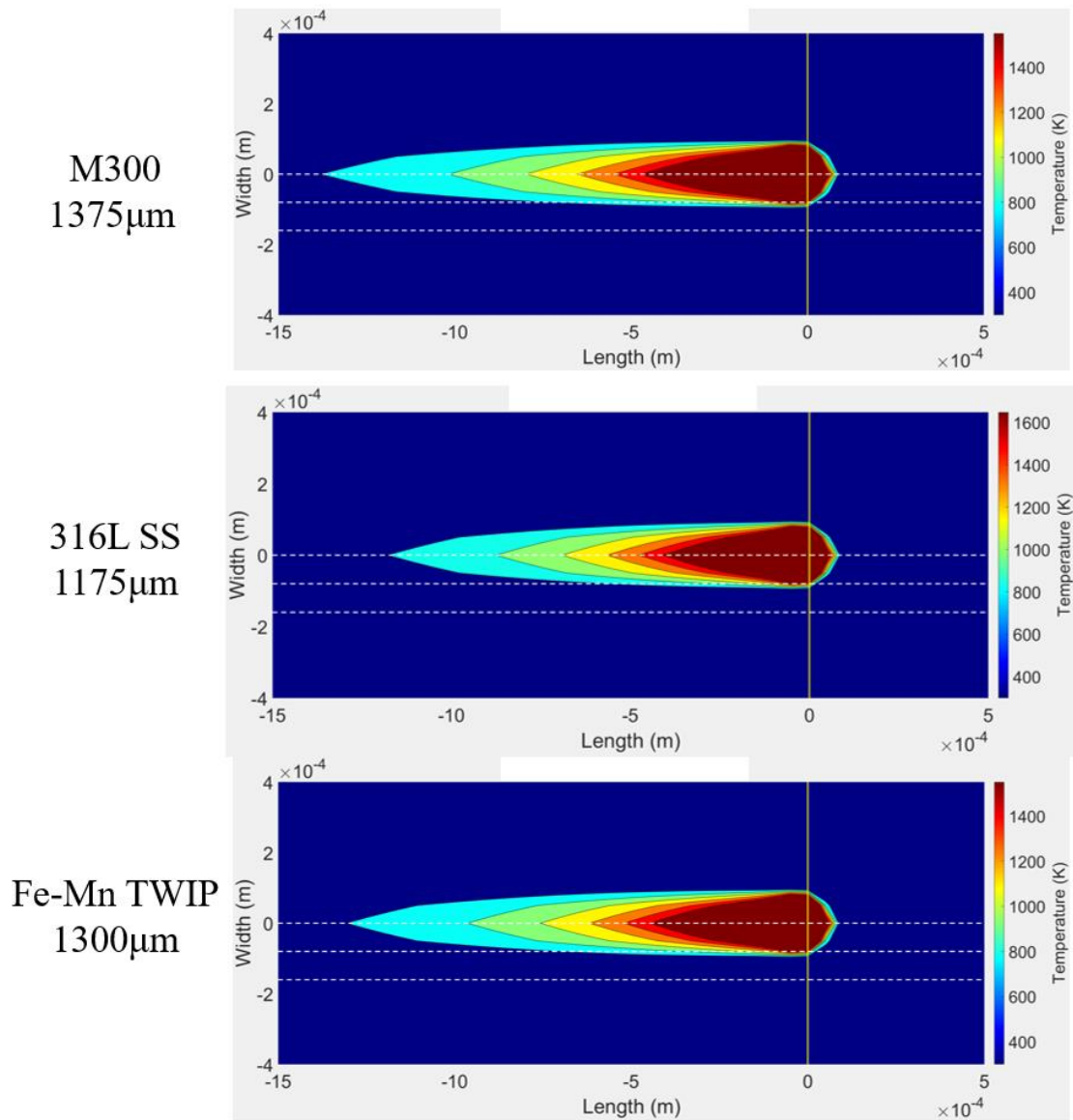


Figure 6.6: Melt pool length simulated with the Matlab script. Overall similar melt pool lengths are observed in all three steels.

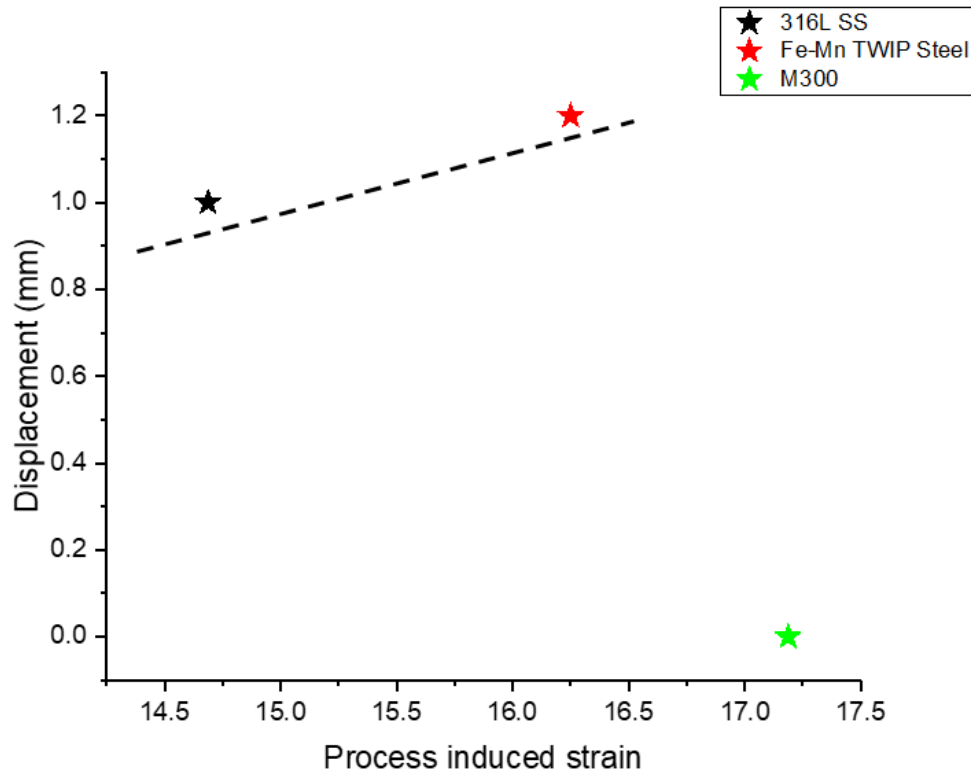


Figure 6.7: Relationship between thermal strain term and the cut-off distortion observed in cantilevers. While the austenitic steels exhibit large displacement due to the thermal strain, M300 shows no distortion due to its self stress-relief capability.

6.6. Discussion

Residual stress formation in laser additive manufactured parts can be influenced by processing parameters, substrate temperature, feedstock chemistry and the scan strategy. In this study, the same cantilever structure and processing parameters were used so that the comparison was made purely to compare the presence and mode of residual stress.

To start with, both austenitic steels exhibit moderate distortion after cut-off. Visual inspection of the cantilevers suggests that tensile residual stress is present in non-transforming steels while compressive residual stress is likely to exist in the transforming M300 maraging steel. The generic residual stress formation in additive manufacturing is covered in the literature review section. Li et al. studied the simulation of residual stresses using the cantilever structure [97]. With non-transforming steels, the top bar is subject to tensile residual stress prior to cut-off. As the support structure is being removed from the substrate, the top bar transitions to compressive stress to balance out the deformation to the supporting structure. This sequence resulted in the upward distortion observed in cantilevers built with 316L SS and Fe-Mn TWIP steel. The contrary can be expected with M300 as stress-relief takes place when the structure is cooled below martensitic start temperature and a near-zero residual stress is present in the top bar prior to cut-off.

The formation of annealing twins under the influence of residual stress is often observed in alloys with low stacking fault energy [98]. The boundary characteristics of 316L SS built in this study is shown in Appendix Fig 10. While certain processing parameters have been demonstrated to result in extremely high populations of $\Sigma 3$ boundaries, formation of annealing twins was not observed in the 316L SS built in this work [34]. Although Fe-Mn TWIP steel exhibits γ - ϵ martensitic transformation at substantial plastic strain, the low population of pre-existing twin boundaries resulted in limited nucleation site for the martensite phase thus the absence of stress-relief effect. The formation of ϵ -martensite is often observed in regions with high stacking fault and twin density [99]. For athermal martensitic transformation to occur, the Fe-Mn TWIP steel would need to be submerged in liquid nitrogen and reach a temperature of -125°C , as predicted in Table 3-1. Therefore, it can be concluded that with the structure and processing parameters employed in the present study, M300 maraging steel with athermal martensitic transformation at 150°C was the only one to successfully self stress-relief at room temperature.

As previously discussed in chapter 4 and 5, the martensite start temperature can be influenced by the dislocation cell size. A 30°C difference is obtained in the present study between the M_s of AM part and literature value of conventionally processed M300 [95]. However, Krol et al. reports M_s value of M300 in the range of 213°C to 221°C , significantly higher than that of this work [70]. The 100°C reduction in the M_s of 17-4PH reported by Freeman et al. also shows that the suppression of martensite start temperature is not universal different compositions [87]. In addition to the uncertainties in compositional response to the cell size suppression of martensitic transformation, the micro-level segregation due to processing parameters (cell boundary segregation) may also play an important role in influencing the degree of martensitic transformation. For instance, the scan strategy utilised in chapter 5 has much larger *in-situ* heat treatment effect which partially stabilised bands of retained austenite and less athermal martensite formed at room temperature. Therefore, it is difficult precisely predict the “AM” M_s value for a given composition. Nevertheless, with the work reported on direct application of LTTEs in LMD platforms, it can be suggested that alloys with low transformation is certainly capable of self stress-relief [100].

In addition, Freeman et al. conducted experiments around controlling phase fraction in 17-4PH with processing parameters using the same strain term and increments in martensite fraction was found when the process driven thermal strain increases [50]. Given that with appropriate parameters additively manufactured 17-4PH can exhibit a fully austenitic microstructure, one

may argue that a unique TRIP stress relief phenomenon may be present in additively manufactured 17-4PH. However, further experimentations are required to validate this as the build surface of high thermal strain 17-4PH is rough and may not be applicable to ordinary processing conditions, as shown in Fig 6.8. In other words, the amount of thermal strain required to activate the TRIP stress-relief effect may exceed the critical point where the build quality is compromised.

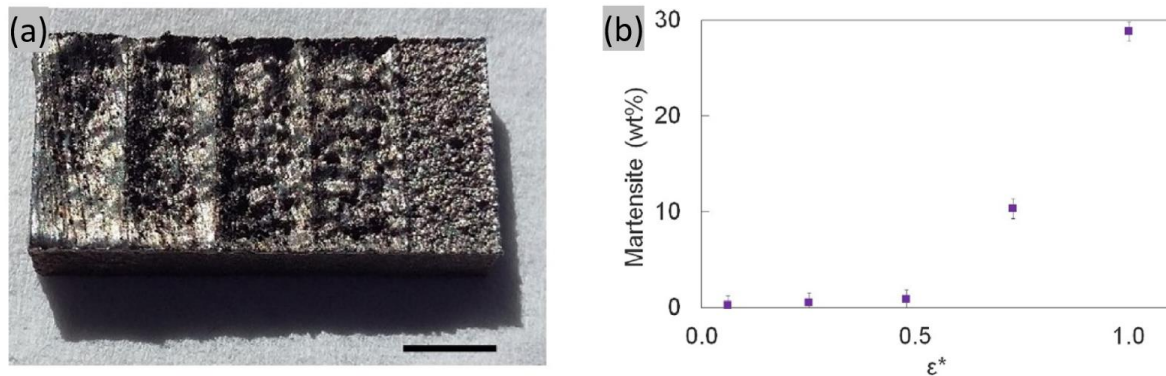


Figure 6.8: (a) Spatially graded 17-4PH showing rough surface in the high thermal strain region (austenite + martensite) and smooth surface in low thermal strain region (fully austenitic) (b) Relationship between the weight percent of martensite and the process driven thermal strain term [50].

The effect of residual stress on the mechanical performance of additively manufactured 316L SS was studied by Chen et al., which highlighted how the heterogeneous microstructure contributed to the formation of residual stresses [32]. In scenarios where it is not possible to introduce martensitic transformation by alternating the powder chemistry, it is recommended that stress-relief heat treatment or substrate preheating should be applied to additive manufactured non-transforming steels.

6.7. Conclusion

In summary, the effect of self stress-relief capability of steels with low martensitic transformation temperature is illustrated with cantilevers built with 316L SS, high manganese TWIP steel and M300 maraging steel. While a clear tensile residual stress induced upwards bending was observed in cantilevers built with non-transforming steels, negligible distortion could be found in the cantilever built with M300. Using a simplified strain model, it was discovered that all three cantilevers were subject to a similar level of thermal strain. The present study shows that steels with low transformation temperature can accommodate thermally induced residual stress with displacive transformation occurring at the temperature range where thermal contraction takes place. For future study of introducing low transformation temperature

steels into AM, it is recommended to anticipate a large variation in martensite start temperature before and after the AM process. The activation of the TRIP effect in the Fe-Mn TWIP steel is dependent on previous deformation products such as deformation twin, which led to insignificant stress-relief effect. The cantilever structure utilised in the present study has shown effectiveness in revealing the mode and magnitude of residual stress through cut-off angular distortion. For low-cost destructive testing where the numerical value of residual stress is not required, such structural components should be considered.

7. Conclusion

7.1. Summary of the study

Based on the success of additive manufacturing of 316L stainless steel, the present study conducted around the hierarchical microstructure and its influence on the microstructure, mechanical properties, and phase stability of additively manufactured steels. The design of a high manganese twinning induced plasticity steel and its application in L-PBF platform shows that powder based AM has the capability of adopting alloys with poor weldability. A trade-off between yield strength and ductility occurred due to the heterogeneous microstructure and process induced defects. The study in metastable M300 maraging steel highlighted the role of solute elements in the phase fraction and stability of retained austenite. Further study of the prototyping of a cantilever structure have shown the unique stress-relief capability of M300 which is similar to that of low transformation temperature electrodes. These three chapters have provided insights into designing new alloys for laser AM in terms of the influence of AM-specific microstructure and AM-induced segregation. It is also suggested that alloys with displacive transformation taking place at low temperature can self stress-relief in an additive manufacturing condition. Main conclusions of this thesis are listed as following:

Application of a high manganese steel for L-PBF platforms

- Fe-18Mn-2Al-0.5Si-0.3C TWIP&TRIP steel exhibits a good combination of strength and ductility when subject to cold rolling and annealing. A low yield strength is present due to the non-refined grain size.
- Microstructure investigation shows that twinning and γ - ϵ - α' transformation were observed as the main deformation mechanism. Both mechanisms contributed to an elongation to failure above 60%.
- A high initial strain hardening rate of 2931MPa and the slow decline in strain hardening rate resulted in a UTS of 873 MPa. Multi-stage work hardening can be observed.
- Despite showing solidification crack during single laser hatch track testing, the proposed composition has a large processing window in a L-PBF platform.
- A fully austenitic microstructure was obtained, with elongated grains of high aspect ratio and nanometre sized solidification cells.
- Micro segregation of manganese and silicon was discovered at cell boundaries. Unlike conventionally processed TWIP steels, the deformation was not altered at interfaces with segregation.

- Tensile testing shows a 243 MPa increment in yield strength. However, reduction in elongation to failure was also observed, with negligible decrease in the UTS.
- Microscopy study of intermediate strained samples show that twinning is the predominant deformation mechanism at 25% plastic strain, with small volume of γ - ϵ transformation occurring at heavily twinned regions. As HCP intensities did not appear in XRD spectrums of intermediate strained samples the transformation could be local and small in volume.
- While literature suggests that cell boundaries can provide resistance to dislocation glide on deformation twins. The growth of the deformation twin through a high aspect ratio grain was unaltered by the dislocation network. This results in a reduced twin density and thus a rapidly declining strain hardening rate.
- Overall, the combined tensile properties of additively manufactured TWIP steel are inferior when compared to its conventionally processed counterpart. This is mainly due to the reduction in elongation to failure, which is attributed to both the absence of γ - ϵ - α' transformation and the presence of micro-scale porosities.
- With regards to the alloy design aspects, the proposed TWIP steel did not suffer from weldability issues associated with the carbon addition. This is largely attributed to the unique characteristics of the AM process, which involves substantial remelt of the previous layer and high cooling rate. The more uniform distribution of manganese micro-segregation has also resulted in the absence of large scale γ - ϵ - α' transformation.
- Conventional welding diagrams can still be used to estimate the phase constitution. Future work on design alloy for AM should incorporate more details of the AM-characteristic microstructure and segregation profile.

Metastable austenite in an additively manufactured martensitic steel

- Additively manufactured M300 exhibits a dual phase microstructure. As-built M300 with keyhole processing parameter have resulted in additional crescent shaped retained austenite.
- Feritscope readings taken before and after surface abrasion indicate that martensitic transformation indeed took place purely due to grinding with grit paper. XRD spectra conducted ex-situ shows depletion of austenite in the abraded surface.

- Ageing heat treatment of M300 shows that up to 15 vol% of austenite can be reverted in 50 minutes of holding at 600°C. Further holding leads to partitioning of nickel into islands of cells where austenite can revert and remain stable after surface preparation.
- EDS mapping of as built and heat treated M300 shows a significant difference in segregation profile. Titanium segregation is enabled by both the high mobility of titanium and the *in-situ* heat treatment during the AM process. The enrichment of nickel in austenite cells occurs when ageing is carried out between Ac1 and Ac3 temperatures.
- Tensile testing of M300 built at room and escalated temperature reveals a dual stage metastability of retained austenite in additively manufactured M300. Similar fractions of martensitic transformation were measured by Feritscope during surface abrasion and tensile testing to a small amount of strain.
- Fabricating M300 at an escalated temperature did not induce significant precipitation hardening. The much smaller volume of martensitic transformation obtained by surface modification is likely due to the combined effort of *in-situ* heat treatment and ambient temperature induced slow diffusion.
- A smaller as-built martensite fraction was characterised in the gauge area of heated bed built M300, indicating that up to 7.5 Vol% of martensite can be induced by the thermal stress & strain associated with the build process.
- The significant difference between the austenite phase fraction calculated from image processing and Feritscope measurements shows that magnetic induction measurement is associated with overestimation. Extra care should be taken when preparing additively manufactured steels, where methods such as electropolishing should be considered to remove a mechanically worked surface.
- It is speculated that the crescent shaped austenite bands are formed by a strong solute rejection effect that resulted in heavy segregation of austenite stabilisers in the bottom of the melt pools. Further on-site EDS analysis is needed to determine the exact mechanism that stabilises these austenite bands.
- While the keyhole-shaped melt-pools have resulted in extra retained austenite at room temperature, it is worthwhile mentioning that a substantial amount of keyhole defects is generated as bi-product. Further optimisation of the processing parameter is needed for utilising this technique at lower cost of mechanical performance.

Self-stress relief capability of additively manufactured M300 steel

- Cantilever structures built with 316L SS, high manganese TWIP steel and M300 show no signs of distortion prior to cut-off.
- After sectioning of the feet, upwards bending can be seen in cantilevers built with 316L SS and high manganese TWIP steel, indicating the presence of tensile residual stress.
- The cantilever built with M300 however shows no significant bending. Sectioning of tensile specimen shows that a compressive residual stress is present in the top build surface of additively manufactured M300.
- The absence of annealing twins in additively manufactured 316L is processing parameter driven, as more recent studies have demonstrated the possibility of inducing a high population of CSL boundaries.
- All three cantilevers were subject to a similar level of thermal strain, based on the calculation of a simplified AM thermal strain model. This confirms that M300 responded different to the thermally induced residual stress.
- Large variations in M_s are currently being observed with laser AM. However, steels with substantial athermal martensitic transformation taking place at low temperature will exhibit stress-relief capability.
- The cantilever structure can be used to reveal the presence and the mode of residual stresses in additively manufactured parts. For precise measurement of the magnitude of residual stress, advanced characterisation techniques such as synchrotron and neutron diffraction should be considered.

7.2. Future work

7.2.1. Further improvement to the currently proposed high manganese TWIP steel

In the present study, the strengthening effect observed in L-PBF built 316L was successfully applied to the high manganese composition where low yield strength is its major weakness. However, a trade-off in ductility occurred and the overall crash worthiness of the TWIP steel became inferior when compared to its conventionally manufactured counterpart. The reduction in ductility can be attributed to the presence of micro and nano gas pores that were enlarged during straining. Microstructure analysis also indicates that the long aspect ratio grains may have led to a steady decline in the work hardening rate. Therefore, a post build treatment that closes gas pores and triggers partial recrystallisation should be applied to additively manufactured TWIP steel. Hot isostatic pressing (HIP) is the perfect candidate as literature shows its effect in both reducing porosity density and leading to recrystallisation, depicted in

Fig 7.1 and 7.2. However, the temperature and duration of HIP should be carefully controlled so that further coarsening of grains does not take place.

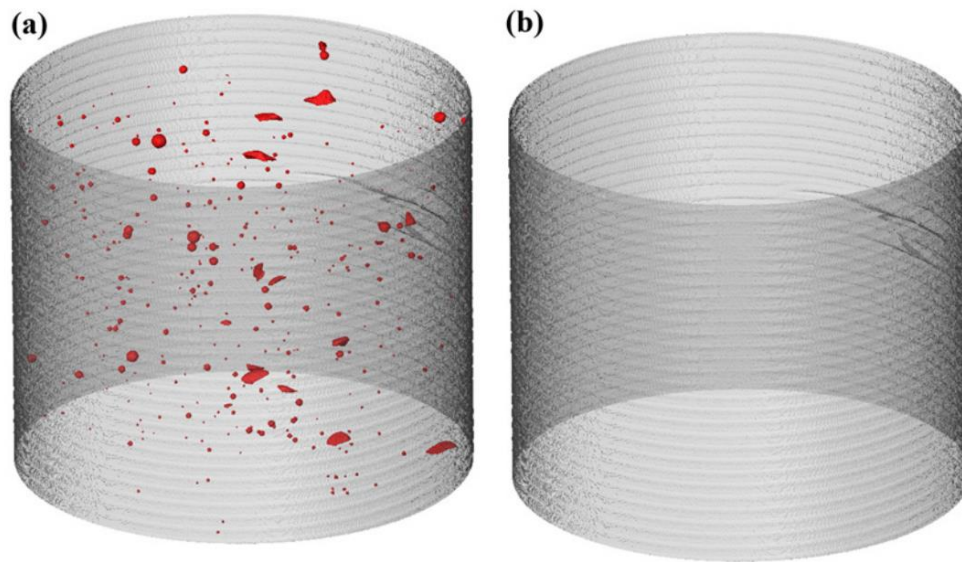


Figure 7.1: Effect of hot isostatic pressing on the defect volume of an additively manufactured part [13].

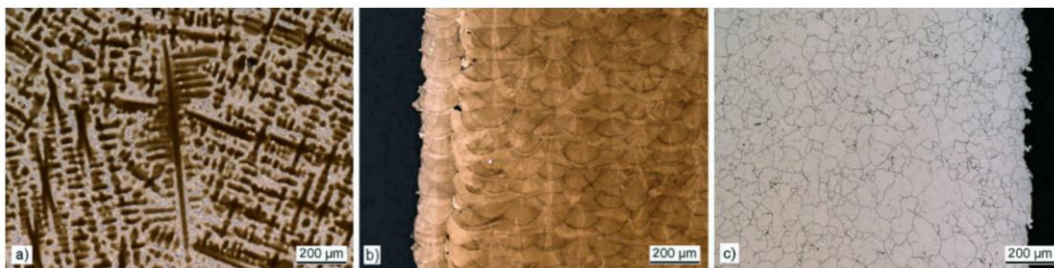


Figure 7.2: Microstructure of as-cast, additively manufactured and AM+HIP CoCrMo alloy [101].

7.2.2. Further understanding into the crescent shaped austenite bands

In the present study, a 2D understanding of the crescent shaped austenite is achieved. To have a better understanding of its formation and how this kind of structure can be reliably introduced into the microstructure, more advanced characterisation should be conducted. To investigate the interface between austenite and martensite, and the chemical profile around the interface, focused ion beam lift out can be carried out at the site of the crescent so that high resolution analytical transmission electron microscopy can be conducted on the exact γ - α' interface area. A schematic diagram of the area where FIB lift out should be carried out is presented in Fig 7.3.

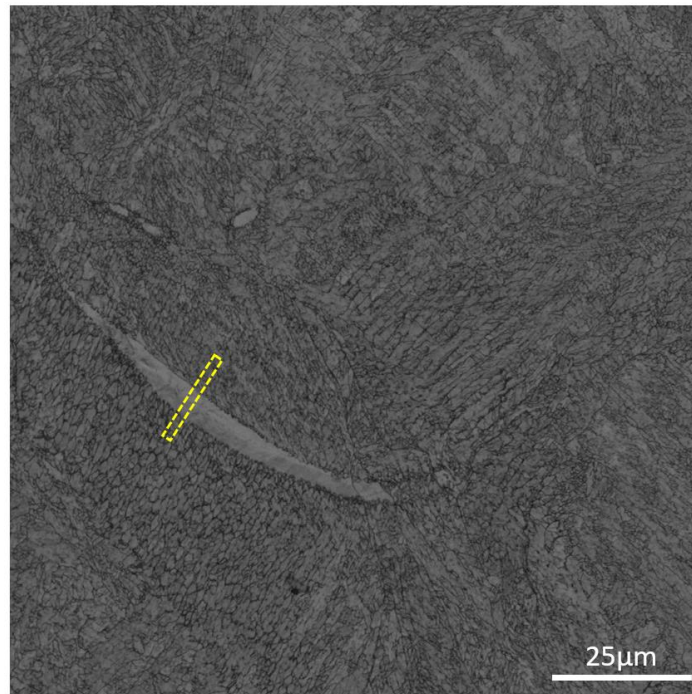


Figure 7.3: EBSD band contrast figure showing the location of the austenite crescent. FIB lift out position is highlighted in yellow.

7.2.3. *In-situ* observation of γ - α' - γ during the fabrication of M300 maraging steel

The present study showcased the depletion and recovery of austenite with *ex-situ* style characterisations. With the advancement in *in-situ* observation techniques, monitoring of phase transformation can be made with near-realistic processing conditions of additive manufacturing. Hocine et al. developed an experimental platform which enabled real-time monitoring of phase changes during the AM process, illustrated in Fig 7.4 [102]. Such platforms can be greatly beneficial to transforming metals in AM. In addition, more simplified experiments such as *in-situ* synchrotron XRD monitoring on the peak positions during surface abrasion and tensile straining should be carried out to confirm the readings taken with Feritscope.

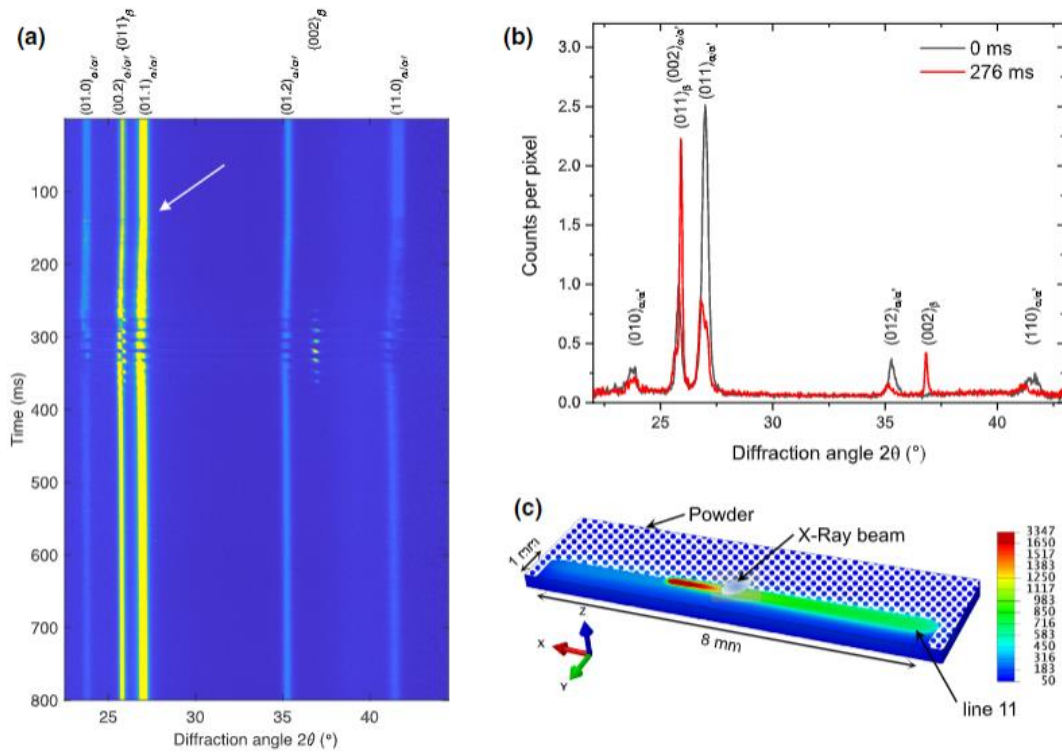


Figure 7.4: (a) variation of phase fraction shown in stacked intensities spectrum taken from the fabrication process of Ti-6Al-4V. (b) Individual spectrums taken before and after a laser hatch being laid. (c) Schematic diagram showing the relative positions of the melt pool, heat affected zone and the Synchrotron X-ray beam [102].

7.2.4. Realistic experiment on utilising M300 maraging steel as a structural sensor

Based on the discoveries of chapter 5, it is possible to clad M300 onto an engineering component as a structural sensor. Any form of surface abrasion, external stress or strain that exceeds the yield strength of the part can be monitored with non-destructive testing such as Feritscope measurements. The foundation has already been laid on this part of future work, where cuboids of different thickness were deposited onto the baseplate to a maximum height of 4mm. After sectioning tensile specimens out of the substrate with electrical discharging machining, the tensile bars formed by the stainless-steel substrate can be strained and the response of M300 can be recorded by the Feritscope. The geometry of the tensile specimen is shown in Fig 7.5.

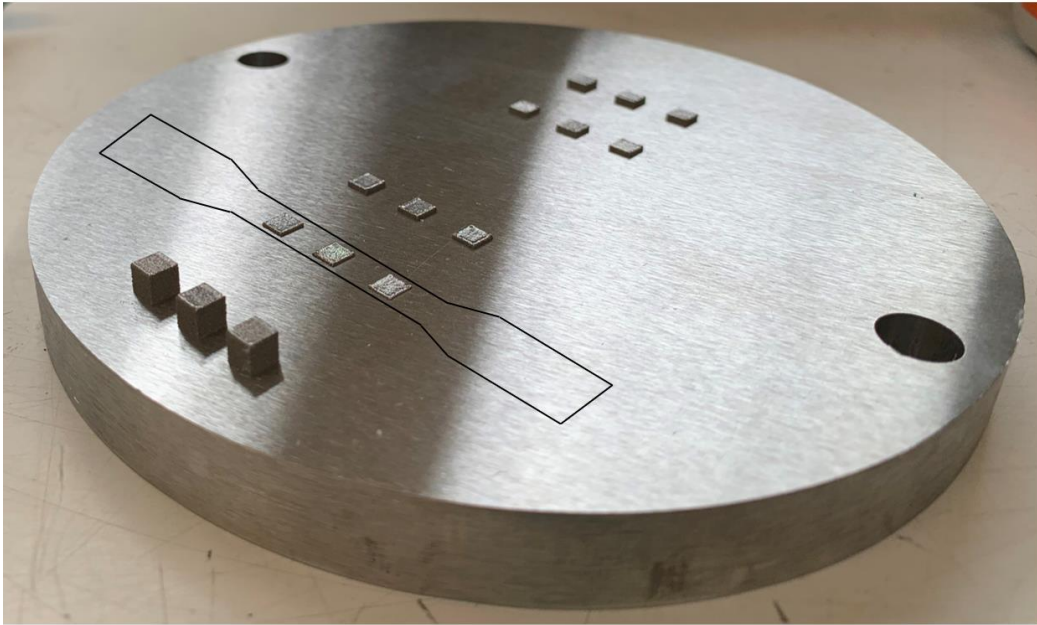


Figure 7.5: The M300 cladding deposited in Aconity Mini and the proposed shape of tensile specimen for sensor testing.

Reference

- [1] I. A. Segura, J. Mireles, D. Bermudez, C. A. Terrazas, L. E. Murr, K. Li, V. S. Y. Injeti, R. D. K. Misra, and R. B. Wicker, “Characterization and mechanical properties of clad stainless steel 316L with nuclear applications fabricated using electron beam melting,” *J. Nucl. Mater.*, vol. 507, pp. 164–176, 2018, doi: 10.1016/j.jnucmat.2018.04.026.
- [2] C. Wang, X. Tan, E. Liu, and S. B. Tor, “Process parameter optimization and mechanical properties for additively manufactured stainless steel 316L parts by selective electron beam melting,” *Mater. Des.*, vol. 147, pp. 157–166, 2018, doi: 10.1016/j.matdes.2018.03.035.
- [3] H. Knoll, S. Ocylok, A. Weisheit, H. Springer, E. Jäggle, and D. Raabe, “Combinatorial Alloy Design by Laser Additive Manufacturing,” *Steel Res. Int.*, vol. 88, no. 8, pp. 1–11, 2017, doi: 10.1002/srin.201600416.
- [4] H. Fayazfar, M. Salarian, A. Rogalsky, D. Sarker, P. Russo, V. Paserin, and E. Toyserkani, “A critical review of powder-based additive manufacturing of ferrous alloys: Process parameters, microstructure and mechanical properties,” *Mater. Des.*, vol. 144, pp. 98–128, 2018, doi: 10.1016/j.matdes.2018.02.018.
- [5] C. L. A. Leung, S. Marussi, R. C. Atwood, M. Towrie, P. J. Withers, and P. D. Lee, “In situ X-ray imaging of defect and molten pool dynamics in laser additive manufacturing,” *Nat. Commun.*, vol. 9, no. 1, pp. 1–9, 2018, doi: 10.1038/s41467-018-03734-7.
- [6] J. Jhabvala, E. Boillat, T. Antignac, and R. Glardon, “On the effect of scanning strategies in the selective laser melting process,” *Virtual Phys. Prototyp.*, vol. 5, no. 2, pp. 99–109, 2010, doi: 10.1080/17452751003688368.
- [7] Z. Wang and A. M. Beese, “Effect of chemistry on martensitic phase transformation kinetics and resulting properties of additively manufactured stainless steel,” *Acta Mater.*, vol. 131, pp. 410–422, 2017, doi: 10.1016/j.actamat.2017.04.022.
- [8] P. Lhuissier, X. Bataillon, C. Maestre, J. Sijobert, E. Cabrol, P. Bertrand, E. Boller, A. Rack, J. J. Blandin, L. Salvo, and G. Martin, “In situ 3D X-ray microtomography of laser-based powder-bed fusion (L-PBF)—A feasibility study,” *Addit. Manuf.*, vol. 34, no. December 2019, p. 101271, 2020, doi: 10.1016/j.addma.2020.101271.
- [9] J. Metelkova, Y. Kinds, K. Kempen, C. de Formanoir, A. Witvrouw, and B. Van Hooreweder, “On the influence of laser defocusing in Selective Laser Melting of 316L,” *Addit. Manuf.*, vol. 23, no. March 2019, pp. 161–169, 2018, doi: 10.1016/j.addma.2018.08.006.
- [10] R. Cunningham, C. Zhao, N. Parab, C. Kantzos, J. Pauza, K. Fezzaa, T. Sun, and A. D. Rollett, “Keyhole threshold and morphology in laser melting revealed by ultrahigh-speed x-ray imaging,” *Science (80-.)*, vol. 363, no. 6429, pp. 849–852, 2019, doi: 10.1126/science.aav4687.
- [11] Y. Chen, S. J. Clark, C. L. A. Leung, L. Sinclair, S. Marussi, M. P. Olbinado, E. Boller, A. Rack, I. Todd, and P. D. Lee, “In-situ Synchrotron imaging of keyhole mode multi-layer laser powder bed fusion additive manufacturing,” *Appl. Mater. Today*, vol. 20, p. 100650, 2020, doi: 10.1016/j.apmt.2020.100650.

- [12] M. W. Wu, J. K. Chen, B. H. Lin, and P. H. Chiang, “Improved fatigue endurance ratio of additive manufactured Ti-6Al-4V lattice by hot isostatic pressing,” *Mater. Des.*, vol. 134, pp. 163–170, 2017, doi: 10.1016/j.matdes.2017.08.048.
- [13] S. Tammam-Williams, P. J. Withers, I. Todd, and P. B. Prangnell, “Porosity regrowth during heat treatment of hot isostatically pressed additively manufactured titanium components,” *Scr. Mater.*, vol. 122, pp. 72–76, 2016, doi: 10.1016/j.scriptamat.2016.05.002.
- [14] Z. Gan, O. L. Kafka, N. Parab, C. Zhao, L. Fang, O. Heinonen, T. Sun, and W. K. Liu, “Universal scaling laws of keyhole stability and porosity in 3D printing of metals,” *Nat. Commun.*, vol. 12, no. 1, 2021, doi: 10.1038/s41467-021-22704-0.
- [15] L. Thijs, J. Van Humbeeck, K. Kempen, E. Yasa, J. Kruth, and M. Rombouts, “Investigation on the inclusions in maraging steel produced by Selective Laser Melting,” *Innov. Dev. Virtual Phys. Prototyp.*, pp. 297–304, 2011, doi: 10.1201/b11341-48.
- [16] Y. M. Wang, T. Voisin, J. T. McKeown, J. Ye, N. P. Calta, Z. Li, Z. Zeng, Y. Zhang, W. Chen, T. T. Roehling, R. T. Ott, M. K. Santala, P. J. Depond, M. J. Matthews, A. V. Hamza, and T. Zhu, “Additively manufactured hierarchical stainless steels with high strength and ductility,” *Nat. Mater.*, vol. 17, no. 1, pp. 63–70, 2018, doi: 10.1038/NMAT5021.
- [17] S. Bodziak, K. S. Al-Rubaie, L. D. Valentina, F. H. Lafratta, E. C. Santos, A. M. Zanatta, and Y. Chen, “Precipitation in 300 grade maraging steel built by selective laser melting: Aging at 510 °C for 2 h,” *Mater. Charact.*, vol. 151, no. September 2018, pp. 73–83, 2019, doi: 10.1016/j.matchar.2019.02.033.
- [18] M. Rappaz, A. Jacot, and W. J. Boettinger, “Last-stage solidification of alloys: Theoretical model of dendrite-arm and grain coalescence,” *Metall. Mater. Trans. A Phys. Metall. Mater. Sci.*, vol. 34 A, no. 3, pp. 467–479, 2003, doi: 10.1007/s11661-003-0083-3.
- [19] H. E. Sabzi, S. Maeng, X. Liang, M. Simonelli, N. T. Aboulkhair, and P. E. J. Rivera-Díaz-del-Castillo, “Controlling crack formation and porosity in laser powder bed fusion: Alloy design and process optimisation,” *Addit. Manuf.*, vol. 34, no. June, p. 101360, 2020, doi: 10.1016/j.addma.2020.101360.
- [20] Y. He, M. Zhong, J. Beuth, and B. Webler, “A study of microstructure and cracking behavior of H13 tool steel produced by laser powder bed fusion using single-tracks, multi-track pads, and 3D cubes,” *J. Mater. Process. Technol.*, vol. 286, no. June, p. 116802, 2020, doi: 10.1016/j.jmatprotec.2020.116802.
- [21] D. L. Olson, “Prediction of Austenitic Weld Metal Microstructure and Properties,” *AWS 65th Annu. Meet.*, pp. 280–295, 1984, doi: 10.1017/CBO9781107415324.004.
- [22] J. C. Lippold, “Solidification Behavior and Cracking Susceptibility of Pulsed-Laser Welds in Austenitic Stainless Steels A shift in solidification behavior under rapid solidification conditions promotes an increase in cracking susceptibility,” *Weld. J. Incl. Weld. Res. Suppl.*, vol. 73, no. 6, p. 129, 1994.
- [23] A. Zambon and F. Bonollo, “Rapid solidification in laser welding of stainless steels,” *Mater. Sci. Eng. A*, vol. 178, no. 1–2, pp. 203–207, 1994, doi: 10.1016/0921-5093(94)90544-4.

- [24] P. J. Withers and H. K. D. H. Bhadeshia, “Residual stress. Part 2 – Nature and origins,” *Mater. Sci. Technol.*, vol. 17, no. 4, pp. 366–375, 2001, doi: 10.1179/026708301101510087.
- [25] P. J. Withers and H. K. D. H. Bhadeshia, “Residual stress. Part 1—measurement techniques,” *Mater. Sci. Technol.*, vol. 17, no. April, pp. 355–365, 2001, doi: 10.1179/026708301101509980.
- [26] P. Mercelis and J. P. Kruth, “Residual stresses in selective laser sintering and selective laser melting,” *Rapid Prototyp. J.*, vol. 12, no. 5, pp. 254–265, 2006, doi: 10.1108/13552540610707013.
- [27] D. Buchbinder, W. Meiners, N. Pirch, K. Wissenbach, and J. Schrage, “Investigation on reducing distortion by preheating during manufacture of aluminum components using selective laser melting,” *J. Laser Appl.*, vol. 26, no. 1, p. 012004, 2014, doi: 10.2351/1.4828755.
- [28] Calphad, “Iron-Chromium Phase Diagram,” p. 1, 2000, [Online]. Available: <http://www.calphad.com/iron-chromium.html>
- [29] Calphad, “Iron-Manganese (Fe-Mn) Phase Diagram,” p. 2006, 2006.
- [30] The Materials Company, *ASM Handbook - Volume 3: Alloy Phase Diagrams*, vol. 3. 1992. doi: 10.1007/BF02869318.
- [31] H. K. D. H. Bhadeshia, *Bainite in Steels*, vol. 148.
- [32] W. Chen, T. Voisin, Y. Zhang, J. Florien, C. M. Spadaccini, D. L. McDowell, T. Zhu, and Y. M. Wang, “Microscale residual stresses in additively manufactured stainless steel,” *Nat. Commun.*, no. 2019, pp. 1–12, doi: 10.1038/s41467-019-12265-8.
- [33] L. Liu, Q. Ding, Y. Zhong, J. Zou, J. Wu, Y. L. Chiu, J. Li, Z. Zhang, Q. Yu, and Z. Shen, “Dislocation network in additive manufactured steel breaks strength–ductility trade-off,” *Mater. Today*, vol. 21, no. 4, pp. 354–361, 2018, doi: 10.1016/j.mattod.2017.11.004.
- [34] M. Laleh, A. E. Hughes, M. Y. Tan, G. S. Rohrer, S. Primig, and N. Haghdadi, “Grain boundary character distribution in an additively manufactured austenitic stainless steel,” *Scr. Mater.*, vol. 192, pp. 115–119, 2021, doi: 10.1016/j.scriptamat.2020.10.018.
- [35] M. Thomas, G. J. Baxter, and I. Todd, “Normalised model-based processing diagrams for additive layer manufacture of engineering alloys,” *Acta Mater.*, vol. 108, pp. 26–35, 2016, doi: 10.1016/j.actamat.2016.02.025.
- [36] T. DebRoy, H. L. Wei, J. S. Zuback, T. Mukherjee, J. W. Elmer, J. O. Milewski, A. M. Beese, A. Wilson-Heid, A. De, and W. Zhang, “Additive manufacturing of metallic components – Process, structure and properties,” *Prog. Mater. Sci.*, vol. 92, pp. 112–224, 2018, doi: 10.1016/j.pmatsci.2017.10.001.
- [37] K. A. Sofinowski, S. Raman, X. Wang, B. Gaskey, and M. Seita, “Layer-wise engineering of grain orientation (LEGO) in laser powder bed fusion of stainless steel 316L,” *Addit. Manuf.*, vol. 38, p. 101809, 2021, doi: 10.1016/j.addma.2020.101809.
- [38] D. P. M. da Fonseca, A. L. Melo Feitosa, L. G. de Carvalho, R. L. Plaut, and A. F. Padilha, “A short review on ultra-high-strength maraging steels and future

- perspectives,” *Mater. Res.*, vol. 24, no. 1, 2021, doi: 10.1590/1980-5373-MR-2020-0470.
- [39] E. V. Pereloma, A. Shekhter, M. K. Miller, and S. P. Ringer, “Ageing behaviour of an Fe-20Ni-1.8Mn-1.6Ti-0.59Al (wt%) maraging alloy: Clustering, precipitation and hardening,” *Acta Mater.*, vol. 52, no. 19, pp. 5589–5602, 2004, doi: 10.1016/j.actamat.2004.08.018.
- [40] Renishaw plc, “Maraging steel M300 powder for additive manufacturing * H-5800-3429-03-A *,” vol. 2001, no. Iso 97, pp. 8–9, 2001.
- [41] S. Jiang, H. Wang, Y. Wu, X. Liu, H. Chen, M. Yao, B. Gault, D. Ponge, D. Raabe, A. Hirata, M. Chen, Y. Wang, and Z. Lu, “Ultrastrong steel via minimal lattice misfit and high-density nanoprecipitation,” *Nature*, vol. 544, no. 7651, pp. 460–464, 2017, doi: 10.1038/nature22032.
- [42] L. Sun, T. H. Simm, T. L. Martin, S. McAdam, D. R. Galvin, K. M. Perkins, P. A. J. Bagot, M. P. Moody, S. W. Ooi, P. Hill, M. J. Rawson, and H. K. D. H. Bhadeshia, “A novel ultra-high strength maraging steel with balanced ductility and creep resistance achieved by nanoscale β -NiAl and Laves phase precipitates,” *Acta Mater.*, vol. 149, pp. 285–301, 2018, doi: 10.1016/j.actamat.2018.02.044.
- [43] F. F. Conde, J. D. Escobar, J. P. Oliveira, M. Béreš, A. L. Jardini, W. W. Bose, and J. A. Avila, “Effect of thermal cycling and aging stages on the microstructure and bending strength of a selective laser melted 300-grade maraging steel,” *Mater. Sci. Eng. A*, vol. 758, no. September 2018, pp. 192–201, 2019, doi: 10.1016/j.msea.2019.03.129.
- [44] S. A. R. Shamsdini, S. Shakerin, A. Hadadzadeh, B. S. Amirkhiz, and M. Mohammadi, “A trade-off between powder layer thickness and mechanical properties in additively manufactured maraging steels,” *Mater. Sci. Eng. A*, vol. 776, no. February, p. 139041, 2020, doi: 10.1016/j.msea.2020.139041.
- [45] S. A. R. Shamsdini, M. H. Ghoncheh, M. Sanjari, H. Pirgazi, B. S. Amirkhiz, L. Kestens, and M. Mohammadi, “Plastic deformation throughout strain-induced phase transformation in additively manufactured maraging steels,” *Mater. Des.*, vol. 198, p. 109289, 2021, doi: 10.1016/j.matdes.2020.109289.
- [46] B. Mooney, K. I. Kourousis, and R. Raghavendra, “Plastic anisotropy of additively manufactured maraging steel: Influence of the build orientation and heat treatments,” *Addit. Manuf.*, vol. 25, no. September 2018, pp. 19–31, 2019, doi: 10.1016/j.addma.2018.10.032.
- [47] R. Casati, J. Lemke, A. Tuissi, and M. Vedani, “Aging Behaviour and Mechanical Performance of 18-Ni 300 Steel Processed by Selective Laser Melting,” *Metals (Basel)*, vol. 6, no. 9, p. 218, 2016, doi: 10.3390/met6090218.
- [48] K. Kempen, E. Yasa, L. Thijs, J. P. Kruth, and J. Van Humbeeck, “Microstructure and mechanical properties of selective laser melted 18Ni-300 steel,” *Phys. Procedia*, vol. 12, no. PART 1, pp. 255–263, 2011, doi: 10.1016/j.phpro.2011.03.033.
- [49] S. Yin, C. Chen, X. Yan, X. Feng, R. Jenkins, P. O’Reilly, M. Liu, H. Li, and R. Lupoi, “The influence of aging temperature and aging time on the mechanical and tribological properties of selective laser melted maraging 18Ni-300 steel,” *Addit. Manuf.*, vol. 22, no. May, pp. 592–600, 2018, doi: 10.1016/j.addma.2018.06.005.

- [50] F. S. H. B. Freeman, A. Lincoln, J. Sharp, A. Lambourne, and I. Todd, "Exploiting thermal strain to achieve an in-situ magnetically graded material," *Mater. Des.*, vol. 161, no. November, pp. 14–21, 2019, doi: 10.1016/j.matdes.2018.11.011.
- [51] F. S. H. B. Freeman, J. Sharp, J. Xi, and I. Todd, "Influence of solidification cell structure on the martensitic transformation in additively manufactured steels," *Addit. Manuf.*, vol. 30, no. October, p. 100917, 2019, doi: 10.1016/j.addma.2019.100917.
- [52] O. Grässel, L. Krüger, G. Frommeyer, and L. W. Meyer, "High strength Fe-Mn-(Al, Si) TRIP/TWIP steels development - properties - application," *Int. J. Plast.*, vol. 16, no. 10, pp. 1391–1409, 2000, doi: 10.1016/S0749-6419(00)00015-2.
- [53] E. Welsch, D. Ponge, S. M. Hafez Haghghat, S. Sandlöbes, P. Choi, M. Herbig, S. Zaefferer, and D. Raabe, "Strain hardening by dynamic slip band refinement in a high-Mn lightweight steel," *Acta Mater.*, vol. 116, pp. 188–199, 2016, doi: 10.1016/j.actamat.2016.06.037.
- [54] K. M. Rahman, V. A. Vorontsov, and D. Dye, "The effect of grain size on the twin initiation stress in a TWIP steel," *Acta Mater.*, vol. 89, pp. 247–257, 2015, doi: 10.1016/j.actamat.2015.02.008.
- [55] J. Gao, S. Jiang, H. Zhang, Y. Huang, D. Guan, Y. Xu, S. Guan, L. A. Bendersky, A. V. Davydov, Y. Wu, H. Zhu, Y. Wang, Z. Lu, and W. M. Rainforth, "Facile route to bulk ultrafine-grain steels for high strength and ductility," *Nature*, vol. 590, no. 7845, pp. 262–267, 2021, doi: 10.1038/s41586-021-03246-3.
- [56] Q. Xie, Z. Pei, J. Liang, D. Yu, Z. Zhao, P. Yang, R. Li, M. Eisenbach, and K. An, "Transition from the twinning induced plasticity to the γ - ϵ transformation induced plasticity in a high manganese steel," *Acta Mater.*, vol. 161, pp. 273–284, Dec. 2018, doi: 10.1016/J.ACTAMAT.2018.09.020.
- [57] B. C. De Cooman, Y. Estrin, and S. K. Kim, "Twinning-induced plasticity (TWIP) steels," *Acta Mater.*, vol. 142, pp. 283–362, 2018, doi: 10.1016/j.actamat.2017.06.046.
- [58] J. E. Jin and Y. K. Lee, "Effects of Al on microstructure and tensile properties of C-bearing high Mn TWIP steel," *Acta Mater.*, vol. 60, no. 4, pp. 1680–1688, 2012, doi: 10.1016/j.actamat.2011.12.004.
- [59] A. Saeed-Akbari, J. Imlau, U. Prah, and W. Bleck, "Derivation and variation in composition-dependent stacking fault energy maps based on subregular solution model in high-manganese steels," *Metall. Mater. Trans. A Phys. Metall. Mater. Sci.*, vol. 40, no. 13, pp. 3076–3090, 2009, doi: 10.1007/s11661-009-0050-8.
- [60] M. Koyama, E. Akiyama, Y. K. Lee, D. Raabe, and K. Tsuzaki, "Overview of hydrogen embrittlement in high-Mn steels," *Int. J. Hydrogen Energy*, vol. 42, no. 17, pp. 12706–12723, 2017, doi: 10.1016/j.ijhydene.2017.02.214.
- [61] D. K. Han, S. K. Lee, S. J. Noh, S. K. Kim, and D. W. Suh, "Effect of aluminium on hydrogen permeation of high-manganese twinning-induced plasticity steel," *Scr. Mater.*, vol. 99, pp. 45–48, 2015, doi: 10.1016/j.scriptamat.2014.11.023.
- [62] H. Springer and D. Raabe, "Rapid alloy prototyping: Compositional and thermo-mechanical high throughput bulk combinatorial design of structural materials based on the example of 30Mn-1.2C-xAl triplex steels," *Acta Mater.*, vol. 60, no. 12, pp. 4950–4959, 2012, doi: 10.1016/j.actamat.2012.05.017.

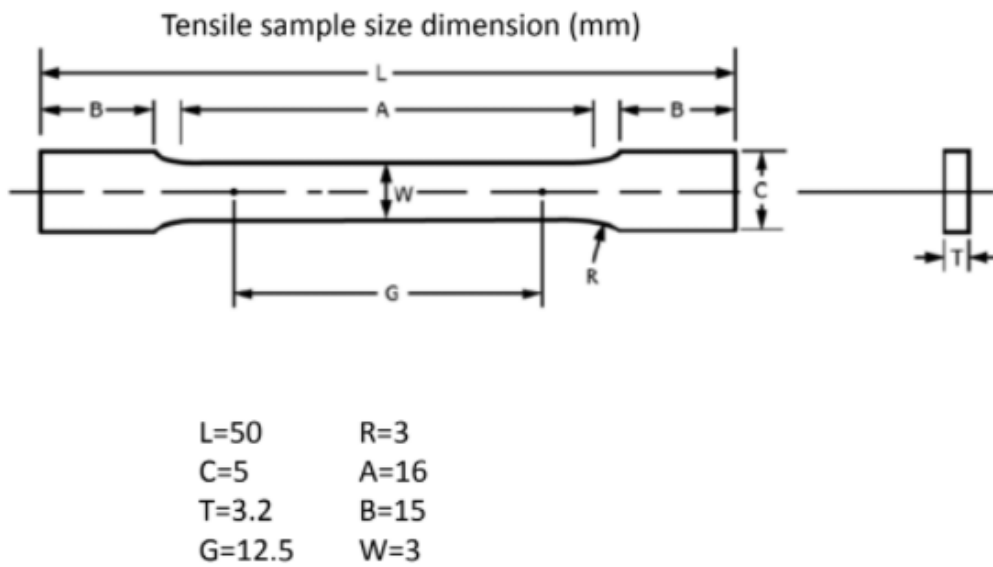
- [63] M. C. Jo, J. H. Choi, H. Lee, A. Zargaran, J. H. Ryu, S. S. Sohn, N. J. Kim, and S. Lee, “Effects of solute segregation on tensile properties and serration behavior in ultra-high-strength high-Mn TRIP steels,” *Mater. Sci. Eng. A*, vol. 740–741, no. October 2018, pp. 16–27, 2019, doi: 10.1016/j.msea.2018.10.065.
- [64] S. Lee, S. J. Lee, and B. C. De Cooman, “Austenite stability of ultrafine-grained transformation-induced plasticity steel with Mn partitioning,” *Scr. Mater.*, vol. 65, no. 3, pp. 225–228, 2011, doi: 10.1016/j.scriptamat.2011.04.010.
- [65] R. Ding, Y. Yao, B. Sun, G. Liu, J. He, T. Li, X. Wan, Z. Dai, D. Ponge, D. Raabe, C. Zhang, A. Godfrey, G. Miyamoto, T. Furuhashi, Z. Yang, S. Van Der Zwaag, and H. Chen, “Chemical boundary engineering : A new route toward lean , ultrastrong yet ductile steels,” pp. 1–9, 2020.
- [66] S. W. Ooi, J. E. Garnham, and T. I. Ramjaun, “Review: Low transformation temperature weld filler for tensile residual stress reduction,” *Mater. Des.*, vol. 56, pp. 773–781, 2014, doi: 10.1016/j.matdes.2013.11.050.
- [67] A. Ohta, N. Suzuki, Y. Maeda, K. Hiraoka, and T. Nakamura, “Superior fatigue crack growth properties in newly developed weld metal,” *Int. J. Fatigue*, vol. 21, pp. 113–118, 1999, doi: 10.1016/S0142-1123(99)00062-6.
- [68] A. Ohta, K. Matsuoka, N. T. Nguyen, Y. Maeda, and N. Suzuki, “Fatigue strength improvement of lap joints of thin steel plate using low-transformation-temperature welding wire,” *Weld. J. (Miami, Fla)*, vol. 82, no. 4, 2003.
- [69] J. J. Yan, D. L. Zheng, H. X. Li, X. Jia, J. F. Sun, Y. L. Li, M. Qian, and M. Yan, “Selective laser melting of H13: microstructure and residual stress,” *J. Mater. Sci.*, vol. 52, no. 20, pp. 12476–12485, 2017, doi: 10.1007/s10853-017-1380-3.
- [70] M. Król, P. Snopiński, and A. Czech, “The phase transitions in selective laser-melted 18-NI (300-grade) maraging steel,” *J. Therm. Anal. Calorim.*, vol. 142, no. 2, pp. 1011–1018, 2020, doi: 10.1007/s10973-020-09316-4.
- [71] F. Freeman, “Structuring Difference: The Additive Manufacture of Spatially & Functionally Differentiated Microstructures,” no. October, 2018, [Online]. Available: <http://etheses.whiterose.ac.uk/22742/>
- [72] T. W. Eagar and N. S. Tsai, “Temperature fields produced by traveling distributed heat sources,” *Weld. J.*, vol. 62, no. 12, pp. 346–355, 1983.
- [73] M. Arjomandi, H. Khorsand, S. H. Sadati, and H. Abdoos, “Prediction of martensite formation start temperature in steels using artificial neural networks,” *Defect Diffus. Forum*, vol. 273–276, no. April, pp. 329–334, 2008, doi: 10.4028/www.scientific.net/ddf.273-276.329.
- [74] Z. Li, K. G. Pradeep, Y. Deng, D. Raabe, and C. C. Tasan, “Metastable high-entropy dual-phase alloys overcome the strength–ductility trade-off,” *Nature*, pp. 4–11, 2016, doi: 10.1038/nature17981.
- [75] E. I. Galindo-Nava and P. E. J. Rivera-Díaz-del-Castillo, “Understanding martensite and twin formation in austenitic steels: A model describing TRIP and TWIP effects,” *Acta Mater.*, vol. 128, pp. 120–134, Apr. 2017, doi: 10.1016/J.ACTAMAT.2017.02.004.
- [76] F. Kies, P. Köhnen, M. B. Wilms, F. Brasche, K. G. Pradeep, A. Schwedt, S. Richter,

- A. Weisheit, J. H. Schleifenbaum, and C. Haase, "Design of high-manganese steels for additive manufacturing applications with energy-absorption functionality," *Mater. Des.*, vol. 160, pp. 1250–1264, 2018, doi: 10.1016/j.matdes.2018.10.051.
- [77] P. Köhnen, C. Haase, J. Bültmann, S. Ziegler, J. H. Schleifenbaum, and W. Bleck, "Mechanical properties and deformation behavior of additively manufactured lattice structures of stainless steel," *Mater. Des.*, vol. 145, pp. 205–217, 2018, doi: 10.1016/j.matdes.2018.02.062.
- [78] D. Pérez Escobar, S. Silva Ferreira De Dafé, and D. Brandão Santos, "Martensite reversion and texture formation in 17Mn-0.06C TRIP/TWIP steel after hot cold rolling and annealing," *J. Mater. Res. Technol.*, vol. 4, no. 2, pp. 162–170, 2015, doi: 10.1016/j.jmrt.2014.10.004.
- [79] L. Mujica, S. Weber, H. Pinto, C. Thomy, and F. Vollertsen, "Microstructure and mechanical properties of laser-welded joints of TWIP and TRIP steels," *Mater. Sci. Eng. A*, vol. 527, no. 7–8, pp. 2071–2078, 2010, doi: 10.1016/j.msea.2009.11.050.
- [80] J. Hunt, F. Derguti, and I. Todd, "Selection of steels suitable for additive layer manufacturing," *Ironmak. Steelmak.*, vol. 41, no. 4, pp. 254–256, 2014, doi: 10.1179/0301923314Z.000000000269.
- [81] P. Köhnen, S. Ewald, J. H. Schleifenbaum, A. Belyakov, and C. Haase, "Controlling microstructure and mechanical properties of additively manufactured high-strength steels by tailored solidification," *Addit. Manuf.*, vol. 35, no. May, p. 101389, 2020, doi: 10.1016/j.addma.2020.101389.
- [82] S. Takaki, K. Fukunaga, J. Syarif, and T. Tsuchiyama, "Effect of grain refinement on thermal stability of metastable austenitic steel," *Mater. Trans.*, vol. 45, no. 7, pp. 2245–2251, 2004, doi: 10.2320/matertrans.45.2245.
- [83] L. Facchini, N. Vicente, I. Lonardelli, E. Magalini, P. Robotti, and M. Alberto, "Metastable austenite in 17-4 precipitation-hardening stainless steel produced by selective laser melting," *Adv. Eng. Mater.*, vol. 12, no. 3, pp. 184–188, 2010, doi: 10.1002/adem.200900259.
- [84] A. D. Kudzal, B. A. McWilliams, J. Taggart-Scarff, and M. Knezevic, "Fabrication of a low alloy ultra-high strength (>1500 MPa yield) steel using powder bed fusion additive manufacturing," *Mater. Sci. Eng. A*, vol. 770, no. June 2019, p. 138512, 2019, doi: 10.1016/j.msea.2019.138512.
- [85] B. B. He, B. Hu, H. W. Yen, G. J. Cheng, Z. K. Wang, H. W. Luo, and M. X. Huang, "High dislocation density-induced large ductility in deformed and partitioned steels," *Science (80-.)*, vol. 357, no. 6355, pp. 1029–1032, 2017, doi: 10.1126/science.aan0177.
- [86] F. F. Conde, J. D. Escobar, J. P. Oliveira, A. L. Jardini, W. W. Bose Filho, and J. A. Avila, "Austenite reversion kinetics and stability during tempering of an additively manufactured maraging 300 steel," *Addit. Manuf.*, vol. 29, no. July, p. 100804, 2019, doi: 10.1016/j.addma.2019.100804.
- [87] F. S. H. B. Freeman, J. Sharp, J. Xi, and I. Todd, "Influence of solidification cell structure on the martensitic transformation in additively manufactured steels," *Addit. Manuf.*, vol. 30, no. July, p. 100917, 2019, doi: 10.1016/j.addma.2019.100917.

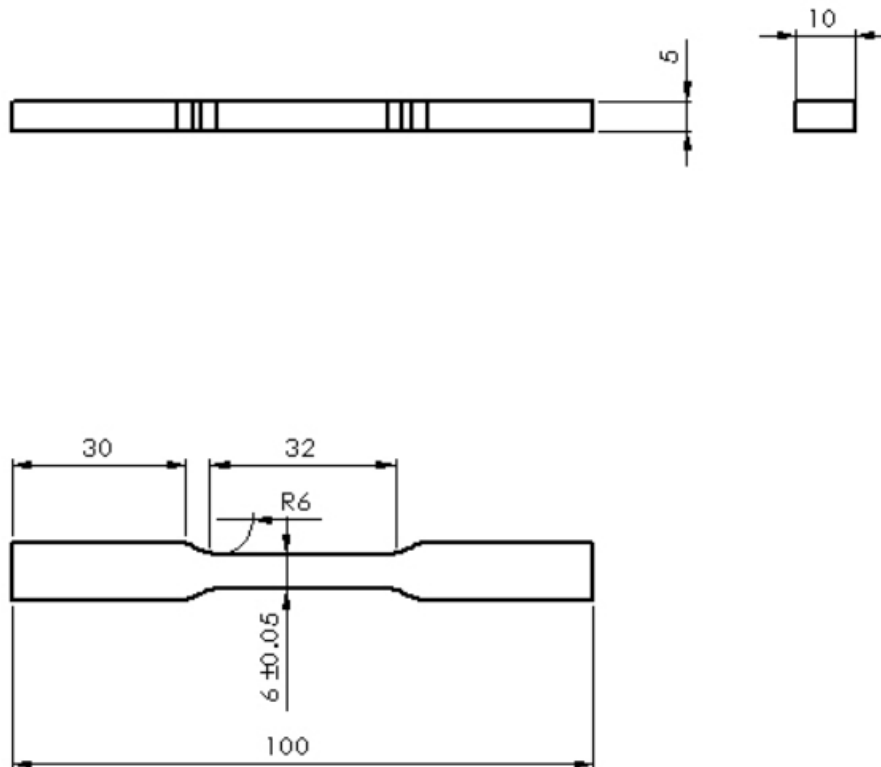
- [88] T. Allam, K. G. Pradeep, P. Köhnen, A. Marshal, J. H. Schleifenbaum, and C. Haase, “Tailoring the nanostructure of laser powder bed fusion additively manufactured maraging steel,” *Addit. Manuf.*, vol. 36, no. June, 2020, doi: 10.1016/j.addma.2020.101561.
- [89] R. Kapoor, L. Kumar, and I. S. Batra, “A dilatometric study of the continuous heating transformations in 18wt.% Ni maraging steel of grade 350,” *Mater. Sci. Eng. A*, vol. 352, no. 1–2, pp. 318–324, 2003, doi: 10.1016/S0921-5093(02)00934-6.
- [90] E. A. Jäggle, Z. Sheng, P. Kürnsteiner, S. Ocylok, A. Weisheit, and D. Raabe, “Comparison of maraging steel micro- and nanostructure produced conventionally and by laser additive manufacturing,” *Materials (Basel)*, vol. 10, no. 1, 2017, doi: 10.3390/ma10010008.
- [91] M. Carrard, M. Gremaud, M. Zimmermann, and W. Kurz, “About the banded structure in rapidly solidified dendritic and eutectic alloys,” *Acta Metall. Mater.*, vol. 40, no. 5, pp. 983–996, 1992, doi: 10.1016/0956-7151(92)90076-Q.
- [92] T. T. Roehling, S. S. Q. Wu, S. A. Khairallah, J. D. Roehling, S. S. Soezeri, M. F. Crumb, and M. J. Matthews, “Modulating laser intensity profile ellipticity for microstructural control during metal additive manufacturing,” *Acta Mater.*, vol. 128, pp. 197–206, 2017, doi: 10.1016/j.actamat.2017.02.025.
- [93] I. Zarudi and L. C. Zhang, “Modelling the structure changes in quenchable steel subjected to grinding,” *J. Mater. Sci.*, vol. 37, no. 20, pp. 4333–4341, 2002, doi: 10.1023/A:1020652519141.
- [94] K. S. Raghavan, G. Thomas, J. Arnold, A. Gill, and T. Gnaupel-Herold, “A comparison of different measurement methods to evaluate strain-induced martensite formation in a metastable austenitic stainless steel,” *Mater. Sci. Technol. Conf. Exhib. 2014, MS T 2014*, vol. 1, no. August 2018, pp. 187–199, 2014.
- [95] S. S. Ansari, J. Mukhopadhyay, and S. V. S. N. Murty, “Analysis of Stress-Strain Curves to Predict Dynamic Recrystallization During Hot Deformation of M300 Grade Maraging Steel,” *J. Mater. Eng. Perform.*, vol. 30, no. 8, pp. 5557–5567, 2021, doi: 10.1007/s11665-021-05780-7.
- [96] T. Mukherjee, J. S. Zuback, A. De, and T. DebRoy, “Printability of alloys for additive manufacturing,” *Sci. Rep.*, vol. 6, pp. 1–8, 2016, doi: 10.1038/srep19717.
- [97] C. Li, J. F. Liu, X. Y. Fang, and Y. B. Guo, “Efficient predictive model of part distortion and residual stress in selective laser melting,” vol. 17, pp. 157–168, 2017, doi: 10.1016/j.addma.2017.08.014.
- [98] D. P. Field, R. C. Eames, and T. M. Lillo, “The role of shear stress in the formation of annealing twin boundaries in copper,” *Scr. Mater.*, vol. 54, no. 6, pp. 983–986, 2006, doi: 10.1016/j.scriptamat.2005.11.037.
- [99] H. Lee, M. C. Jo, S. S. Sohn, A. Zargaran, J. H. Ryu, N. J. Kim, and S. Lee, “Novel medium-Mn (austenite + martensite) duplex hot-rolled steel achieving 1.6 GPa strength with 20 % ductility by Mn-segregation-induced TRIP mechanism,” *Acta Mater.*, vol. 147, pp. 247–260, Apr. 2018, doi: 10.1016/J.ACTAMAT.2018.01.033.
- [100] W. Chen, L. Xu, Y. Han, L. Zhao, and H. Jing, “Control of residual stress in metal additive manufacturing by low-temperature solid-state phase transformation: An

- experimental and numerical study,” *Addit. Manuf.*, vol. 42, no. February, 2021, doi: 10.1016/j.addma.2021.102016.
- [101] J. Haan, M. Asseln, M. Zivcec, J. Eschweiler, R. Radermacher, and C. Broeckmann, “Effect of subsequent Hot Isostatic Pressing on mechanical properties of ASTM F75 alloy produced by Selective Laser Melting,” *Powder Metall.*, vol. 58, no. 3, pp. 161–165, 2015, doi: 10.1179/0032589915Z.000000000236.
- [102] S. Hocine, H. Van Swygenhoven, S. Van Petegem, C. S. T. Chang, T. Maimaitiyili, G. Tinti, D. Ferreira Sanchez, D. Grolimund, and N. Casati, “Operando X-ray diffraction during laser 3D printing,” *Mater. Today*, vol. 34, no. April, pp. 30–40, 2020, doi: 10.1016/j.mattod.2019.10.001.

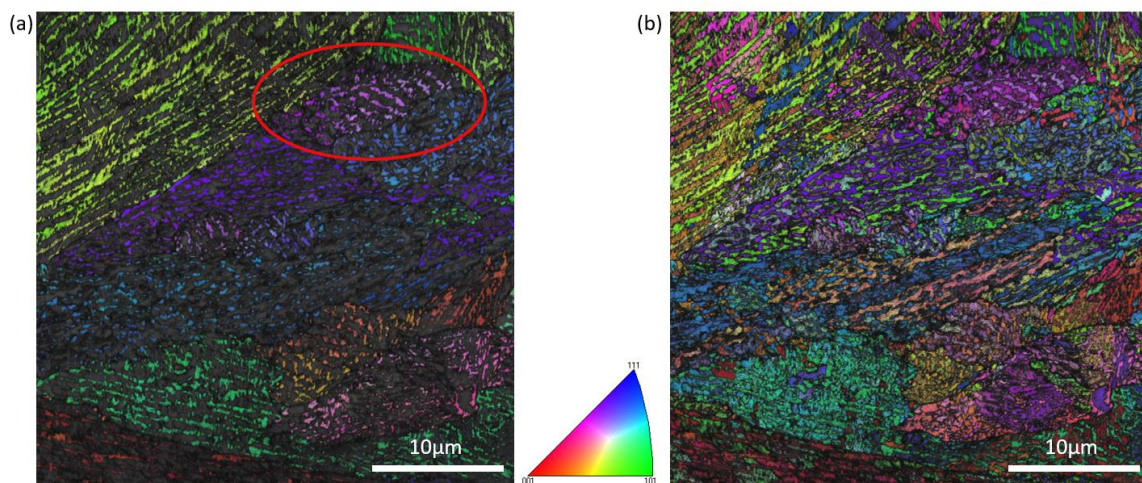
Appendix



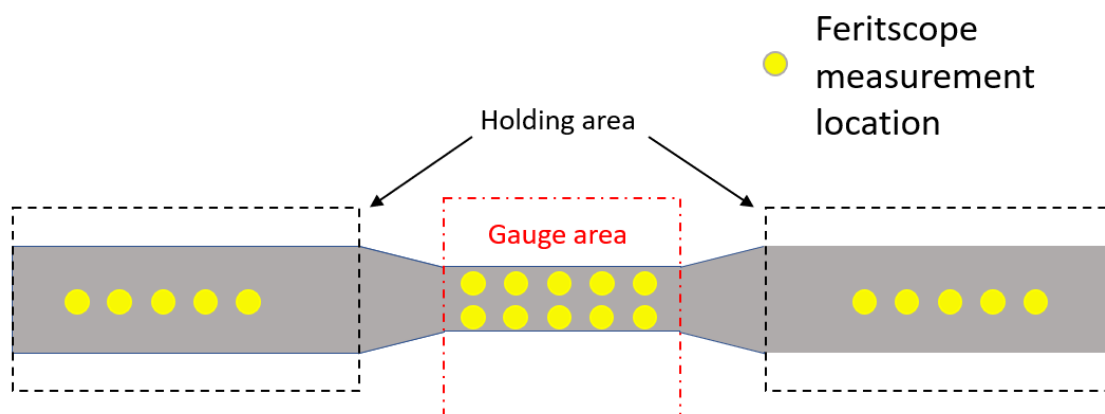
Appendix Figure 1: Drawing of the smaller tensile bar used in Chapter 4 and 5.



Appendix Figure 2: Dimensions of the larger tensile bar tested in Chapter 4 and 5.



Appendix Figure 3: IPF of (a) austenite and (b) combined phases in aged M300 sample. Area circled in red shows near-single variant transformation.



Appendix Figure 4: Schematics of the Feritscope testing procedure of M300 tensile specimen.



AMG Superalloys UK Limited

Fullerton Road, Rotherham, South Yorkshire S60 1DL, England
Telephone: UK 01709 828500 - International: +44 (01709) 828500
Fax: UK 01709 830391 - International: +44 (01709) 830391

FAX TRANSMISSION

Company: The University of Sheffield
Attention: Jiawei Xi
From: D Mason
Page 1 of 1
Comments:

Fax No. 0114 2225943
Date: 13/11/2018
Customer Order No. YK0/4500965710
Lab. Request No. 3806555
Email: jx2@sheffield.ac.uk

TEST REPORT TO FOLLOW WITH FULL ANALYSES DETAILS
Where UKAS Accreditation applies, this will be confirmed on the full analysis certificate

URGENT - TOP PRIORITY

Fe-Mn-Si-Al-C STEEL

3821317

Mn	16.60 %
C	0.32 %

Analysis on 'As Received' Basis

All analysis carried out to our terms and conditions

REGARDS

Fax Check Signature

In the event of an incomplete transmission please contact laboratory administration on Extension 763

Appendix Figure 5: Chemical test certificate of the manganese content in conventionally processed tensile specimen.



AMG Superalloys UK Limited
Fullerton Road, Rotherham, South Yorkshire S60 1DL, England

ANALYTICAL SERVICES

Tel. 01709-833763
Fax. 01709-830391



CERTIFICATE OF ANALYSIS

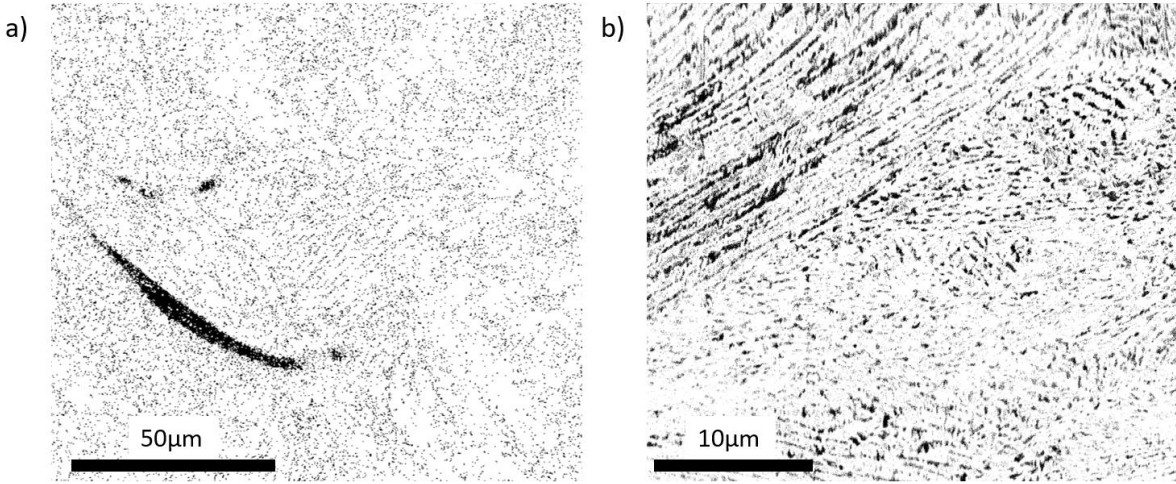
Page No. 1 of 1

Material analysed has been supplied to AMG Analytical Services for 3rd party analysis
Results only relate to items tested

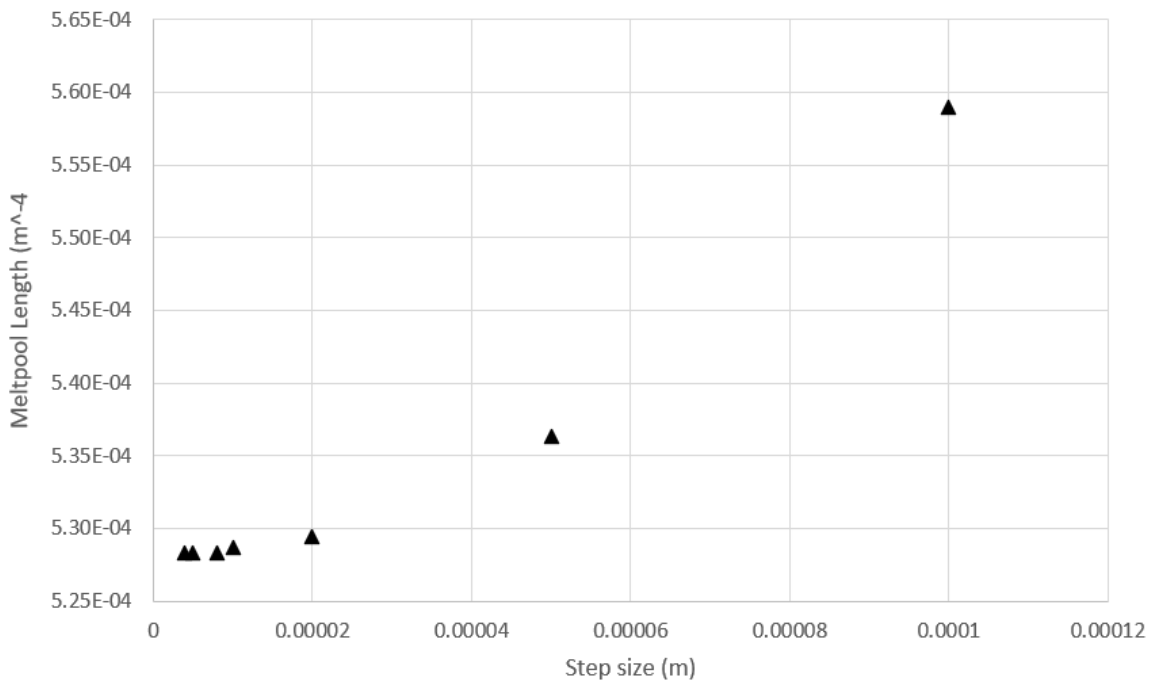
ID The University of Sheffield Dept of Engineering Materials Sir Robert Hadfield Building Portobello Street Sheffield S1 3JD	Certificate Date	12/02/2020	Certificate No.	Lab Request No.
	Date of Receipt	27/01/2020	4000749	4000551
	Analysis Start Date	12/02/2020	Your Ref. / Order No.	
	Analysis End Date	12/02/2020	YK0/4501068481	
Sample Details No. of Samples Submitted : 2				
FAO Jiawei Xi				
Analysis Results				
4001965 FEMN ALLOY POWDER		4001966 FEMN ALLOY SOLID		
C	0.34 %	C	0.33 %	
Al	2.10 %	Al	2.09 %	
Si	0.52 %	Si	0.52 %	
Ti	<0.05 %	Ti	<0.05 %	
V	<0.05 %	V	<0.05 %	
Cr	<0.05 %	Cr	<0.05 %	
Mn	18.44 %	Mn	17.09 %	
Fe	78.43 %	Fe	79.83 %	
Co	<0.05 %	Co	<0.05 %	
Ni	<0.05 %	Ni	<0.05 %	
Cu	<0.05 %	Cu	<0.05 %	
Zr	<0.05 %	Zr	<0.05 %	
Mo	<0.05 %	Mo	<0.05 %	
Sn	<0.05 %	Sn	<0.05 %	
W	<0.05 %	W	<0.05 %	
END OF REPORT				
Analysis on 'As Received' Basis Material: Metallic		Analysis on 'As Received' Basis Material: Metallic		
Comments / Remarks Analysed using in - house documented procedures for technique(s) : Leco XRF Leco Nitrogen - Thermal Conductivity Leco Carbon, Sulphur, Oxygen, Hydrogen - Infra-Red		Certificate Signed by <input checked="" type="checkbox"/> P. W. Hurditch Chief Chemist <input type="checkbox"/> S. L. Temple Office Manager <input type="checkbox"/> I. Hyde Assistant Chief Chemist		
Signed 				

The report shall not be reproduced except in full without approval of the laboratory
Please refer to <http://www.amg-s.com> for our Conditions of Assay
Registered Office as above. Registered in England No. 345279 V.A.T. No. GB 789 6326 65.

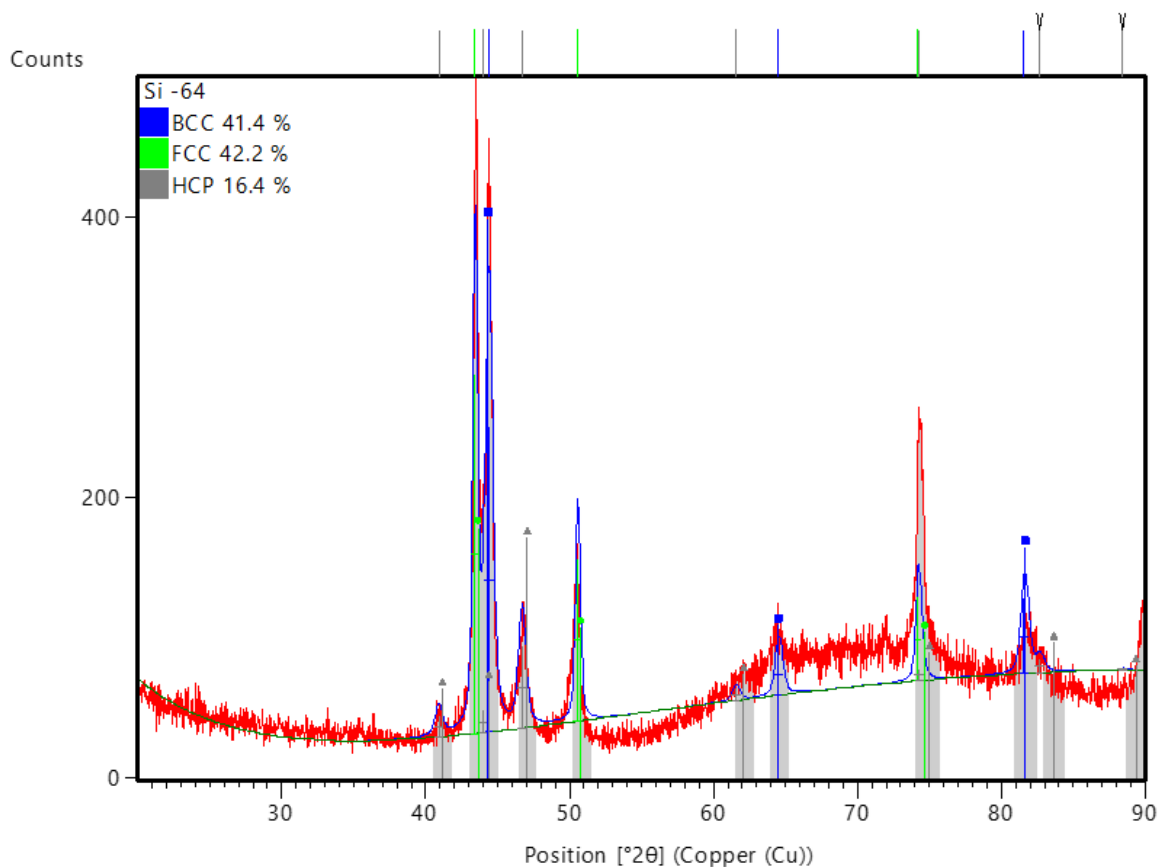
Appendix Figure 6: Chemical test certificate of the full chemical composition of new and unused powder and AM built part.



Appendix Figure 7: 8-bit processed EBSD phase maps of a) as-built and b) 24hrs aged M300 maraging steel for ImageJ area fraction analysis.

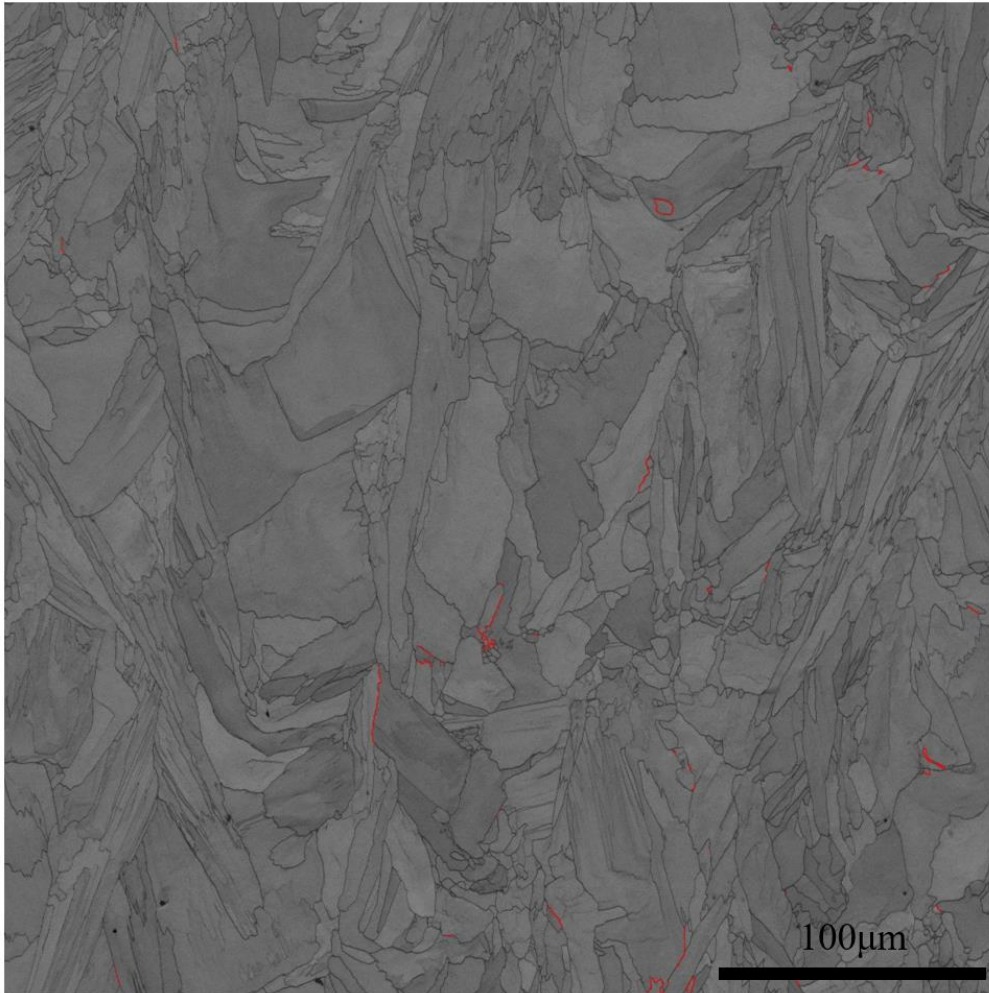


Appendix Figure 8: Sensitivity test of the MATLAB script utilised in this study. A step size of 0.000005 is chosen.



Pos. [°2θ]	Height [cts]	FWHM Left [°2θ]	d-spacing [Å]	Rel. Int. [%]
40.8886	14.74	0.6059	2.20528	5.78
43.4083	255.18	0.3759	2.08293	100.00
43.9588	15.75	0.6059	2.05812	6.17
44.3794	217.17	0.5927	2.03959	85.11
46.6734	58.71	0.6059	1.94454	23.01
50.5350	115.83	0.3759	1.80464	45.39
61.5215	7.85	0.6059	1.50610	3.08
64.4996	29.83	0.5927	1.44356	11.69
74.1882	59.69	0.3759	1.27718	23.39
74.3295	8.39	0.6059	1.27510	3.29
81.5717	53.30	0.5927	1.17921	20.89
82.6306	9.20	0.6059	1.16676	3.61
88.4286	1.29	0.6059	1.10462	0.51

Appendix Figure 9: Rietveld refinement calculation results and the peaks used in the calculation.



Appendix Figure 10: EBSD boundary characteristic map of additively manufactured 316L SS. Σ 3 boundaries are coloured in red.